NORTHWESTERN UNIVERSITY

The Ionic Environment and Solution Interactions of Protein Spherical Nucleic Acids Probed by In-situ X-ray Scattering

A DISSERTATION

SUBMITTED TO THE GRADUATE SCHOOL
IN PARTIAL FULFILLMENT OF THE REQUIREMENTS

for the degree

DOCTOR OF PHILOSOPHY

Field of Applied Physics

By

Kurinji Krishnamoorthy

EVANSTON, ILLINOIS

March 2019

ABSTRACT

The Ionic Environment and Solution Interactions of Protein Spherical Nucleic Acids Probed by In-situ X-ray Scattering

Kurinji Krishnamoorthy

Electrostatic interactions mediated by ionic environments play a central role in physical processes across materials science, chemistry and biology. Key biological phenomena, such as the condensation and packaging of DNA, ion transport across cellular membranes and the enzymatic action of proteins, rely on the complex interplay between nanoscale electrostatic, osmotic and entropic forces. A consideration of such interactions is especially relevant to synthetic bioconjugates, which harness the powerful properties of molecules, such as proteins and nucleic acids to realize applications in materials assembly and therapeutic medicine. Spherical nucleic acids (SNAs) defined as a dense three-dimensional arrangement of oligonucleotides on the surface of a particle core are one such striking example of a bioconjugate whose collective properties are distinct from those of its nucleic acid components. For instance, the DNA shell and associated counterionic cloud on an Au nanoparticle SNA results in highly programmable assembly behavior, cooperative hybridization thermodynamics, efficient internalization across more than 200 different cell types and an enhanced resistance to enzymatic degradation in comparison to linear DNA. While the properties and assembly behavior of spherical nucleic acids are well characterized, the nanoscale structure and role of the counterionic cloud surrounding such constructs is poorly understood. Here, we address this challenge in the context of a spherical nucleic acid composed of

a functional protein core using in-situ solution x-ray scattering techniques. Our approach provides fundamental insights into the ionic environment around a protein spherical nucleic acid (Pro-SNA) and its influence on the resistance of Pro-SNAs to enzymatic degradation.

ACKNOWLEDGEMENTS

I would first like to thank my advisors, Professor Michael Bedzyk and Professor Chad Mirkin for the incredible opportunity to work with two uniquely diverse research groups on some truly interdisciplinary projects spanning materials science, chemistry and x-ray physics. They have always been extremely supportive and have taught me how to be a better scientist and communicator. I am grateful for their unwavering support and find myself incredibly fortunate to have had the opportunity to work with two pioneers in their respective fields.

Secondly, I would like to thank the other members of my committee, Professor Olvera de la Cruz and Professor Pulak Dutta for their invaluable advice, collaboration and helpful discussions. Collaborating with Professor Olvera de la Cruz and members of her group has been an amazing learning experience and has allowed me to gain insight into the theoretical considerations underlying our research. I would also like to thank Dr. Sumit Kewalramani for his mentorship and guidance. He has always been extremely helpful and knowledgeable about x-ray theory, techniques and modelling and is always willing to help in problem-solving and brainstorming new approaches.

I would also like to acknowledge my funding sources the U.S. Department of Energy, Office of Science, Office of Basic Energy Sciences, DOE-BES, under award number DE-SC0018093, MURI: BioProgrammable One-, Two-, and Three-Dimensional Materials under Grant Number: FA9550-11-1-0275 and a fellowship from the Center of Computation and Theory of Soft Materials at Northwestern University. Without this financial support, my graduate research work would not have been possible. I also thank the beamline scientists at the Advanced Photon Source, for their help in acquiring X-ray data, including Dr. Steven Weigand, and Dr. Soenke Seifert.

I would like to thank my collaborators in the Mirkin and Olvera de la Cruz groups – Dr. Jeffrey Brodin for teaching me how to synthesize and characterize protein spherical nucleic acids, Dr. Kyle Hoffmann and Annaliese Ehlen for their useful discussions regarding DFT and MD simulations. I would also like to thank my mentor Dr. Liane Moreau who was always incredibly supportive and taught me how to design and execute a good experiment. I'm grateful for the opportunity to have met, talked to and worked with so many intelligent and talented researchers across the Materials Science, Chemistry and Physics departments and truly cherish my time immersed in the interdisciplinary research environment at Northwestern. I thank all the members of the Mirkin and Bedzyk group for their support and friendship – Stephanie Moffitt, Bor-Rong Chen, Gavin Campbell, Changrui Gao, Katherine Harmon, Elise Goldfine, Anusheela Das, KVLV Narayanachari, Li Zeng, Xiao Chen and Guennadi Evmenenko.

I would also like to thank my friends and family for their steadfast support and companionship. I'd like to thank my parents who have always supported everything I have wanted to do and have been a constant source of encouragement and inspiration. I would like to thank my friends Anjali, Kaushik, Madhu, Riju and Sonali and my boyfriend Nikhil for being my support system and in many ways my family away from home. I would also like to thank the members of the Evanston Animal Shelter for giving me the opportunity work with some amazing people and animals and meet my cat, Mia who has been a loyal companion throughout my graduate career.

Table of Contents

List of Figures

List of Tables

Chapter 1: Introduction

Electrostatic interactions strongly mediate processes and phenomena across all realms of the physical sciences. This is profoundly manifest in biological systems wherein a delicate balance between electrostatic, osmotic and entropic forces enables processes central to the existence of life. For instance, multivalent cations induce the condensation and packaging of genomic DNA into viral capsids more than 500 times smaller than their average length.[1-2] The ability of proteins to stabilize their native structure and efficiently catalyze reactions on the nanoscale relies on the presence of biologically relevant mono and divalent salt ions, such as Na^+, K^+ and Mg^{2+}.[3-4] The powerful properties of such biomacromolecules are increasingly being leveraged to create synthetic structures with applications in materials assembly and therapeutic medicine. Colloidal nanoparticle-based formulations, in particular, have garnered significant interest due to the wealth of chemistry that may be used to tune their surface properties and compatibility with biomolecules. An outstanding example in this class of novel materials are nanoparticles with a covalently bound shell of nucleic acids. These bioconjugates, termed Spherical Nucleic Acids[5] (SNA) have unique properties dictated by both their nanoparticle core and oligonucleotide shell. For instance, Watson-Crick hybridization between complementary DNA on neighboring nanoparticle cores can be used to controllably program their assembly into well-defined crystalline lattices.[6-8] Rational design of the DNA base sequence, length and the identity of the particle core has enabled the realization of diverse lattice types including BCC, FCC and AlB_2 to name a few.[6] The identity of the nucleic acid ligand on the nanoparticle surface may be judiciously chosen to realize applications in detection[9], bio diagnostics[10], gene regulation[11] and immunomodulation.[12] The density and orientation of the nucleic acid shell characteristic to SNA architecture results in sharp and highly cooperative DNA melting transitions,[13] enhanced cellular uptake[14-15] and an increased stability against enzymatic degradation.[16-17] Further, the extensive library of possible core choices including Au,[5] Ag,[18] Fe_3O_4,[19] liposomes[20] and proteins[21] can be used to confer additional plasmonic, catalytic and magnetic to an SNA.

As is the case with most materials systems, the functional properties of spherical nucleic acid conjugates are dictated by their nanoscale structure. A thorough elucidation of their structure should allow us to develop a comprehensive understanding of the origin of their remarkable properties. The small size and lack of structural order inherent to aqueous dispersions of isolated DNA-nanoparticle conjugates makes them ill-suited to traditional atomic scale characterization techniques including x-ray diffraction, crystallography or ligand-binding chemistry. Spectroscopic tools (such as UV-Vis and circular dichroism) and dynamic light scattering (DLS) can provide information on the macroscopic physical and chemical attributes of the constructs but they lack the nanometer scale resolution and element specificity required to develop a full description of SNA structure and properties. Electron microscopy is a powerful local probe of nanoparticle shape and morphology, but is typically insensitive to the relatively low-contrast biomolecular corona functionalized onto the nanoparticle cores. In addition, it requires the conjugates to be dried out, frozen or embedded in silica which may disrupt their native solution structure. An ideal characterization approach for such materials should non-destructively probe their solution structure in-situ to yield nanometer-scale information. Small Angle X-ray Scattering meets these requirements because of its ability to globally probe the solution structure of both nanomaterials and biomolecules with dimensions ranging from 1-100 nm in-situ.[22-23] SAXS has been extensively used to elucidate and identify crystalline arrangements of self-assembled materials[24] including those of spherical nucleic acids[6] as well as the solution structure of isolated nanoparticles,[25-26] proteins[27-28] and nucleic acids.[29-30] In addition to being a sensitive measure of nanoparticle core size and shape, contrast variation SAXS techniques, such as anomalous small angle x-ray scattering (ASAXS) can be used to discern the local concentration and ion density distribution profiles surrounding nanoparticle conjugates[31-32] making it particularly well suited for the investigation of the counterionic cloud surrounding spherical nucleic acid conjugates. With a pragmatic selection of particle core, SAXS may also be used to directly probe the structural attributes of the oligonucleotide shell component of a spherical nucleic acid conjugate.

One of the most promising choices of particle core is a protein – nature's functional nanoparticle. The library of known proteins encompasses a structurally and functionally rich parameter space, which could be explored to realize potential transfection, catalytic and signaling applications.[33-35] Previous work has demonstrated the facile synthesis, assembly and cellular transfection properties of Protein Spherical Nucleic Acid (Pro-SNA) nanostructures with Catalase and β- Galactosidase enzyme cores.[21, 36-37] In spite of relatively high DNA loading densities varying between 25-50 strands per particle, the proteins were demonstrated to retain their native structure and catalytic functionality. In addition, they were successfully co-assembled with both protein and Au nanoparticles bearing complementary DNA sequences resulting in the formation of BCC and CsCl type superlattices. Protein Spherical Nucleic Acids also have immense potential in intracellular protein transfection applications, which are typically hindered by the instability, large size and surface charge inherent to most proteins of interest.[38] For the case of β- Galactosidase, surface modification with a dense shell of oligonucleotides has shown to enhance its cellular uptake across multiple different cell lines by upto 280-fold relative to the native enzyme in spite of working concentrations as low as 100 pM. Once endocytosed, β- Galactosidase retains its ability to catalyze the hydrolysis of β- glycosidic linkages highlighting the remarkable ability of Pro-SNAs to engineer cellular functions. Thus, the dense three-dimensional architecture of DNA on the surface of the protein confers to it the distinctive properties of a Spherical Nucleic Acid. Apart from the breadth and efficiency of their catalytic ability, proteins possess an unparalleled degree of structural and compositional homogeneity. This bestows Protein Spherical Nucleic Acids with a high degree of shape and size monodispersity, which when coupled with their relatively low electron density make them an ideal candidate for SAXS. This work demonstrates the use of in-situ SAXS techniques to measure the solution structure and interactions of these conjugates.

In addition to its modular core and shell components, a crucial and often overlooked feature of an SNA is the dense shell of charge compensating counterions bound to the DNA shell. Several key SNA properties derive from the enhanced concentrations of counterions presented at its surface. For instance, the enhanced resistance of an SNA to enzymatic degradation by nucleases is hypothesized to result from the elevated local concentration of Na^+ counterions in the vicinity of the DNA shell.[16] This Na^+ counterionic cloud is believed to inhibit the activity of nucleases, such as DNase I thus promoting the stability of SNAs in intracellular environments. The highly cooperative hybridization behavior and sharp melting temperature of assembled SNAs are also facilitated by the presence of a dense counterionic environment.[13] Thus, a systematic investigation of the structure of this counterionic cloud and its effects on the interactions of an SNA with the solution interface is vital to developing a complete understanding of SNA function. Developing a complete picture of the structure and solution interactions of SNAs should enable a deeper understanding of their properties and will pave the path towards optimizing their performance.

Herein, we address this objective in the context of Protein Spherical Nucleic Acids with a goal to establish generalizable key insights into the structure-function relationships of Spherical Nucleic Acids and other complex biomolecular conjugates.

This thesis starts by introducing the experimental methods employed (Chapter 2). The basic physical principles underlying the techniques and a brief guide to a qualitative and quantitative interpretation of the data are provided. We then apply these techniques to develop a thorough nanoscale description of the structure of a Pro-SNA and its counterionic cloud (Chapter 3) and the effect of solution conditions on the same. We then explore the effect of Pro-SNA structure on an important solution interaction – that with the intracellular nuclease, DNase I. Through the use of an in-situ X-ray Scattering approach the mechanistic pathway governing the interaction of DNase I with a Pro-SNA is illuminated (Chapter 4). Finally, the influence of ion valency on the composition of the counterionic cloud surrounding a Pro-SNA is explored in Chapter 5. These three studies allow us to illuminate the nuances of a critical SNA structure-property relationship – that between its dense ionic environment and its observed resistance to enzymatic degradation. The key results achieved through the use our X-ray scattering approach are further complemented with insights obtained through Density Functional Theory and methods in analytical chemistry such as Gel Electrophoresis and Fluorescence spectroscopy. We then conclude with a discussion highlighting the impact and future directions made possible through our work (Chapter 6).

Chapter 2: Methods

2.1. Synthesis of Protein Spherical Nucleic Acids

Synthesis strategies for Spherical Nucleic Acid constructs typically rely on chemistries suited for the chosen core material. For instance, Au nanoparticle SNAs are synthesized by utilizing a Au-SH covalent bond between the Au nanoparticle surface and a SH (Thiol) group on either the 5' or 3' terminus of a synthetic oligonucleotide.[39] The loading of such DNA or RNA onto Au nanoparticle cores ranging in diameter from 5-200 nm are then optimized using well-established salt-aging protocols. Similar specialized strategies have been designed for a range of core materials including Ag,[18] Fe_3O_4,[19] CdSe/ZnS[40] quantum dots and liposomes.[20]

Proteins distinguish themselves from traditional inorganic core materials due to the distinct pattern of functional residues on their surface. Therefore, the DNA functionalization strategy for proteins relies on chemical modification to selected solvent accessible functional groups on the protein with synthetic DNA terminated with specialty phosphoramidites. For the case of the Corynebacterium Glutamicum (*Cg*) Catalase Pro-SNA studied in this work, the solvent accessible lysine residues on the protein are modified with DNA using the following two-step protocol:

The proteins are reacted with a 3000-fold excess of tetraethylene glycol linkers containing an azide moiety and an N-hydroxy-succinimide (NHS) ester on opposing termini. Each reaction contains 50 µM protein dispersed in a Sodium Bicarbonate buffer (100 mM $NaHCO_3$, 0.5 M NaCl, pH 9) to a final volume of 100 µl to which 6 µl of NHS-PEG_4-Azide is added. The reaction is allowed to proceed at 25°C for 2 hours while shaking at 1000 rpm. This has the effect of converting approximately 75% of the 64 surface-accessible lysines on the Catalase tetramer to azides. The number of azide labels per protein is determined through MALDI Mass Spectrometry. Each azide label adds 274 Da to the known molecular weight of native *Cg* Catalase (240 kDa). The concentration of the protein is determined using UV-Vis absorption spectroscopy using the known molar extinction coefficient of Catalase at 405 nm (ε_{405} = 324,000 M^{-1} cm^{-1}).

The azide labelled proteins are then exchanged into PBS buffer (0.5 M) and reacted with single stranded synthetic DNA modified with a dibenzocyclooctyne (DBCO) dT phosphoramidite at its 5' terminus. This results in a strain-promoted cycloaddition reaction (Cu-free "click chemistry") between the surface bound azides and the DBCO group on the DNA. Each reaction typically contains 1µM protein and 300 µM DBCO in a total volume of 1 mL and is incubated for 3 days at 25°C while shaking at 1000 rpm. The unreacted DNA are then removed through 10 rounds of ultracentrifugation. The DNA loading density is quantified using UV-Vis spectroscopy and the known molar extinction coefficients of the protein and DNA at 405 nm and 260 nm, respectively. This functionalization strategy results in approximately 44 DNA strands (± 10 %) per protein corresponding to an average surface loading density of 17 pmol/cm^2. To duplex the DNA on the protein, complementary DNA are added at a 100X excess relative to the protein concentration after which the Catalase Pro-SNA are purified by multiple rounds of centrifugation. The Pro-SNA can then be exchanged into the required buffer through ultracentrifugation. A schematic outlining this two-step reaction is provided in Fig.2.1.

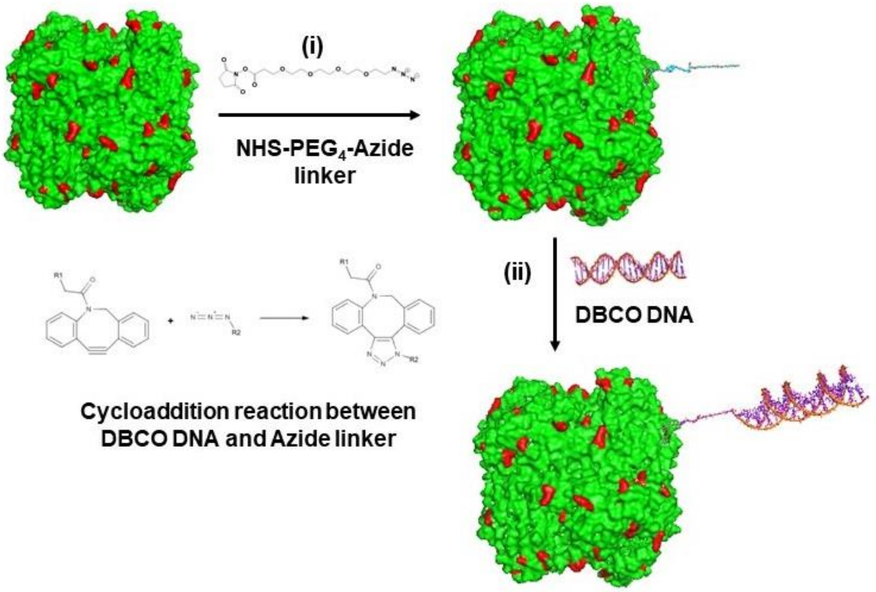

Figure 2.1 : Schematic of the DNA functionalization strategy for Catalase depicting: (i) the functionalization of the surface accessible lysines (red) with an NHS-PEG$_4$-Azide linker and (ii) the cycloaddition reaction (Cu-free "Click chemistry") between the Azide-labelled Catalase and DBCO modified DNA.

2.2. Small Angle X-ray Scattering

Ever since their discovery by Röntgen in 1895, X-rays have been central to deciphering the structure of a staggering range of materials from simple chemical compounds to the notable structure of DNA[41] – the molecule of life. Materials systems including amorphous and crystalline thin films, bulk organic and inorganic materials, proteins and even functional units in living organisms have greatly benefited from X-ray based characterization methods. The power of x-rays to illuminate the atomic-scale structure of materials stems from the fact that their wavelength (~

1 Å) is comparable to typical atomic spacings in materials. The interaction of an X-ray photon with the electrons in an irradiated sample is dominated by two physical processes: absorption and scattering. Elastic scattering, wherein the wavelength of the scattered wave is equal to that of the incident wave is the process that is most commonly utilized for the structural characterization of non-crystalline materials including liquids, glasses, polymers and protein conjugates such as those studied here. The Small Angle X-ray Scattering (SAXS) regime corresponds to the case in which x-rays are scattered by colloidal-sized electron density inhomogeneities in the sample at small scattering angles relative the direction of the incident beam. In a typical SAXS experimental set up (Fig.2.2) a highly monochromatic x-ray beam is incident on a sample from which it is scattered at low angles into a position sensitive detector. The scattered intensity measured in such an experiment may be mathematically expressed as[42]:

$$I(q) = \frac{N}{V}\, \Delta\rho^2\, V_p^2 |F(q)|^2\, S(q) \tag{2.1}$$

Here, the scattered intensity is expressed as a function of q, which is the magnitude of the scattering vector **q** defined as the difference in the wavevectors of the incident and scattered x-rays $\mathbf{k_i}$ and $\mathbf{k_s}$:

$$\mathbf{q} = \mathbf{k_s} - \mathbf{k_i} \tag{2.2}$$

The magnitude of the scattering vector, **q,** is related to the scattering angle 2θ depicted in Fig. 2.2 by the following relation:

$$\mathrm{q} = \frac{4\pi}{\lambda} \sin\theta \tag{2.3}$$

where λ is the wavelength of the incident x-ray photon. $\Delta\rho\ (\rho_p - \rho_s)$ in Eq. 2.1 is the electron density contrast between the scattering particle (ρ_p) and the surrounding solvent (ρ_s), V_p is the volume of the particle and $\frac{N}{V}$ is the concentration of particles. The quantity $F(q)$ is the single particle form factor given by:

$$F(q) = \frac{1}{V_p} \int_{V_p} \rho(\boldsymbol{r}) e^{i\boldsymbol{q}.\boldsymbol{r}} \, dV_p \tag{2.4}$$

where the integral is taken over the volume of the particle V_p , and **r** represents the position of the volume element dV_p. The quantity $S(q)$ is the structure factor which describes inter-particle correlations in the system. For a dilute solution of particles, as is the case in this work, inter-particle interactions may be neglected and $S(q)$ may be assumed to be unity. The expression for the scattered intensity then reduces to:

$$I(q) = \frac{N}{V} \, \Delta\rho^2 \, V_p^2 |F(q)|^2 \tag{2.5}$$

The form factor $F(q)$ depends on the morphology (size and shape) of the particle and may be solved analytically for several simple shapes. These expressions may then to be used to fit the experimentally measured scattered intensity profile in order to extract the structural parameters of the scattering particles. For example, the form factor for a sphere of radius R is given by:

$$F(q) = 3 \left[\frac{\sin(qR) - qR\cos(qR)}{q^3 R^3}\right] \tag{2.6}$$

In the forward scattering direction at q = 0, all the electrons in the sample scatter in phase and consequently, $|F(q)|^2 = 1$. The measured intensity in this case, I (q=0), is then proportional to the squared number of electrons in the sample. Limiting forms of Eq. 2.5 may be used to glean additional insight into the morphology of the particle. In the high-q limit, referred to as the Guinier regime, $qR \rightarrow 0$ and Eq. 2.6 may be expanded and simplified to give:

$$I(q) \approx \frac{N}{V}\, \Delta\rho^2\, V_p^2\, e^{\frac{-q^2 R_g^2}{3}} \tag{2.7}$$

Here R_g is radius of gyration, which for a sphere is related to its radius R by the equation:

$$R_g = \sqrt{\frac{3}{5}}\, R \tag{2.8}$$

A plot of $\ln I\ (q)$ vs. q^2 referred to as a Guinier plot may be used to extract the radius of gyration of scattering objects of various shapes in a model-independent manner.

When qR >> 1, an expansion of the form factor for a sphere results in:

$$I(q) = \frac{2\pi\Delta\rho^2}{q^4} S_p \tag{2.9}$$

where S_p is the surface area of the sphere. Thus, in this limit, called the Porod regime, the SAXS intensity is inversely proportional to the fourth power of q. In the Porod regime, the dependence of the scattered intensity on the wavevector q is dictated by the shape and dimensionality of the particle. For instance, the SAXS intensity falls off as q^{-2} and q^{-1} for particles of dimensionality 2 and 1 such as discs (d = 2) and rods (d =1). Conventional in-situ SAXS measurements and analyses, such as those described above, are central to elucidating the key structural attributes of colloidal dispersions and have been used extensively in this work to determine the concentration, shape, size and electron density distributions of Protein Spherical Nucleic Acid Conjugates. The modelling and analysis of SAXS data collected from Pro-SNAs is described in detail in Chapter 3 and Chapter 4. These measurements have primarily been conducted at the Advanced Photon Source (Sector 5 ID-D). The SAXS/MAXS/WAXS detectors at Sector 5 ID-D (Fig. 2.2) enable a simultaneous collection of data over the SAXS/MAXS/WAXS regimes. The experimental set-up used is described in more detail in the methods section of Chapter 3, Chapter 4 and Chapter 5.

While SAXS is a powerful probe of the properties of the core and shell components of a Pro-SNA, it is insensitive to the weakly scattering cloud of counterions surrounding the construct due to their low electron density contrast with respect to the protein core and DNA shell. The challenge of measuring the structure of this diffuse ionic cloud can be overcome through the use of contrast variation SAXS techniques such as Anomalous Small Angle X-ray Scattering.

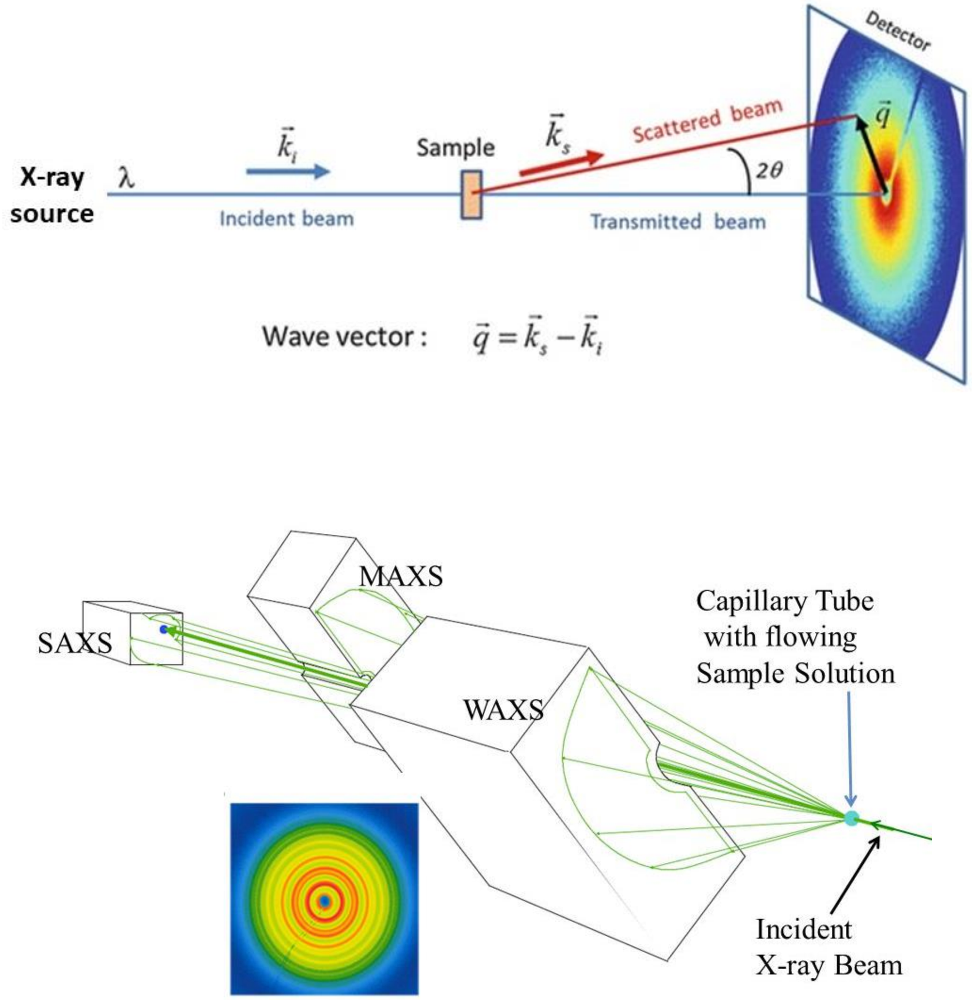

Figure 2.2: Typical SAXS experimental set-up showing an incident x-ray beam with wavelength λ and wavevector k_i and a scattered beam with wavevector k_s and scattering angle 2θ. Also depicted is a schematic of the simultaneous SAXS/MAXS/WAXS detectors and the vacuum flow cell set-up at Sector 5 ID-D at the Advanced Photon source.

2.2.1. Anomalous Small Angle X-ray Scattering

Anomalous Small Angle X-ray Scattering (ASAXS) exploits the variation in the effective scattering strength of an element close to an absorption edge to enable the element-sensitive deduction of the spatial distribution of an ionic species within a complex sample. When the energy of the incoming x-ray photon is approximately equal to the binding energy of a core-shell electron in an atom or ion, the radiation is absorbed resulting in a sharp discontinuity in the linear absorption coefficient of the species. In vicinity of this energy, referred to as an absorption edge, the form factor of the ion becomes a complex function of the energy E of the incident radiation and takes on a form given by:

$$f(q,E) = f_0(q) + f'(E) + if''(E) \tag{2.10}$$

The first term of the form factor, $f_0(q)$, is an energy-independent, non-resonant term that is equivalent to the number of electrons of atomic or ionic species under consideration. The energy-dependent terms $f'(E)$ and $f''(E)$ are called the dispersion corrections and change dramatically close to an absorption edge as seen for the case of Rubidium in Fig. 2.3. Thus, f', which goes sharply negative near the edge, causes an effective reduction in the number of scattering electrons in the ion of interest. Through the use of a synchrotron radiation source, the energy of the incoming x-ray photon may be tuned to the absorption edge of a specific element to probe its spatial distribution within a system. For a dilute system of non-interacting macromolecules along with their charge compensating counterions, it has been shown that the SAXS intensity measured close to an absorption edge of the counterionic species can be written as[43]:

$$I(q,E) = F_0^2(q) + 2f'(E)F_0(q)v(q) + \left(f'^2(E) + f''^2(E)\right)v^2(q) \tag{2.11}$$

The first term of the above equation is the non-resonant scattered intensity measured from the macroion-counterion system at energies far removed from the x-ray absorption edge. The second term is a resonant cross term containing the real part of the anomalous dispersion correction $f'(E)$ and the Fourier transform of the excess counterion density distribution, $v(q)$:

$$v(q) = \int_0^\infty [\rho_{ion}(r) - \rho_{bulk}]\, e^{i\boldsymbol{q}.\boldsymbol{r}}\ dV \tag{2.12}$$

The term $v(q)$ encodes information about the spatial distribution of the excess counterions in the system. The third resonant term in the equation arises purely due to scattering from the counterions. In a typical ASAXS experiment these three partial intensities may be extracted by measuring the scattered intensity from the system at several incident photon energies below the absorption edge of the element of interest. Such measurements are generally performed at energies below the absorption edge in order to avoid strong background fluorescence. By sampling $I(q, E)$ at different values of $f'(E)$, each of the terms may be isolated over the relevant q range through the application of an appropriate regression function. These terms may then be fit with appropriate models

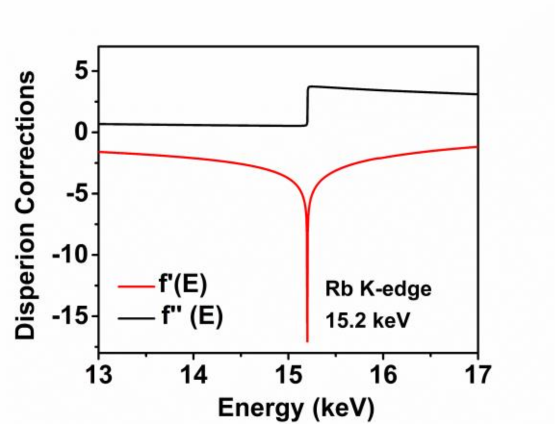

Figure 2.3: Anomalous Dispersion Corrections f'(E) and f'' (E) as a function of incident photon energy for Rubidium in the vicinity of its K-absorption edge at 15.2 keV.

corresponding to the structure of the macroion and the distribution of the counterions to ascertain local ionic concentrations surrounding the macroion. It should be noted here that for the case of Rb depicted in Fig. 2.3., the value of $f''(E)$ below the edge is negligible, and we may approximate $f''(E) \approx 0$, further simplifying Eq. 2.11. The ASAXS method detailed here has been applied to decipher the distribution of counterions surrounding Pro-SNAs and is described in greater detail in Chapter 2 and Chapter 4.

2.3. SDS Polyacrylamide Gel Electrophoresis

Sodium Dodecyl Sulphate Polyacrylamide Gel Electrophoresis (SDS PAGE) is an analytical technique commonly used to purify, separate and characterize the molecular weight of proteins in a mixture. SDS PAGE is based on the differential electrophoretic mobility of proteins governed by their molecular weight.

The migration of a charged molecule under the influence of an applied electric field depends on the strength of the field, the net charge and molecular radius. The net charge and molecular radius of a natively folded protein are however, not dependent on its molecular weight. To overcome this limitation, the proteins are first denatured through the addition of a reducing agent such as dithiothreitol which has the effect of cleaving the disulphide bonds which hold together the tertiary structure of proteins. This ensures that all the proteins under consideration have a consistent linear conformation. In order to confer all the proteins with a roughly equivalent net charge, an anionic detergent, Sodium Dodecyl Sulphate is added to the aqueous suspension of proteins. SDS binds at a constant level per amino acid residue on the protein at a rate of 1.4 g SDS/1g protein as a result of which the charge on the protein becomes proportional to its molecular weight. As a result of this process, the proteins in the mixture are converted into linear molecules with a length proportional to their molecular weight.

An aqueous solution of these SDS decorated proteins are then applied to a cross-linked polyacrylamide gel matrix held between a negative (top) and positive (bottom) electrode across which an electric field is applied. The rate of migration of the negatively charged proteins towards the cathode through the pores in the gel matrix is governed by their molecular radius and hence molecular weight as a result of which lighter proteins migrate further through the gel than heavier ones. Empirically it is found that the distance travelled by a protein along a gel is approximately a linear function of log (1/M), where M is the molecular weight of the protein. To determine the molecular weight of an unknown protein, it is typically run against a reference “protein ladder” consisting of proteins with known molecular masses. The operating principle and apparatus of a typical SDS PAGE experiment and the resultant gel image are depicted in Fig. 2.4. The use of SDS PAGE to characterize Pro-SNAs and their enzymatic degradation pathway is described in Chapter 4.

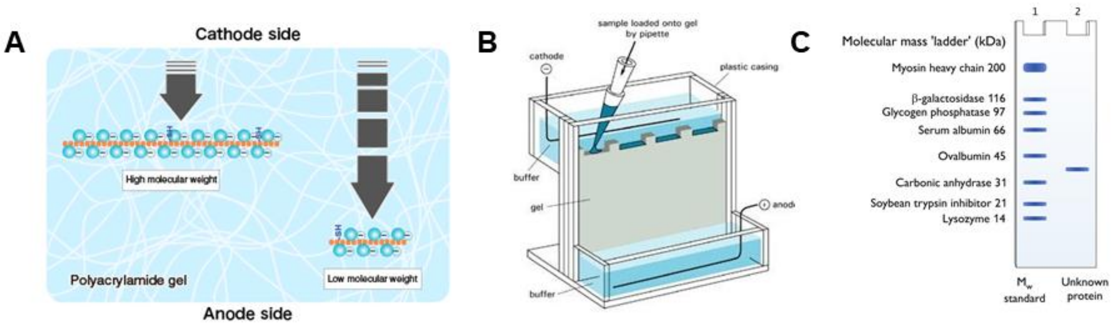

Figure 2.4: (A) An illustration of the differential migration of molecules of differing molecular weights through a polyacrylamide gel. (B) Typical SDS PAGE apparatus (C) Illustrative PAGE gel showing bands from a reference protein ladder and an unknown protein.

2.4. Dynamic Light Scattering

Dynamic Light Scattering is a light scattering method typically employed to probe particle size and polydispersity on the sub-micron length scale. The technique exploits the interaction of laser light (typical wavelength ~ 600 nm) with particles undergoing random Brownian motion as a result of collisions with solvent molecules. The velocity of the particles undergoing Brownian motion is defined by a quantity called the translational diffusion coefficient (D), which is related to the hydrodynamic diameter (d (H)) of the particles through the Stokes-Einstein equation:

$$d(H) = \frac{kT}{3\pi\eta D} \tag{2.13}$$

Here k is Boltzmann's constant and T and η are the absolute temperature and viscosity of the surrounding medium, respectively. The viscosity of the solvent depends on the temperature thus highlighting the need to maintain a stable temperature throughout the measurement. Further, fluctuating temperatures could result in convection currents within the sample causing non-random particle movements that would lead to a misinterpretation of size. The hydrodynamic diameter above is the diameter of a sphere that has the same diffusion coefficient as the particle under consideration. Since the particles in the dispersion are in a constant random Brownian motion, the intensity of the scattered light experiences fluctuations with a period that is characteristic to the size of the particles with small particles causing more rapid fluctuations than larger ones as shown in Fig. 2.5. In order to determine particle size through a measurement of the scattered intensity, most DLS instruments employ an autocorrelation function, $G(\tau)$, which represents a time average of the scattered intensities sampled over small intervals of time τ:

$$G(\tau) = \langle I(t)I(t+\tau)\rangle \tag{2.14}$$

For a large number of monodispersed particles undergoing Brownian motion, it has been shown that the autocorrelation function is an exponentially decaying function of the correlator time delay τ :

$$G(\tau) = A[1 + Be^{-2\Gamma\tau}] \tag{2.15}$$

where A and B are the baseline and intercept of the correlation function. The quantity Γ is then related to the diffusion coefficient D through:

$$\Gamma = Dq^2 \tag{2.16}$$

where,

$$q = \frac{4\pi n}{\lambda}\sin\frac{\theta}{2}$$

Here, n is the refractive index of the solvent, λ is the wavelength of the incident light and θ

is the scattering angle. A schematic of a typical DLS experiment and examples of autocorrelation functions obtained for large and small particles are depicted in Figure 2.5. DLS has been used in this thesis to determine the size and degree of monodispersity of native and DNA functionalized proteins.

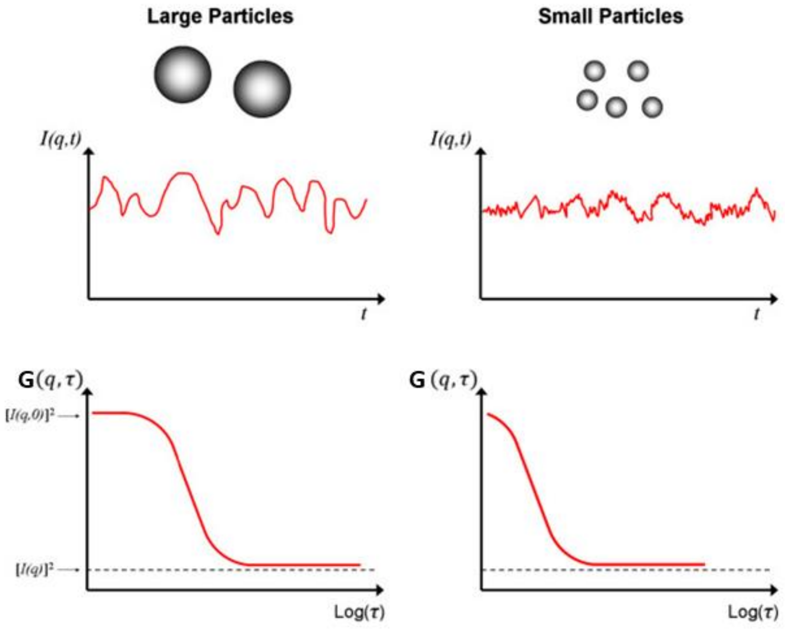

Figure 2.5: Fluctuations in the measured scattered intensity as a function of time from large particles (left) and small particles (right) and their corresponding autocorrelation functions $G(\tau)$.

2.5. Circular Dichroism Spectroscopy

Circular Dichroism (CD) spectroscopy exploits the differential interaction of optically active chiral molecules with polarized light to investigate their physical and chemical properties. When a molecule contains one or more chiral chromophores, it absorbs left and right circularly polarized light to different extents thus giving rise to a CD signal:

$$\Delta A(\lambda) = A_l(\lambda) - A_r(\lambda) \tag{2.17}$$

Here, A_l and A_r are the absorbances of the left and right circularly polarized light at a specified wavelength λ. This equation can be recast in an alternative form through the application of Beer's Law to give:

$$\Delta A(\lambda) = \big(\varepsilon_l(\lambda) - \varepsilon_r(\lambda)\big)Cl \tag{2.18}$$

where $\varepsilon_l(\lambda)$ and $\varepsilon_r(\lambda)$ are the extinction coefficients for left and right circularly polarized light, C is the molar concentration and l is the path length in centimeters. Then, the molar circular dichroism is given by:

$$\Delta\varepsilon\,(\lambda) = \varepsilon_l(\lambda) - \varepsilon_r(\lambda) \tag{2.19}$$

The main application of Circular Dichroism spectroscopy lies in the study of biological macromolecules such as proteins, DNA and RNA due to their inherently highly chiral chemistries. In such applications, the CD signal from an aqueous suspension of biomolecules is measured over a range of wavelengths spanning Ultraviolet and visible regions of the spectrum. The resulting radiation becomes elliptically polarized upon passing through the circular dichroic sample and hence most instruments report CD spectra in units of ellipticity corrected for concentration and path length called the molar ellipticity. Molar circular dichroism and molar ellipticity ($[\theta]$) are related by the expression:

$$\Delta\varepsilon = \frac{[\theta]}{3298.2} \tag{2.20}$$

The secondary structure of proteins lends itself extremely well to study by CD spectroscopy. In particular, structural elements such as α-helices and β-sheets have signature CD spectra which can be used to characterize their relative abundance within a protein structure. The characteristic CD spectra associated with the α-helix and β-sheet are shown in Fig. 2.6 below. Further, since the secondary structure of proteins is extremely sensitive to environmental parameters such as pH, temperature and ionic strength, CD can be used to track changes in the structure of the molecule. The commonly occurring conformations of DNA such as A, B and Z-form DNA also have signature CD spectra. Thus, in this thesis, CD spectroscopy has been used to probe the secondary structures of native and DNA modified proteins (Appendix, A5).

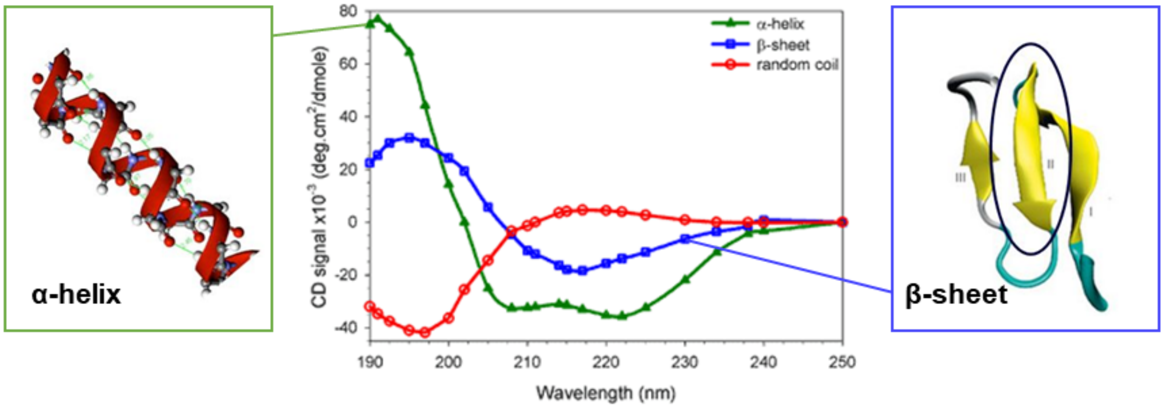

Figure 2.6: Characteristic CD spectra of the α-helix (green) and β-sheet (blue) elements of protein secondary structure.

Chapter 3: Defining the Structure of a Protein Spherical Nucleic Acid Conjugate and its Counterionic cloud

Abstract

Protein spherical nucleic acid conjugates (Pro-SNAs) are an emerging class of bioconjugates that have properties defined by their protein cores and dense shell of oligonucleotides. They have been used as building blocks in DNA-driven crystal engineering strategies and show promise as agents that can cross cell membranes and effect both protein and DNA-mediated processes inside cells. However, ionic environments surrounding proteins can influence their activity and conformational stability, and functionalizing proteins with DNA substantively changes the surrounding ionic environment in a non-uniform manner. Techniques typically used to determine protein structure fail to capture such irregular ionic distributions. Here, we determine the counterion radial distribution profile surrounding Pro-SNAs dispersed in RbCl with 1 nm resolution through *in-situ* anomalous small angle X-ray scattering (ASAXS) and classical density functional theory (DFT). SAXS analysis also reveals the radial extension of the DNA and the linker used to covalently attach the DNA to the protein surface. At the experimental salt concentration of 50 mM RbCl, Rb^+ cations compensate ~90% of the negative charge due to the DNA and linker. Above 75 mM, DFT calculations predict overcompensation of the DNA charge by Rb^+.This study suggests a method for exploring Pro-SNA structure and function in different environments through predictions of ionic cloud densities as a function of salt concentration, DNA grafting density, and length. Overall, our study demonstrates that solution X-ray scattering combined with DFT can discern counterionic distribution and submolecular features of highly charged, complex nanoparticle constructs such as Pro-SNAs and related nucleic acid conjugate materials.

Introduction

The structure and function of biological macromolecules are intimately coupled to their ionic environment. For example, protein turnover and enzymatic catalysis both depend on electrostatic interactions.[44] The local electrostatic environment can affect the pK_a values of critical amino acids involved in acid/base catalysis[44] while substrates are guided to the active site via electric potentials.[45] Electrostatic interactions dictate both local and long-range structure. For instance, the association of oligonucleotides with charge-compensating multivalent counterions induces the condensation and packaging of viral genomes,[1, 46] the asymmetric charge distribution of cations around DNA stabilizes specific DNA conformations,[47] and crystallization via the "salting out" effect enables the determination of many protein structures via X-ray crystallography.[48] Also, salt concentration and pH influence the folding and denaturation of proteins, which dictate their biological function.[49-50] These examples suggest that the structure and functionality of bio-nanoconstructs formed by functionalizing proteins with nucleic acids [e.g. protein spherical nucleic acid conjugates (Pro-SNAs)][51] should be highly sensitive to their ionic environment.

Certain Pro-SNA conjugates (e.g. Fig. 3.1) retain the native enzymatic functionality of the protein core[51] and exhibit advantageous characteristics that arise from their dense DNA coating. For example, they are internalized by cells without the need for transfection agents,[36, 51] and have been used as building blocks for protein crystal engineering via deliberately designed Watson-Crick hybridization interactions between DNA on neighboring proteins.[37, 51] Pro-SNAs and related structures that differ in core shape but with comparable DNA densities also exhibit characteristics common to conventional Au-SNAs,[5] such as the enhanced resistance of the tethered DNA to enzymatic degradation[16] and cooperative melting behavior of their DNA-linked assemblies.[13] These properties are hypothesized to arise, in part, due to high local concentrations of cationic counterions associated with these negatively charged nanoparticles. Indirect evidence that the structure of the ion cloud surrounding Pro-SNAs influences inter-Pro-SNA interactions as well the interaction of Pro-SNA with other types of SNA conjugates is obtained in studies on crystallization via Watson-Crick hybridization. This method has been used to induce the assembly of Pro-SNAs, or combinations of Pro-SNAs and AuNP-SNAs, into crystalline superlattices.[21] In the latter case, varying the salt concentration, which directly affects the ion distribution and the range and strength of the interaction between SNAs,[52] induced transitions between distinct crystalline phases.[53] Thus, a thorough elucidation of the ionic environment surrounding Pro-SNA conjugates would enable a deeper understanding of their properties, and support future efforts to exploit the structure-function relationships of Pro-SNAs, as well as the related class of high density DNA-functionalized nanomaterials for diagnostic,[54-55] therapeutic,[17, 56] and crystal engineering applications.[6, 8, 57]

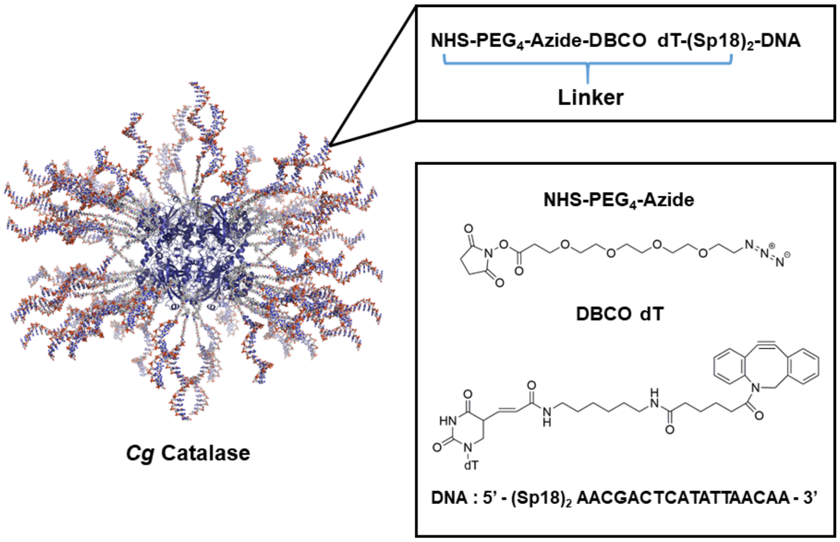

Figure 3.1: Schematic illustration of *Cg* Catalase functionalized with 18 base long ss-DNA. Each strand is composed of a linker region comprised of an NHS-PEG$_4$-Azide moiety and a DBCO dT group covalently anchoring the DNA to the protein surface (*inset)*.

As illustrated in Fig. 3.1, the Pro-SNA conjugate employed in this study is composed of a *Corynebacterium Glutamicum* (Cg) Catalase core that is densely grafted with ~ 40 DNA strands that are 18 base-long via a two-step synthetic scheme where: (1) surface amines are converted to azides and (2) azides are reacted with oligonucleotides containing a terminal strained cyclooctyne (DBCO). (For details, see *Materials and Methods.*) The oligonucleotide (D) is anchored to the protein core via a linker region (L) consisting of a tetraethylene glycol spacer from the NHS polyethylene glycol (PEG)$_4$ crosslinker, a spacer between the DBCO and thymidine moieties of the DBCO dT synthetic phosphoramidite, and two hexaethylene glycol spacers introduced at the

5’-terminus of the oligonucleotide during synthesis. These Pro-SNAs were dispersed in 50 mM RbCl to a final concentration of 1 μM or 4 μM.

Small angle X-ray scattering (SAXS) is an ideal *in situ* probe for characterizing the structure of nanoscale particles due to the penetrating power and small wavelength (~ 1 Å) of high energy X-rays. However, while SAXS can resolve the size of the Pro-SNA conjugate, the electron density contrast between the Pro-SNA conjugate, counterions and surrounding solvent is not sufficient to distinguish the distribution of ions surrounding the particle. For this we turn to anomalous SAXS (ASAXS), which can be used to provide elemental specificity to sense the scattering contribution from ions surrounding the particle. ASAXS has been successfully employed to extract the ion density[31, 58-59] surrounding double stranded DNA[60-61] and polymer brushes.[31] Although ASAXS could not be used to determine the counterion distribution surrounding Au-SNAs due to the strong scattering from the electron dense Au cores,[32] the relatively low electron density of the protein core in a Pro-SNA enables the use of ASAXS in this case. As described below, Rb^+ is chosen as the monovalent counterion for Pro-SNAs because its core electron binding energy ($E_K = 15.200$ keV) is sufficiently high for solution ASAXS, which necessitates the use of high energy X-rays (E >~ 10 keV) to overcome the X-ray absorption in the aqueous medium.

ASAXS deduction of the counterionic distribution profile relies on the measurement of subtle changes in the X-ray energy (E) dependent scattering from the overall particle-counterion system. These changes arise due to a sharp reduction in the scattering strength of the selected counterion species at X-ray energies close to one of its core electron binding energies (absorption edge). At X-ray energies below an absorption edge, the background subtracted intensity from non-interacting, isolated particles in solution is approximately (Appendix A1, Sec.A1.1):

$$\Delta I(q,E) = \frac{N}{V}[|F_0(q)|^2 + f'(E)(2F_0(q)v(q))] \tag{3.1}$$

where $q = 4\pi \sin\theta/\lambda$ is the modulus of the scattering vector, 2θ is the scattering angle, and λ is the wavelength of the incident X-rays. Here N/V represents the concentration of particles (Pro-SNAs in this case). $F_0(q)$ is the form factor from a single Pro-SNA, which includes contributions from the associated excess counterions (here, Rb^+), at an X-ray energy far below a Rb^+ absorption edge (here, K edge: E_k = 15.200 keV). Therefore, $|F_0(q)|^2$ is the non-resonant contribution to the scattered intensity from a single Pro-SNA with its associated, excess Rb^+ ions. The resonant second cross-term contains the dispersion correction $f'(E)$. This is a negative number (Fig. 3.2(A), Appendix A1, Sec.A1.2), which accounts for the reduction in the effective number of electrons [$f_0 + f'(E) = 36 + f'(E)$] that contribute to the scattering from a single Rb^+ ion near E_k.[62] Most importantly, the cross-term also contains $v(q)$, the Fourier transform of the excess Rb^+ density$[n_{Rb+}(r) - n_b]$, where n_b represents the bulk Rb^+ number density.

It is important to note that the native Catalase protein has an isoelectric point (pI) of 5.4.[63] Thus, at neutral pH, the contribution of the protein core to the overall charge of the Pro-SNA is minimal[64] [-17 for the protein core (Appendix A1, Fig.A1.3) vs. -840 for the linker and DNA shell]. ASAXS measurements on unmodified proteins (Appendix, Fig.A1.3 and text in Sec. A1.3) support the assumption that the protein core does not exhibit an appreciable effect on the counterion distribution.

Materials and Methods

1. Sample preparation

All the oligonucleotides used in this study were synthesized on controlled pore glass (CPG) solid supports on a MM48 BioAutomation DNA synthesizer or an ABI 392/394 synthesizer using reagents from Glen Research. The synthesized DNA strands were subsequently purified using RP-HPLC on a Varian ProStar HPLC system. The base sequence of the single stranded DNA used is as follows: 5'- DBCO dT- $(Sp18)_2$- AACGACTCATATTAA CAA-3'. DBCO dT refers to a dibenzocyclooctyne phosphoramidite (Fig.3.1) and Sp18 refers to a hexa-ethylene glycol spacer. The oligonucleotides were conjugated to proteins using previously established methods.[51]

Briefly, Catalase from Corynebacterium Glutamicum was obtained from Sigma Aldrich (Product number: 02071) and suspended in a buffer containing 100 mM sodium bicarbonate (pH 9.0, 0.5 M NaCl) by ultrafiltration. The concentration of the protein was determined by UV-vis absorption spectroscopy using a molar extinction coefficient (ε_{405}) of 324,000 M^{-1} cm^{-1}.[63]

The surface-accessible amine functional groups on the protein were converted into azides by adding 6 mg of tetraethylene glycol linkers containing an *N*-hydroxy-succinimide (NHS) ester and an azide group on opposing termini (Fig. 3.1) to a 100-µL solution containing 50 µM protein. This reaction was then allowed to proceed for 2 hours at 25° C while shaking at 1000 rpm on a Benchmark Multitherm shaker. The unreacted linkers were then removed by five rounds of ultracentrifugation after which the number of azide labels on the protein was determined by MALDI mass spectrometry. The difference in the observed mass of the native and azide-labelled enzyme was used to quantify the number of azide linkers per protein by making use of the fact that each attached linker adds a mass of 274 Da to the mass of the native protein.[51]

These azide-modified proteins were then functionalized with DBCO modified DNA through the use of a strain promoted cycloaddition reaction (Cu-free “click chemistry”) between the surface bound azides on the protein and the DBCO moieties on the 5’ end of the synthetic oligonucleotides. Each protein-DNA functionalization reaction typically contained 1 μM protein and 300 μM DNA (300 X excess) suspended in phosphate buffered saline (PBS). This reaction was incubated for 3 days at 25°C while shaking at 1000 rpm on a Benchmark Multitherm shaker, after which the unreacted DNA was removed by 10 rounds of ultrafiltration using Millipore Amicon Ultra 100 KDa centrifugal filter units. The DNA loading density was determined by using UV-vis absorption spectroscopy with the appropriate molar extinction coefficients for the protein (ε_{405} = 324,000 M^{-1} cm^{-1}) and DNA (ε_{260} = 188,300 M^{-1} cm^{-1}). The Pro-SNA conjugates were then exchanged into 50 mM RbCl prior to the SAXS measurements.

2. X-ray Measurements

All the SAXS measurements were performed at beamline 5 ID-D of the Advanced Photon Source at the Argonne National Lab. In order to avoid strong fluorescence at and above the Rb K-edge (15.2 keV), SAXS measurements were performed at four incident X-ray energies below the absorption edge (summarized in Fig. 3.2A (inset)). The spot size of the incident beam at the sample was 0.25×0.25 mm^2 and the average incident flux was ~ 10^{11} photons/sec. In order to minimize air scattering, a capillary tube housed in an in-vacuum flow cell was utilized. Additionally, the entire beam path was also placed under vacuum. An ion chamber positioned before the flow cell was used to monitor the flux of incident beam, while a cadmium tungstate scintillating crystal followed by a pin diode embedded in the beam stop was used to monitor the transmitted beam.

The intensities of the incident and transmitted beams were used to normalize the scattered intensities collected on a Rayonix area detector placed at 7.5 m from the sample (accessible range of $q \sim 0.022 - 1.35$ nm^{-1} at 15 keV).

To prevent radiation damage, the entire sample volume was continuously flowing at 3 mm/s through the 1.5 mm diameter quartz capillary during data collection. The measurements were carried out at room temperature. At each energy, 5 frames were collected with an exposure time of 3 seconds per frame. For a given protein concentration, all the measurements were performed using the same capillary tube. The capillary was thoroughly washed with ~ 10 ml of pure water and sodium hydroxide between measurements.

To ensure that the background signal was unchanged due to particle aggregation or sticking, SAXS profiles of the empty capillary, water and 50 mM RbCl buffer were collected before and after each sample measurement. Five frames were collected with an exposure time of 10 seconds/frame for the empty capillary, water and buffer. The 1D scattered intensity profiles for the sample, empty capillary, water and buffer were obtained through azimuthal integration of the collected 2D SAXS patterns, while taking into account the solid angle, flat-field, transmission and polarization corrections.

The data were converted to an absolute scale following standard procedures.[65] Briefly, the data from pure water, obtained as the difference between the scattered intensities from the capillary filled with water and the empty capillary, were fitted with straight lines. The intercept of these best-fit lines through the near constant water scattering was set at 0.0165cm^{-1}, which is the absolute intensity (scattering cross section/volume) for water at $T = 25$ °C.[65] Thereafter, all the data were scaled accordingly.

3. Density Functional Theory (DFT)

The Boltzmann distribution of Rb^+ and Cl^- was calculated using classical density functional theory.[32, 66] A conical unit cell was used, where the two axes represent the distance from the protein center and the polar angle with a DNA strand. This cone was symmetric about rotation along the radial axis. Therefore, a 2D grid was used, with the spacing in the radial direction given by 0.05 Debye lengths and 0.005 radians in the θ direction. The maximum angle was calculated by dividing the solid angle of a sphere evenly among the 40 DNA chains. The maximum radius extends 8 Debye lengths from the end of the DNA.

An impervious and uncharged spherical core with the SAXS-derived R_{prot} = 4.5 nm and a DNA loading density of 40 strands/particle was used. The region surrounding the protein where the linkers connect it and the DNA was modeled with a -3 charge distributed uniformly across the volume. The ssDNA was modeled as a -18 charge with the distribution given as the product of three hyperbolic tangent functions with slopes of 1.2. These functions represent the boundaries of the beginning of the DNA, the diameter of the DNA at 1.2 nm, and the end of the DNA. The diameter of the cation and anion used were 0.298 and 0.362 nm, in order to represent hydrated Rb^+ and Cl^- respectively. The concentration of the salt reservoir was 50 mM.

The average concentration of ions was calculated as a function of distance from the nanoparticle center. $Rb^+(r, \theta)$ densities were angle-averaged to obtain r-dependent Rb^+ density profiles $(n_{Rb+}(r) - n_b)$. $v(q)$, the Fourier transform of the average cation density difference with the bulk, was then calculated using trapezoidal integration. The form factor $F_0\ (q)$ obtained from fitting of the non-resonant intensities and the Pro-SNA concentrations (Fig. 3.4 and Table 3.1) was finally multiplied with $\nu(q)$ to produce a series of calculated cross-term profiles $\frac{N}{V}[2F_0\,(q)\nu(q)]$.

The size of linker and ssDNA regions are unknown. These were allowed to vary in 0.5 nm increments in order to minimize the difference between the Huber error of the expected resonant intensity and the predicted resonant intensity.

Results and Discussion

ASAXS possesses the sensitivity needed to resolve the counterionic structure for our Pro-SNA case, as demonstrated by the following model calculations. The two terms in Eq. 3.1 are calculated for f'_{Rb} = -7.58, corresponding to an incident photon energy 5 eV below the Rb^+ K-edge. For these calculations, we assign uniform electron densities to the protein core and DNA shell, and further assume that the distribution of Rb^+ ions within the shell falls off as the inverse square of the radial distance from the surface of the core (Appendix A1, Sec.A1.1). The scattered intensity (Fig. 3.2B) is dominated by the non-resonant term $|F_0(q)|^2$ while the modulus of the resonant term $|2F_0(q)f'(E)v(q)|$ is an order of magnitude lower in intensity. This demonstrates the inherent challenge of ASAXS in this case. Nevertheless, we show that the Fourier transform $v(q)$ can be extracted over a sufficiently large range of q to determine the counterion distribution profile with nanometer-resolution.

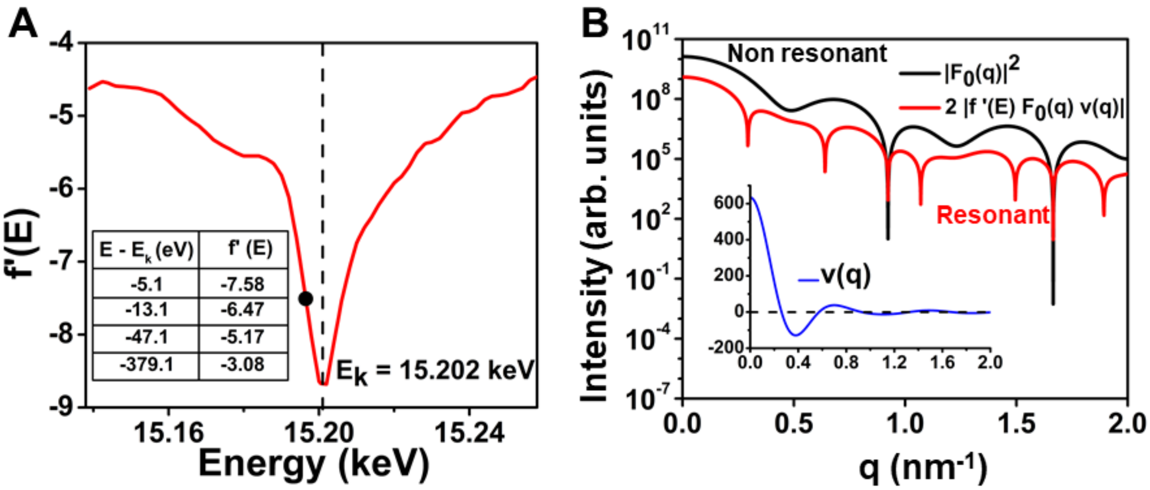

E - E$_k$ (eV)	f' (E)
-5.1	-7.58
-13.1	-6.47
-47.1	-5.17
-379.1	-3.08

Figure 3.2: (A) Experimentally determined anomalous dispersion correction *f'* (*E*) for Rb as a function of incident X-ray energy near the Rb K-edge (see also Appendix A1 Fig. A1.2). (B) Model SAXS intensity calculations of the non-resonant term (black) and the magnitude of the resonant (at E = E$_K$ – 5 eV) term (red) in Eq. 3.1. The positions of the sharp minima that are exclusive to the resonant term magnitude correspond to the q-values where v (q) changes sign (Inset, blue).

The radial distribution profile of Rb$^+$ was obtained from a comparison of the cross-term $\frac{N}{V}\,2F_0(q)v(q)$ profile with classical-DFT calculations, while characteristics of the Pro-SNA conjugate, such as the size of the protein core and DNA shell, were determined by fitting the non-resonant intensity profile $\frac{N}{V}|F_0(q)|^2$ with parameterized geometric models. These two terms are separated out by a simultaneous analysis of the background subtracted SAXS intensity profiles ΔI

(q, E) at four different X-ray energies below the Rb$^+$ K-edge, which are shown for the case of 4 μM Pro-SNA in 50 mM RbCl in Fig. 3.3A.

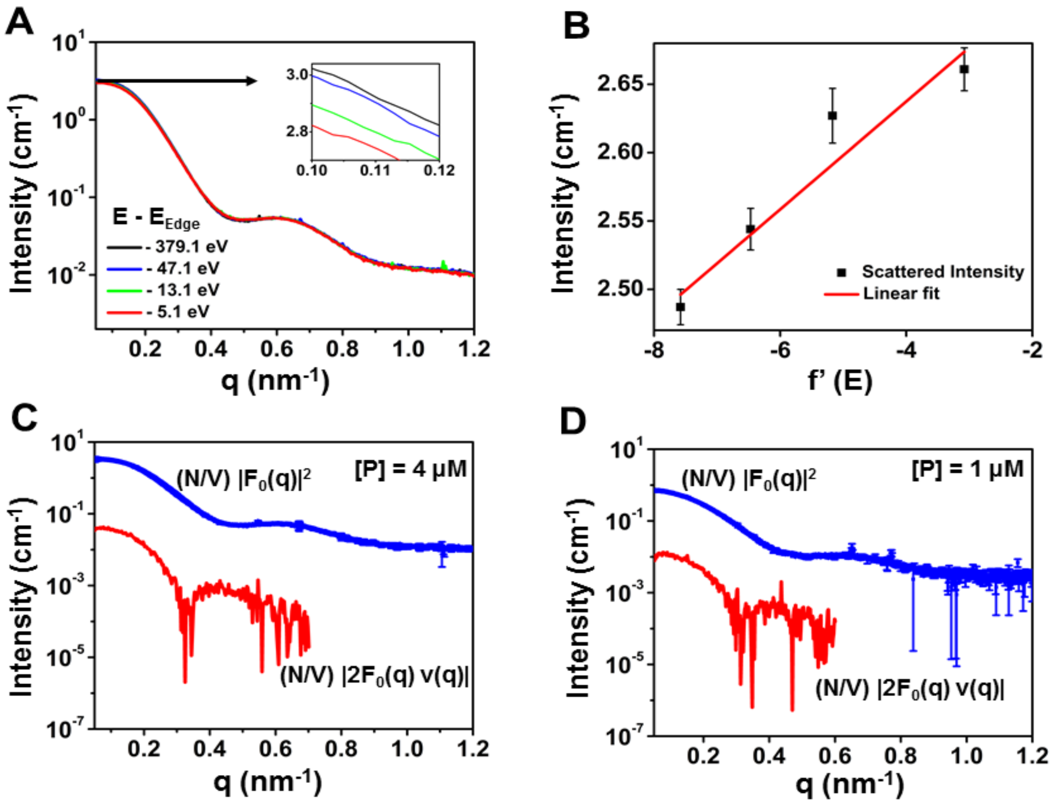

Figure 3.3: (A) Background subtracted SAXS intensity profiles at four incident energies below the Rb K-edge, with a magnified view at low q (inset). (B) Linear fit to the SAXS intensities ΔI (q, E) vs f' (E) at $q = 0.13$ nm^{-1}. (C) & (D) Extracted non-resonant (blue) and cross-term (red) profiles (Eq. 3.1) for 1 μM and 4 μM Pro-SNA in 50 mM RbCl.

The four intensity profiles are easily distinguishable at low q when plotted on a linear scale (Fig. 3.3A inset). At low q, ΔI (q, E) and therefore $2f'(E)[F_0(q)\nu(q)]$, monotonically increase with increasing $E_k - E$. This is the expected trend based on the E-dependence of f' (Fig. 3.2A) and because $F_0(q)$ and $v(q)$ are positive at low q. These observations imply that the non-resonant term $\frac{N}{V}|F_0(q)|^2$ and the cross-term $\frac{N}{V}\ 2F_0(q)v(q)$ can be separated out as the intercepts and the slopes of the linear fits to the four $[f'(E), \Delta I\ (q, E)]$ data points at each q, over an extended q–range (see also Appendix A1, Sec.A1.4). An example of such a linear fit of $\Delta I(q,E)$ vs. $f'(E)$ at q = 0.13 nm^{-1} is shown in Fig. 3.3B. Eq.3.1 used for the decomposition described above is an approximation because it assumes a linear dependence between $\Delta I(q,E)$ and $f'(E)$. The full form of the ASAXS equation is quadratic in $f'(E)$ due to a third purely resonant term – $[f'(E)v(q)]^2$. However, in our case this approximation is valid due to the relatively low magnitude of this term as demonstrated by model ASAXS calculations and an analysis of experimental data (Appendix A1, Sec.A1.1). The non-resonant term $|F_0(q)|^2$ and cross-term $|2F_0(q)v(q)|$ are shown in Figs. 3.3C and 9D for the cases of 4 μM Pro-SNA and 1 μM Pro-SNA in 50 mM RbCl, respectively. In both cases, the profile $\frac{N}{V}|2F_0\ (q)v(q)|$ is reported only up to q = 0.7 nm^{-1} due to uncertainties greater than 70% beyond this q (Appendix A1, Fig. A1.4). As shown below, the extracted profiles (non-resonant and cross-terms) for the two concentration cases differ by a multiplicative constant $(\frac{N_1V_2}{V_1N_2})$ but are otherwise identical. These observations demonstrate reproducibility and prove that for the concentrations used in this study, the Pro-SNA behave as isolated particles. That is, the results discussed here are devoid of any interparticle interaction effects.

A visual examination shows drastic qualitative differences between the extracted $\frac{N}{V}|F_0(q)|^2$ and $\frac{N}{V}|2F_0\ (q)v(q)|$ profiles (Figs. 3.3C-3.3D). Specifically, in qualitative agreement with model calculations in Fig. 3.2B, for both the 1 and 4 μM Pro-SNA cases the first minimum of the

$\frac{N}{V}|2F_0\,(q)v(q)|$ profile occurs at q ~ 0.30 nm^{-1} in comparison to the first minimum at q ~ 0.47 nm^{-1} for the non-resonant ($\frac{N}{V}\,|F_0(q)|^2$) intensity profile. This difference is clearly due to the effect of $v(q)$ - the Fourier transform of the excess Rb$^+$ density. As shown through detailed quantitative analysis below, the difference arises because of the absence of Rb$^+$ in the core (protein) region and because the Rb$^+$ distribution extends beyond the DNA shell. The above qualitative comparison between the two extracted profiles demonstrates that ASAXS is sensitive to $v(q)$ and hence the Rb$^+$ distribution surrounding Pro-SNA.

We first describe the structural attributes of the Pro-SNA conjugate, deduced from fitting the non-resonant $\frac{N}{V}|F_0(q)|^2$ intensity profiles in Figs. 3.3C-3.3D with a spherical core-shell model (Appendix A1, Sec. A1.6). By fitting the SAXS intensity profile of a bare protein without DNA (Appendix A1, Fig. A1.5) to the form factor for a homogenous sphere, the parameters for the protein core were fixed. This fit yielded a radius R_{prot} = 4.5 nm (Appendix A1, Sec.A1.5), which corresponds to a radius of gyration $R_g = \sqrt{(3/5)} \times R$ = 3.5 nm. Our simplified approach agrees well with the value obtained using CRYSOL[67] software (R_g = 3.7 nm), which employs a fully atomistic model derived from diffraction experiments on Cg-Catalase single crystals[68]. The non-resonant contribution to the total scattered intensity from the Pro-SNA, $|F_0(q)|^2$, was thereafter fit (Fig. 3.4A) by a spherical core-shell model (Fig. 3.4B). The DNA and linker segments were modeled as cylinders each with a fixed radius of 0.5 nm and fixed number of electrons based on chemical composition (Appendix A1, Sec. A1.6). The protein concentration and the lengths of the linker and DNA were used as fitting parameters. As expected, the best-fit values of the linker and DNA lengths (summarized in Table 3.1) are in close agreement for the two protein concentrations, with deviations being within the uncertainties of the fit parameters. A detailed analysis of the cross-term profiles allows extraction of the Rb^+ radial distribution.

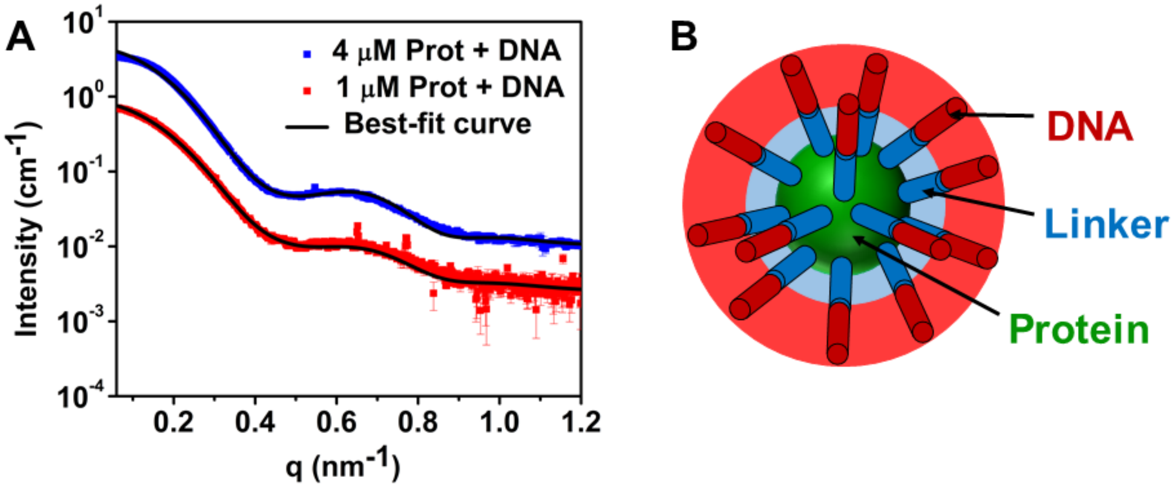

Figure 3.4: (A) Fit of the extracted non-resonant term to a core-shell model of the Pro-SNA conjugate. The multiplicative offset between the two SAXS profiles (4) is consistent with the ratio (4) of the nominal protein concentrations. (B) Cartoon representation of the core-shell model used to approximate variations in the electron density of the Pro-SNA conjugate.

Nominal Prot. Conc. (μM)	Fitted Prot. Conc (μM)	Linker Length (nm)	DNA Length (nm)

1	**1.3 ± 0.2**	**3.9 ± 0.5**	**5.0 ± 0.6**
4	**5.2 ± 0.5**	**4.0 ± 0.4**	**5.1 ± 0.5**

Table 3.1: Structural Characteristics of the Pro-SNA conjugate obtained by fitting the extracted non-resonant intensity profile to a spherical core-shell model.

To determine the structure of the counterion cloud surrounding the Pro-SNA conjugate, we employed classical-DFT to compute Rb$^+$ density profiles. Excess Rb$^+$ density profiles ($n_{Rb+}(r, \theta, \phi) - n_b$) were calculated by independently varying the linker (L) and DNA (D) lengths in increments of 0.5 nm. These profiles were angular averaged for comparison with the ASAXS data. For details, see Appendix A1, Sec. A1.7.

The DFT-derived and the ASAXS-extracted cross-term profiles show very good agreement for L = 4 nm and D = 5 nm as illustrated in Figs. 3.5B and 3.5C for the cases of 1 and 4 μM Pro-SNA concentrations (Appendix A1, Sec. A1.7 for goodness of fit). It should be noted that no multiplicative scaling factors were utilized to match the DFT calculated and the ASAXS-derived profiles. Fig. 3.5A shows the corresponding Rb$^+$ radial distribution profile. For comparison, Fig. 3.5A also shows a simplified geometric model for the excess Rb$^+$ density profile that results when each unit of negative charge on the DNA backbone is compensated by exactly one Rb$^+$ counterion and when a uniform distribution of Rb$^+$ neutralizes the charges in the linker region. In comparison to the geometric model, the DFT-derived distribution profile presents smoother variations. This is intuitively expected because sharp gradients would lead to unphysical osmotic pressure build-up.

It must be mentioned here that throughout the analysis we have (i) modeled the Pro-SNA as a sphere and (ii) assumed only radial distance (*r*)-dependence for the Rb^+ density. The radius of gyration of Cg Catalase calculated about orthogonal x, y and z axes defined with respect to its Protein Data Bank structure is 2.8 nm, 3.2 nm and 2.7 nm respectively. In addition, its asphericity is only 0.056, indicating that although Cg Catalase is slightly prolate, it is nearly spherical. Finally, the linker chains are large and flexible. We hypothesize that these chains will move to minimize their surface energy with the solvent, further reducing the asphericity of the excluded volume around the protein. Finally, the inherent 3D orientational averaging in solution-SAXS coupled with the low resolution of our SAXS data further smears out any small anisotropies. This validates the approximations that the protein core is spherical and that the Rb$^+$ distribution only depends on the radial distance from the protein core.

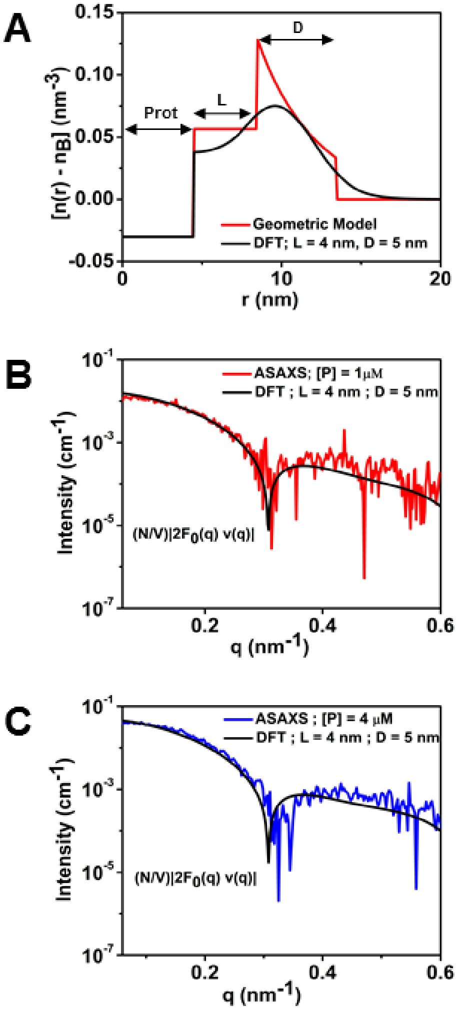

Figure 3.5: (A) DFT-derived model of the excess Rb$^+$ density [n(r) – n_b] as a function of radial distance from the center of the protein core for L = 4 nm and D = 5 nm (black). Also depicted is a simplified geometric model (red) for the excess Rb$^+$ distribution profile. (B and C) Direct comparison of the DFT-derived to ASAXS-extracted 2 $|F_0 (q)\ n(q)|$ profile for 1 µM (B) and 4 µM Pro-SNA (C).

Overall, the combined solution X-ray scattering-DFT analysis reveals certain key features regarding the Rb^+ ion distribution profile and the structural features of Pro-SNA:

(i) Within the shell, Rb^+ counterions compensate ~ 90% of the total negative charge on the DNA and linker segments: Integration of the DFT-derived Rb^+ charge density profile (Fig. 3.5A) up to $r = R_{prot} + L + D$ *gives* the total number of Rb^+ ions located within the DNA corona. The ratio of this number to the total charge on the linkers and DNA is the compensated charge fraction f_c = 90% (±3 %) for the two data sets. This is equivalent to our earlier study for monovalent cations surrounding an Au-SNA [32] where the denser core gold nanoparticle required the use of heavy-ion replacement SAXS, rather than ASAXS.

(ii) The highest Rb^+ ion concentration within the DNA shell is ~ 0.175 M and the effective "Debye length" for the conjugate is ~ 1.3 nm: For both 1 µM and 4 µM protein concentrations, the best fit DFT model predicts a maximum Rb^+ concentration of ~ 0.175 M. This represents a 3.5-fold enhancement over the bulk solution concentration of 0.05 M. Further, the excess Rb^+ density falls to 1/e of its value at the edge of the DNA shell at a distance of 1.3 nm beyond the shell. This ASAXS-DFT estimate for the Debye length (κ^{-1}) is comparable to the expected κ^{-1} = 1.34 nm for a monovalent electrolyte (here RbCl) at 50 mM concentration.

(iii) The lengths of the linker and ssDNA segments are $L = 4 \pm 0.5$ nm and $D = 5 \pm 0.6$ nm respectively. This D value implies an average rise/base of ~ 0.27nm for the ssDNA at 50 mM RbCl.

These results demonstrate the ability of the combined DFT-ASAXS approach to determine the local ion densities surrounding Pro-SNA conjugates. Specifically, once the Pro-SNA structural parameters are known (from SAXS), the ASAXS- DFT approach can predict the ionic distribution profile surrounding these bioconjugates. We use this to provide estimations of the ion distribution surrounding Pro-SNA over an extended salt concentration regime (10 – 300 mM) that encompasses

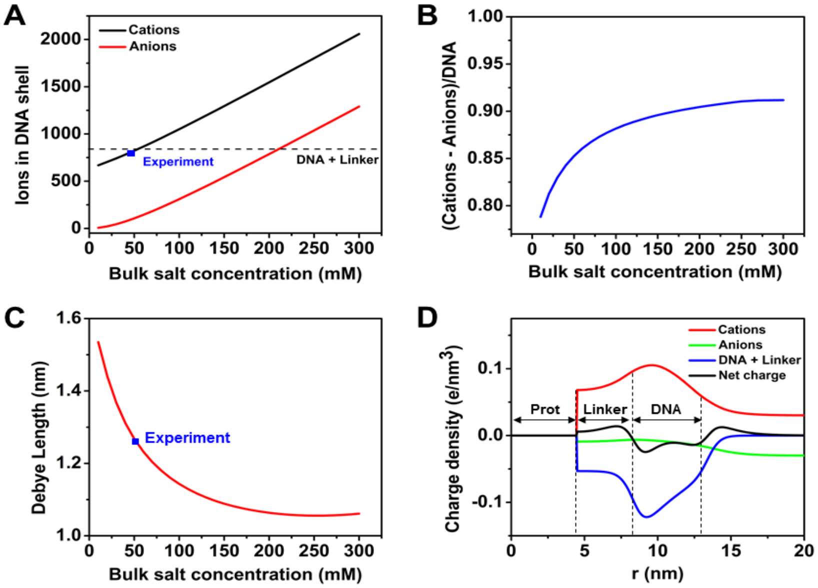

Figure 3.6: (A) DFT-derived predictions of the total number of Rb^+ cations (black) and Cl^- anions (red) within the DNA shell. The experimentally probed salt concentration (50 mM RbCl) is indicated by the blue marker and the total charge of the DNA and linker by the dashed line. (B) DFT calculated ratio of the effective number of cations within the shell (Cations –Anions) to the DNA + linker charge. (C) Effective Debye length as a function of bulk salt concentration (D) Charge density profiles due to the cations (red), anions (green), DNA + linker (blue) and the net charge (black) as a function of radial distance (r) from the center of the protein for [RbCl] = 50 mM.

the physiologically relevant (~ 150 mM) monovalent salt concentrations. The results of these calculations are summarized in Figure 3.6.

The total number of cations (Rb^+) and anions (Cl^-) within the DNA shell increases with increasing bulk salt concentration as shown in Fig 3.6A. At the experimentally probed salt concentration (50 mM RbCl), the Rb^+ cations are found to undercompensate (f_c ~ 90 %) the negative charge from the DNA and linker (Fig. 3.6A, dashed line). However, above ~ 75 mM, the number of cations within the DNA shell is predicted to exceed the negative charge from the DNA and linkers.

The ratio of the effective number of cations within the shell (Cations – Anions) to the DNA charge asymptotically approaches ~ 0.9 as the bulk salt concentration is increased to 300 mM as depicted in Fig. 3.6B. These results can be qualitatively justified by considering the competition between the concentration gradient dependent osmotic pressure and the charge mediated electrostatic forces. As the salt concentration increases, the number of anions brought into the shell increases due to the enhanced osmotic pressure. To maintain the near electro neutrality conditions in the DNA shell, the negatively charged DNA and linkers scavenge an increasing number of Rb^+ from the bulk solution. In particular, we emphasize that the DFT approach does not include ionic correlations, which decrease the free energy of the system, and can induce DNA charge overcompensation in some special cases (in the presence of multivalent cations, for example)[69]. The variation in the effective Debye length with bulk salt concentration agrees qualitatively with Debye-Huckel theory, as depicted in Fig. 3.6C.

For the experimentally probed 50 mM bulk RbCl case, Fig. 3.6D depicts the DFT-derived charge density profiles for the cations, anions, and DNA + linker, as well as the net charge. DFT calculations at all values of bulk salt concentration predict qualitatively similar variations in the net charge density profile of the Pro-SNA. In particular, the mobile Rb^+ ions occupy the regions between the protein surface and the start of the DNA and at the end of the DNA resulting in a net positive charge at the ends of the DNA segment (Fig. 3.6D, black line). The minima in the net charge density profile between ~ 7.5 nm and ~ 13.5 nm is due to the large negative charge of the DNA. Finally, the DFT calculations predict that not all the charge compensating Rb^+ ions are confined within the DNA shell, but instead utilize the space beyond the shell (as parameterized by the effective Debye length) to neutralize the DNA's negative charge. These calculations provide an estimate of the local potential energy variations that may be experienced by small molecules in their interaction with Pro-SNA conjugates.

Summary and Conclusions

We have performed the first study of the structure and counterionic cloud environment of a protein spherical nucleic acid conjugate. The combined use of ASAXS-DFT yields the radial distribution profile for the counterions, including a maximum in the enhancement of the counterionic density in the DNA shell that was 3.5X greater than the bulk solution concentration of 50 mM RbCl. Furthermore, the SAXS analysis with parameterized geometric models deciphered the structural attributes of the DNA corona (linker and DNA lengths) with 1 nm-resolution. Our ASAXS results also serve to validate DFT derived predictions of the ion distribution at the experimentally probed salt concentration. This enables the extension of DFT calculations to regimes encompassing physiologically relevant salt concentrations with greater fidelity. At physiological conditions (above 75 mM), the number of cations within the DNA shell is predicted to exceed the negative charge due to the DNA and linkers. The overcompensation by cations here is not due to ionic correlations but originates from the osmotic pressure differences between the bulk and the DNA shell, which induces a non-zero concentration of anions in the DNA shell that is compensated by cations.

This work demonstrates the sensitivity of ASAXS-DFT in deciphering the structure of the counterionic cloud surrounding Pro-SNAs and facilitates future investigations into the origins of their novel properties. For example, the influence of competing monovalent and divalent ion distributions on the enzymatic degradation of the DNA shell can be studied. High local concentrations of monovalent cations surrounding spherical nucleic acids contribute to the inhibition of the activity of certain nucleases, such as DNAse I and thus promote the intracellular stability of spherical nucleic acid conjugates[16]. The opposite is true for divalent cations. Further, the knowledge of the local charge environment around SNAs made possible using our approach should provide valuable insights into the interactions of these conjugates with small molecules and other solution bound species. Such studies will be directly relevant to the biodiagnostic and therapeutic efficacies of Pro-SNAs and other high DNA density nanoparticle conjugates. Furthermore, ASAXS measurements may be performed on Pro-SNA crystalline assemblies formed by Watson-Crick hybridization. The enhanced structural order, which manifests in diffraction peaks should extend the q-range and thereby, the spatial resolution for the Pro-SNA structure and the counterion distribution profile.

Proposed Future Work

1. Counterionic Distribution Profiles at physiological salt concentrations

In biological applications such as intracellular transfection, gene regulation, biodiagnostics and immunomodulation, the physiological environments encountered by SNAs including the intra and extracellular matrix typically contain approximately 150 mM monovalent Na/K ions in addition to sub-millimolar concentrations of divalent Ca and Mg ions. Under such conditions, the composition of the local counterionic cloud surrounding the SNA will have a strong influence on its stability against enzymatic degradation and its interactions with small molecule targets such as catalytic substrates and mRNA. Thus, it is vital to characterize the nature of the local ionic environment surrounding SNAs under physiologically relevant solution conditions.

The combined ASAXS-DFT approach presented in this study provides a powerful means of elucidating the identity and concentration of the counterions surrounding Pro-SNAs over a range of solution conditions. ASAXS measurements of the counter-ionic density distribution profile for Pro-SNAs dispersed in a buffer containing mono- and divalent ions at concentrations closely mimicking physiological solution conditions should be able to provide an estimation of the local concentration and identity of the dominant ionic species bound to the DNA shell. While DFT calculations enable the prediction of the number of ions in the DNA shell as a function of bulk solution concentration, experimental verification through ASAXS should prove invaluable in developing a comprehensive understanding of the electrostatic interactions of Pro-SNA in intracellular applications.

2. Counterion Distribution surrounding Pro-SNA superlattices

Nanoscale electrostatic, entropic and enthalpic forces profoundly mediate the assembly of SNAs into crystalline lattices. As a natural extension of our investigation into the ionic environment surrounding isolated Pro-SNA conjugates, we propose to study the structure of the ion cloud around these constructs when assembled into superlattices with distinct crystalline symmetries. Relatively little is currently known about the ionic environment surrounding superlattices composed of DNA functionalized nanoparticles from both an experimental and theoretical perspective and our research into the same will aide in filling an important knowledge gap.

In order to construct protein superlattices, Protein-ssDNA conjugates are first hybridized with complementary linker strands after which they are heated to a temperature above their melting point and slowly cooled down resulting in the formation of a thermodynamically stable Body Centered Cubic (BCC) type single crystal.[21] These lattices have been probed via small angle x-ray scattering to reveal diffraction peaks corresponding to a BCC type crystal structure. The study of the ion distribution surrounding isolated Pro-SNA conjugates via Anomalous SAXS relies on the measurement of subtle changes in the particle form factor $F(q)$ in the vicinity of an x-ray absorption edge in limit of infinite dilution where the structure factor $S(q)$ is assumed to be 1. The small magnitude of these differences coupled with the weak scattering from the proteins renders the ion-dependent contributions experimentally challenging to extract. However, the introduction of a finite structure factor $S(q)$ which results when these proteins are assembled into a definite crystal lattice will amplify the subtle energy-dependent differences measured in an ASAXS experiment and will allow us to isolate the resonant contributions arising from the counterions with a greater resolution and lower degree of error. In addition, it will allow us to study how the distribution of counterions around individual protein-DNA conjugates is modified upon assembly into a superlattice and give us a deeper understanding of the electrostatic interactions at play within the nanoparticle superlattice architecture.

Chapter 4: The Enzymatic Degradation of Protein Spherical Nucleic Acids probed by In-Situ X-ray Scattering

Abstract

The successful realization of DNA based nanotechnologies for therapeutic applications hinges on developing a deeper understanding of their interactions with biological environments. One such nanomaterial, Protein Spherical Nucleic Acids (Pro-SNA), are comprised of a protein core densely modified with a shell of covalently bound DNA. They have shown exceptional promise as intracellular protein transfection agents for the delivery of functional enzymes into cells due to the high density of DNA presented on their surface. However, the physiological stability of Pro-SNAs is threatened by nucleases, such as DNase I, which can catalyze the degradation of the DNA shell on Pro-SNAs. Herein, we elucidate the nanoscale structural transformations and the enzymatic reaction pathway inherent to the DNase I mediated degradation of Pro-SNAs using a label-free in-situ solution X-ray scattering approach. Time course Small Angle X-ray Scattering (SAXS) measurements confirmed by gel electrophoresis reveal the presence of a two-state system and a reaction pathway characterized by a slow, rate determining DNase I-Pro-SNA association step followed by a rapid DNA hydrolysis step. In addition, structural modelling of measured SAXS intensity profiles show that the DNA segments on a Pro-SNA are completely digested upon incubation with DNase. Finally, we demonstrate the use of Molecular Dynamics to predict the local ion density profiles surrounding the Pro-SNA which should be instructive in forecasting their stability in therapeutic applications. The in-situ, label free approach detailed here provides key

mechanistic and quantitative structural insights not accessible by conventional methods and should prove invaluable in probing enzyme catalyzed reactions on the nanoscale.

Introduction

Protein Spherical Nucleic Acids (Pro-SNAs) are an emergent class of biomaterials composed of a functional protein core and a dense shell of covalently bound oligonucleotides.[21] Watson-Crick hybridization between complementary DNA on neighboring proteins can be used to controllably program their assembly into crystalline lattices.[21] In addition, selective functionalization of residues on the surface of the protein core can be used to modulate the assembly of Au nanoparticles into different lattice types.[37] The dense and highly oriented shell of DNA on the protein surface enables their efficient transfection into cells. In particular, they have been shown to have a 280-fold enhanced cellular uptake in comparison to native proteins while retaining enzymatic functionality making them attractive intracellular protein transfection agents.[36] However, nature has developed an arsenal of enzymes called nucleases which can identify and attack foreign DNA[70] such as those found on Pro-SNAs. Nuclease catalyzed degradation of the DNA shell on Pro-SNAs threatens the serum stability and efficacy of these constructs in biological applications. Deoxyribonuclease I (DNase I) is an endonuclease widely distributed in mammalian[71] and human tissues[72-73] that is commonly used to test the resistance of DNA functionalized nanoparticles to enzymatic degradation[16, 74-78]. DNase I is a glycoprotein with an average molecular mass of 30 kDa. It catalyzes the direct nucleophilic attack of the phosphorus atom on the DNA backbone by a water hydroxyl resulting in the cleavage of the P-O3' bond and the formation of 5' phosphate terminated nucleotides.[79] While DNase I is not reported to have any marked sequence specificity, it is known to preferentially cleave phosphodiester linkages adjacent to pyrimidine bases.[80] Divalent Ca^{2+} and Mg^{2+} cations stabilize the conformation of DNase and facilitate the hydrolytic cleavage of the phosphodiester bond.[79, 81-82] Subsequently, the activity of DNase I is significantly reduced in buffers devoid of Ca^{2+} and Mg^{2+} or those containing monovalent ions.[83-85] While the activity of DNase I on free DNA has been extensively studied, little is known about the action of DNase I on DNA densely functionalized onto a particle core. Previous work has shown that the local chemical environment created by such dense DNA arrangements can have a profound effect on the interactions between nucleases and their DNA substrate. For instance, for the case of siRNA – Au nanoparticle SNAs, the site of nuclease catalyzed hydrolysis differs from that for free siRNA.[86] In addition, DNA functionalized onto AuNP cores were found to have a half-life that was 4.3 X longer than free DNA of the same sequence.[16] The high local Na^+ ion density and stearic hinderance created by the dense DNA shell were hypothesized to contribute to their enhanced stability. This suggests the need to independently study nuclease degradation reactions for the DNA-nanoparticle system of interest to best tailor strategies to enhance their serum stability. Previous studies on the DNase I mediated degradation of DNA on AuNPs have measured the increase in the fluorescence intensity of a fluorescent label on the DNA upon its degradation and subsequent liberation from the quenching AuNP core.[16-17] While such fluorescence-based assays can provide valuable insight into kinetic reaction parameters, they do not allow for a determination of the structural changes occurring within the DNA shell. They also do not provide insight into the reaction pathway. Further, they require the addition of fluorophore groups to the

DNA which may fundamentally alter the interactions between the nuclease and DNA. Small angle X-ray scattering (SAXS) offers an in-situ label-free method to probe the enzymatic degradation of the DNA shell on Pro-SNAs. The small wavelength (~ 1 Å) and high penetrating power of high energy X-rays make SAXS particularly well suited for the in-situ characterization of materials on the nanoscale (1-100 nm). Consequently, SAXS is a widely used tool for the structural characterization of nanomaterials[23, 87] and biological macromolecules including proteins and DNA[30, 88-89]. Pro-SNAs are an ideal candidate for a SAXS measurement due their highly monodispersed protein cores. In addition, the relatively low electron density of the protein core in comparison to the DNA shell allows for a direct measurement of the length of the DNA shell as previously shown.[90] In comparison, direct measurement of the DNA shell is not feasible for AuNP-DNA conjugates because scattering from the electron dense AuNP core dominates the SAXS profile.[32] SAXS should therefore be a sensitive probe of changes in the DNA shell during the course of its enzymatic degradation. SAXS profiles measured at intermediate reaction time points should also be able to provide a snapshot of the state of the system and enable a deeper understanding of the reaction mechanism.

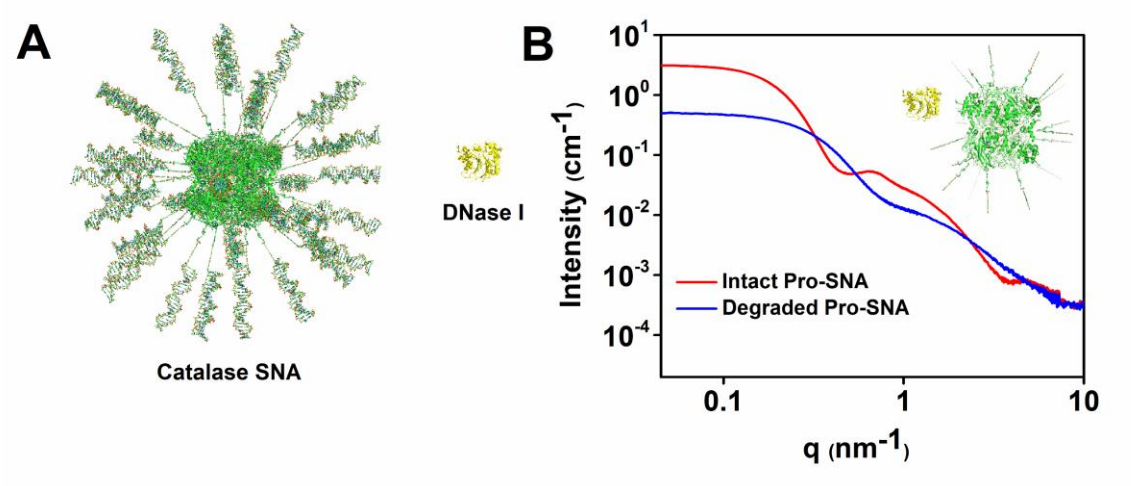

Figure 4.1: (A) Schematic Illustration of Catalase Protein SNA depicting a *Cg* Catalase core covalently bound with dsDNA. Also shown is the nuclease, DNase I, drawn to scale. (B) Background subtracted SAXS intensity profiles from Pro-SNA before (red) and after (blue) incubation with DNase I, revealing a decrease in the forward scattered intensity, I (q=0), and a shift in the position of the first minima consistent with the degradation of the DNA shell on the Pro-SNA.

The Pro-SNA employed in this study is composed of a Corynebacterium Glutamicum Catalase core densely functionalized with approximately 40 double-stranded DNA which are 20 base-pairs in length (Fig. 4.1(A)). The DNA is covalently attached to the protein core using previously established methods.[21] Briefly, the surface accessible amines on the protein are converted into azides and then reacted with a cyclooctyne (DBCO) terminated oligonucleotide. Complementary duplexer DNA strands are then added in excess to hybridize the single stranded DNA on the protein surface (For details, see *Materials and Methods*). The Pro-SNAs are then dispersed to a final concentration varying between 0.5 μM – 4 μM in a reaction buffer for DNase I which contains 10 mM Tris HCl, 0.5 mM $CaCl_2$ and 2.5 mM $MgCl_2$ and has a pH of 7.6 at 25°C. DNase I is then added to a final concentration of 43-100 nM and the reaction is allowed to proceed at room temperature for 1- 6 hours. The reaction mixture is sampled at intermediate time points to track changes in the SAXS profile of the Pro-SNA as described below. To the best of our knowledge, this study represents the first demonstration of SAXS to track an enzyme catalyzed reaction in-situ.

Materials and Methods

1. Synthesis of Pro-SNAs

All the DNA used for this study was synthesized on an ABI 392/394 automated DNA synthesizer on solid controlled pore glass (CPG) supports. Two DNA sequences were employed: a dibenzocyclooctyne (DBCO) terminated strand that was covalently attached to the protein core (sequence: 5' DBCO dT – $(Sp18)_2$ GTTCCTCGACCTTCCGACCC - 3' where Sp18 refers to a hexaethylene glycol spacer) and a complementary strand used to duplex the DBCO modified DNA on the protein (sequence: 5'- GGGTCGGAAGGTCGAGGAAC- 3'). All the phosphoramidites and reagents used for the DNA synthesis were purchased from Glen Research. Catalase from Corynebacterium Glutamicum (Sigma Aldrich, Product number: 02071) was modified with DNA using previously described methods.[21] Briefly, Catalase was exchanged into a bicarbonate buffer (100 mM $NaHCO_3$, 0.5 NaCl, pH 9.0) using Millipore Amicon Ultra centrifugal filter units following which the surface accessible amines on the protein were converted into azides by reacting the protein with a ~ 3000-fold excess of tetraethylene glycol linkers containing an *N*-hydroxy-succinimide (NHS) ester and an azide group on opposing termini (Thermo Scientific, catalog number : 26130). The reaction between the linkers and protein was allowed to proceed for 2 hours at 25°C while shaking at 1000 rpm on a Benchmark Multitherm shaker. The azide-labelled proteins were then purified by five rounds of ultracentrifugation. The number of azide labels per protein was determined through MALDI mass spectrometry (Bruker Autoflex) by comparing the molecular weight of a native Catalase protein to that of an azide-modified protein and using the fact that each azide labels adds 274 Da to the weight of the protein. The concentration of the protein was determined using UV-Vis spectroscopy and the known molar extinction coefficient of the protein at 405 nm (ε_{405} = 324,000 M^{-1} cm^{-1})[21]. The azide labelled proteins were then exchanged into PBS (0.5 M NaCl) by ultracentrifugation and functionalized with DBCO terminated DNA using a cycloaddition reaction (Cu free "click chemistry") between the azide groups on the surface of the protein and the DBCO moieties on the 5' termini of the DNA. Typical reactions contained 1 μM protein and 300 μM DNA and were allowed to proceed for 3 days at 25°C while shaking at 1000 rpm on a Benchmark Multitherm shaker. The unreacted DNA was removed by 10 rounds of ultracentrifugation. The number of DNA strands per protein was quantified by UV-Vis spectroscopy using the known molar extinction coefficients of the protein and DNA (ε_{260} = 170,500 M^{-1} cm^{-1}). To hybridize the single stranded DNA on the protein, complementary DNA of the indicated sequence were added to the DNA functionalized proteins at a 100-fold excess relative to the protein concentration. The DNA modified proteins were then purified and exchanged into DNase I reaction buffer (10 mM Tris-HCl, 2.5 mM $MgCl_2$, 0.5 mM $CaCl_2$, pH 7.6) to a final concentration of 0.5 – 4 μM. The DNase I used for the enzymatic degradation reactions was obtained from New England BioLabs (Catalog No. M0303S).

2. X-ray Scattering Measurements

The Small Angle X-ray Scattering (SAXS) measurements were conducted at Sector 5 ID-D of the Advanced Photon Source at Argonne National Lab. The incident X-ray energy used was 15 keV and the average incident flux was ~ 10^{11} photons/sec. The spot size of the incident beam at the sample was 0.25 x 0.25 mm^2. All the measurements were performed on samples held in a 1.5 mm diameter quartz capillary housed in an in-vacuum flow cell to minimize air scattering. In addition, the entire beam path was also placed under vacuum. Three CCD detectors were placed along the beam path to allow for a simultaneous collection of SAXS/MAXS/WAXS data over a q range of 0.022 – 1.35 nm^{-1} with the SAXS detector (Rayonix) placed 7.5 m from the sample stage. The flux of the incident and transmitted beams were monitored using an ion chamber placed before the flow cell and a cadmium tungstate scintillating crystal followed by a pin diode embedded in the beam stop respectively. These intensities were then used to normalize the SAXS intensities collected on the Rayonix SAXS area detector. In order to prevent radiation damage, the samples were continuously flowed through the capillary during the measurements at a flow rate of 4 µl/s. To improve statistics, 5 frames were collected per sample with an exposure time of 3s/frame. All the measurements were performed at room temperature using the same capillary tube. The capillary was washed thoroughly with pure water and Sodium Hydroxide between measurements. SAXS profiles of the empty capillary, pure water and the reaction buffer were collected before and after each measurement to ensure that the background level was unaffected by particle aggregation or sticking to the capillary walls. The 2D SAXS patterns were converted into 1-D intensity profiles through azimuthal integration while taking into account the solid angle, flat-field, transmission and polarization corrections. The patterns were also normalized according to exposure time. SAXS profiles from the empty capillary and the capillary with buffer and water (Exposure time: 10 s;5

frames) were used for background subtraction and to convert the data to an absolute scale using established procedures.[65] For absolute intensity calibration, the normalized and corrected intensity profiles from pure water (difference between scattering profiles from capillary with pure water and empty capillary) were fitted to straight lines. The intercept of these best fit lines was set to 0.0165 cm^{-1} which is the absolute intensity (scattering cross section/volume) for water at 25°C. The sample data was then scaled accordingly. The time course SAXS measurements were performed as follows. The DNase I was added to a sample of the Pro-SNA dispersed in the reaction buffer contained in a 1.5 mL Eppendorf tube and then mixed by pipetting. The tube was loaded into the sample stage and an 80 μL aliquot of the Pro-SNA-DNase I reaction mixture was pulled up into the capillary tube and measured 5 minutes after the addition of the DNase I resulting in the measured SAXS profile at the first time point (Figure 4.2A). The capillary was then washed following which another aliquot was pulled up from the reaction mixture and measured at the second time point. This process was repeated for all the reaction time points measured.

3. Gel Electrophoresis Measurements (SDS PAGE)

For the Sodium dodecyl sulfate Polyacrylamide Gel Electrophoresis (SDS PAGE) measurements, 43 nM DNase I was added to 1 μM Pro-SNA dispersed in the reaction buffer. Thirty minutes after the addition of DNase I, 20 μL of the reaction mixture was diluted with 20 μL of Laemmli sample buffer (2x, Sigma Aldrich) and Dithiothreitol (DTT) was added to a final concentration of 100 mM in 50 μL. The sample was then placed in a PCR tube and heated at 85°C for 10 minutes. The DTT, SDS and the application of heat denatures the proteins and linearizes them. Samples of the native

Catalase protein, pure Pro-SNA and pure DNase I were prepared in the same manner. These samples were then run on a pre-cast 4-15 % protein gel (Bio-Rad, product number: 4561084) with Tris-Glycine-SDS running buffer (Sigma Aldrich). A Precision Plus Protein Standard (Bio-Rad, product number: 1610373) was loaded into the second lane of the gel while the native Catalase, pure Pro-SNA, Pro-SNA-DNase I reaction mixture and pure DNase I were loaded into the third, fourth, fifth, sixth and seventh lanes of the gel respectively. The gel was then installed into the gel apparatus (Bio-Rad Mini-PROTEAN Tetra Cell) with a buffer dam and run at 200 V for 30 minutes. The gel was then washed and stained using SimplyBlue SafeStain (Thermo Fisher) and imaged on a FluorChem Q imaging system (Alpha Innotech) using Transwhite excitation and EBr emission. The focus and exposure were adjusted, and an image of the gel was acquired.

Results and Discussion

To test the feasibility of SAXS to monitor the enzymatic degradation of the DNA shell, Pro-SNA (4 μM) were incubated with DNase I (166.6 nM) at room temperature for 6 hours following which a SAXS measurement was made on the Pro-SNA-DNase I system. The SAXS intensity profiles measured from the Pro-SNA-DNase I system are dominated by scattering from the Pro-SNA. At the concentration of DNase employed, the scattering from the DNase does not result in any measurable features in the SAXS intensity profile (See Appendix A2, Sec. A2.1). Background subtracted SAXS intensity profiles of the Pro-SNA measured before and after incubation with DNase I (Fig. 4.1(B)) show dramatic differences in shape and demonstrate that SAXS is sensitive to structural changes in the DNA shell upon digestion by DNase I. The solvent subtracted SAXS intensity measured from a system of dilute, non-interacting particles is:

$$\Delta I(q) = \frac{N}{V}\, \Delta\rho^2 V_p^2\, |F(q)|^2 \tag{4.1}$$

where $q = 4\pi\ \sin\theta/\lambda$ is the modulus of the scattering vector, 2θ is the scattering angle, and λ is the wavelength of the incident X-rays. Here $\frac{N}{V}$ represents the particle concentration, $\Delta\rho = \rho_p - \rho_s$ is the contrast between the electron density of the particle $\left(\rho_p\right)$ and that of the solvent $(\rho_s), V_p$ is the volume of the particle and $F(q)$ is the single particle form factor given by:

$$F(q) = \frac{1}{V_p} \int_{V_p} e^{iqr}\, dV_p \tag{4.2}$$

At q = 0, $|F(q)|^2$ = 1, and Eq. 4.1 reduces to $\Delta I(q = 0) = \frac{N}{V}\, \Delta\rho^2 V_p^2$. Thus, the forward scattered intensity, $\Delta I(q = 0)$, is proportional to the squared number of electrons in the particle. Thus, the decrease in the forward scattered intensity from the Pro-SNA upon incubation with DNase I is indicative of a reduction in the number of electrons in the DNA shell. In addition, the position of the first minima in the SAXS profile shifts to a higher value of q indicating a decrease in the length of the DNA shell surrounding the protein. These changes are not observed when the native protein is incubated with DNase I under identical conditions (Appendix A2, Sec. A2.2). This demonstrates that the changes observed in the SAXS intensity profile measured from the Pro-SNA-DNase I system are due to the degradation of the DNA shell by DNase I.

In order to elucidate the enzymatic degradation pathway characteristic to the Pro-SNA-DNase I system, a time course SAXS measurement was performed. Aliquots of the reaction mixture were sampled and measured at several time points after the addition of DNase I (166.6 nM) to the Pro-SNA (4 μM). The corresponding SAXS profiles (Fig. 4.2(A)) exhibit a decrease in the forward scattered intensity (I(q=0)) with time indicating a loss of electrons from the DNA shell due to DNase catalyzed degradation. The scattering profiles also exhibit three clear isosbestic points at $q = 0.32\ nm^{-1}$, $q = 0.54\ nm^{-1}$ and $q = 2.2\ nm^{-1}$ where the measured intensity from the Pro-SNA-DNase I system is invariant during the course of the reaction. Isosbestic points are indicative of reactions in which there exists a linear relationship between the concentrations of components. Such reactions generally consist of two components wherein there is a stochiometric conversion of reactant to product without the formation of any detectable intermediates. Isosbestic points have been widely reported in UV-Vis[91-93], X-ray scattering[94-95] and X-ray reflectivity[96] studies of two component systems.

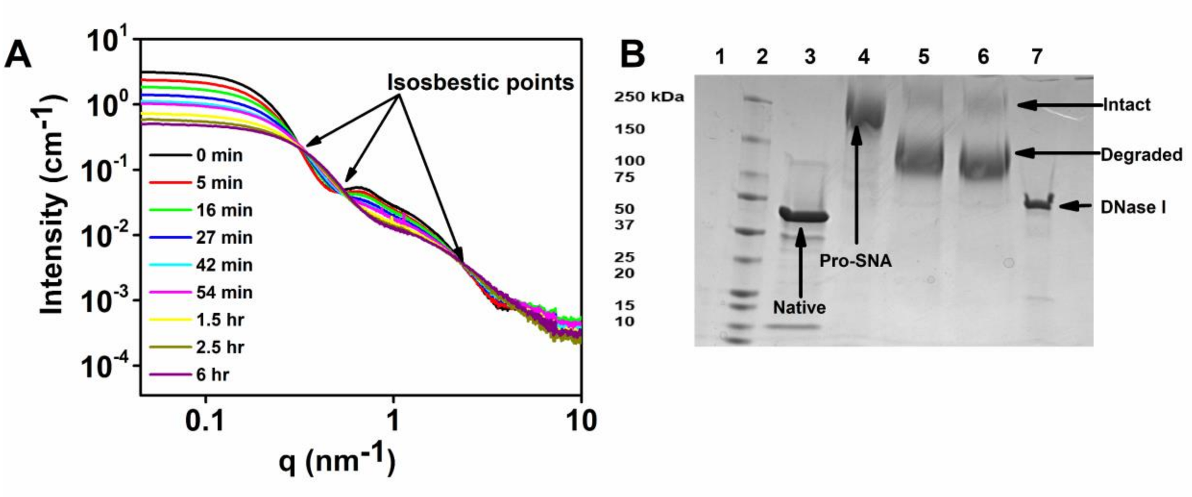

Figure 4.2: (A) Background subtracted SAXS intensity profiles from the Pro-SNA-DNase I system as a function of time from the start of the reaction. The presence of isosbestic points suggests a two-state system. (B) SDS PAGE gel containing a reference protein ladder (Lane 2), native Catalase (Lane 3), Pro-SNA (Lane 4), DNase (Lane 7) and the Pro-SNA- DNase I reaction mixture sampled at the 30-minute (Lane 5) and 45 minute time point (Lane 6). The resolution of the Pro-SNA-DNase I into two distinct bands confirms the presence of two Pro-SNA states.

For the case of the Pro-SNA-DNase I system, we hypothesize that upon association with the intact Pro-SNA, the DNase I catalyzes a rapid hydrolysis of the DNA shell without the formation of any intermediates. Thus, the Pro-SNA effectively exists in two states: intact (State A) and degraded (State B). To validate our “two-state” model, we used gel electrophoresis to probe the reaction at intermediate time points. SDS Polyacrylamide gel electrophoresis (PAGE) can be used to resolve a mixture of proteins with varying molecular radii based on their differential electrophoretic mobility through a gel matrix upon the application of an electric field. The experimental workflow consisted of incubating 1μM Pro-SNA with DNase I at a concentration of 43 nM. At two intermediate reaction time points (30 min and 45 min), an aliquot of the reaction mixture was diluted with Laemmli sample buffer containing Sodium Dodecyl Sulphate (SDS) and 100mM Dithiothreitol (DTT) following which it was heated at 85° C for 10 minutes. The addition of SDS and DTT followed by heat treatment linearizes the Pro-SNAs and ensures that their rate of migration through the gel is proportional to their average molecular radii. A similar SDS PAGE protocol was used for reference samples of native Catalase, pure Pro-SNA and pure DNase I (See Materials and Methods). The native protein, pure Pro-SNA, pure DNase I and the two aliquots of the reaction mixture containing the Pro-SNA and DNase I were loaded onto a 4-15 % PAGE gel and run for 30 minutes at 200 V. The resultant gel was imaged and is depicted in Fig. 4.2(B). Using a reference protein ladder (Lane 2), the native (Lane 3) protein was determined to have a mass consistent with the known molecular weight of the Catalase monomer (60 kDa). The Pro-SNA monomer (Lane 4) has a mass of approximately 240 kDa which is consistent with the DNA loading density on the protein determined via UV-Vis spectroscopy using the known extinction coefficient of DNA at 260 nm (See Materials and Methods). The reaction mixture sampled at the 30-minute time point (Lane 5) resolves into 2 distinct bands on the gel. The first band corresponds to intact Pro-SNA, the second lower band is the degraded Pro-SNA while a third fainter band corresponds to the DNase I. The identification of the third band as DNase I is facilitated by a comparison with Lane 7 which was loaded with pure DNase I. The reaction mixture sampled at the 45-minute timepoint (Lane 6) also resolves into two distinct bands whose positions are identical to the bands seen in the 30-minute reaction timepoint sample. This indicates that the second band corresponds to Pro-SNAs in their final degraded state. The separation of Pro-SNAs into two populations – Intact (State A) and Degraded (State B) on an SDS PAGE gel provides secondary experimental validation of the proposed two-state model.

The extent to which DNase I degrades the DNA shell on a Pro-SNA can be determined by fitting the measured SAXS intensity profiles from the intact (State A) and degraded (State B) Pro-SNA to appropriate structural models. The Catalase protein core was modelled as an ellipsoid with semi-axes given by a = b = 5.05 nm; c = 3.5 nm and an average electron density of 0.404 e/nm^3. These values were fixed based on the crystallographically determined atomic coordinates of Catalase recorded in its Protein Data Bank (PDB ID: 4B7F) entry. The double stranded DNA and linker strand are modelled as cylinders with radii of 1 nm and 0.5 nm respectively. Forty such cylinders are placed on the surface of the ellipsoid such that the electrostatic potential energy of the configuration is minimized. The lengths and electron densities of the DNA and linker are used as fitting parameters. This ellipsoidal model was used to simulate the SAXS intensity profiles from the bare protein and Pro-SNA in State A and State B (Fig. 4.3). The equivalent ellipsoid used to model Catalase and the points of linker and DNA attachment on the surface of the ellipsoid are shown in Fig. 4.3(A) while Fig. 4.3(B) shows the best fit of the ellipsoid model to the SAXS intensity profile from bare Catalase. The ellipsoid-cylinder model for the Pro-SNA is seen to accurately reproduce the features of the scattering profile from the intact Pro-SNA in State A (Fig. 4.3(C)). In order to model State B, the cylinders corresponding to the DNA were removed and only those for the linker groups were left on the surface of the ellipsoid. Additionally, short cylinders representative of dinucleotides were added to solution to model the DNA fragments produced as a result of the digestion of the DNA shell by DNase I. The addition of dinucleotides was motivated by MALDI mass spectrometry analysis of the degraded DNA segments produced at the end of the reaction which revealed the presence of dinucleotides as the predominant product (Appendix A2, Sec A2.7.). This strategy produced a good fit to the scattering profile from the Pro-SNA in State B

(Fig. 4.3(D)), suggesting that all the DNA on the Pro-SNA are digested by DNase I at the end of the reaction. These results are further corroborated by a model-independent Pair Distance Distribution Function analysis of the SAXS data (Appendix A2, Sec. A2.3). PDDF analysis reveals that the native Catalase protein core has a maximum intermolecular distance, D_{max} of 12.8 nm while that of the DNA functionalized protein is 27.7 nm. Upon enzymatic degradation, D_{max} for the Pro-SNA reduces to 16.7 nm indicating that the DNA shell has reduced in length from 7.4 nm to 1.9 nm. This is consistent with a complete degradation of the DNA component of the shell by DNase I leaving the linkers attached to the protein core.

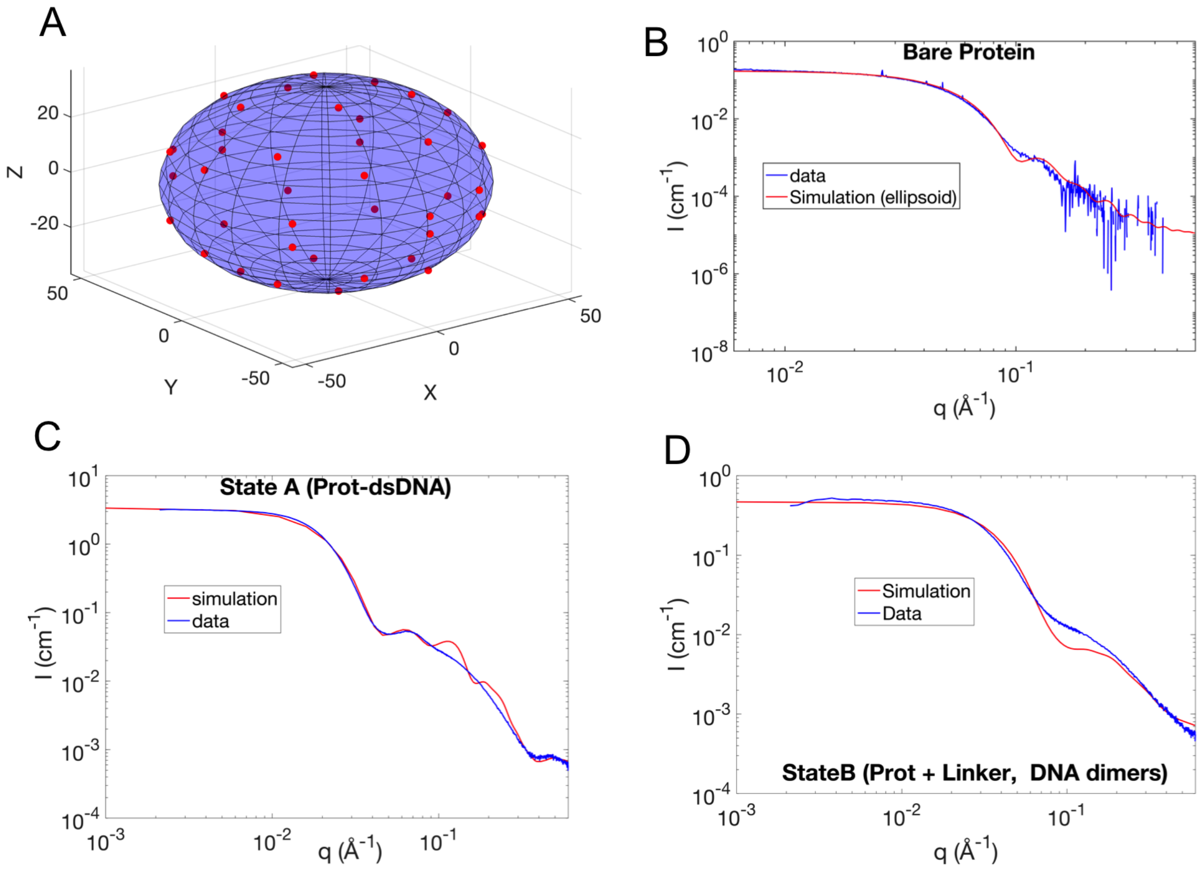

Figure 4.3: (A) Representation of an ellipsoid used to model the protein core of a Pro-SNA showing the points of DNA attachment (red). (B) Background subtracted SAXS intensity profile of bare protein fitted to ellipsoid model (C) & (D) SAXS Intensity profiles of Pro-SNA in State A and State B with their best fit curves generated using the ellipsoid-cylinder model described in the text.

The two-state model also suggests a reaction pathway for the DNase catalyzed hydrolysis of the DNA shell on Pro-SNAs consisting of a slow, rate determining enzyme association step proceeded by a rapid degradation of the DNA shell by DNase I. In this scheme (Fig. 4.4(A)), the DNase I is hypothesized to cause the complete hydrolysis of the DNA shell on a given Pro-SNA before proceeding to catalyze the degradation of the DNA on another Pro-SNA conjugate. A possible explanation for this effect is that the high density of DNA on the surface of protein effectively templates the enzymatic degradation reaction. Thus, in comparison to migrating between Pro-SNA conjugates, it is more favorable for the enzyme (DNase I) to remain associated to a single Pro-SNA due to the abundance of its substrate (DNA) on the surface of the protein core. It should be mentioned here that the reaction pathway described above is facilitated by the low concentration of Pro-SNA in solution. At higher Pro-SNA concentrations, the reaction pathway may differ due to the increased likelihood that the DNase may jump from one Pro-SNA to another resulting in partially degraded DNA shells at intermediate reaction time points. However, this reaction pathway should be relevant to biological applications wherein the concentration of SNAs typically used is relatively low (< 1 nM).[12, 97-98]

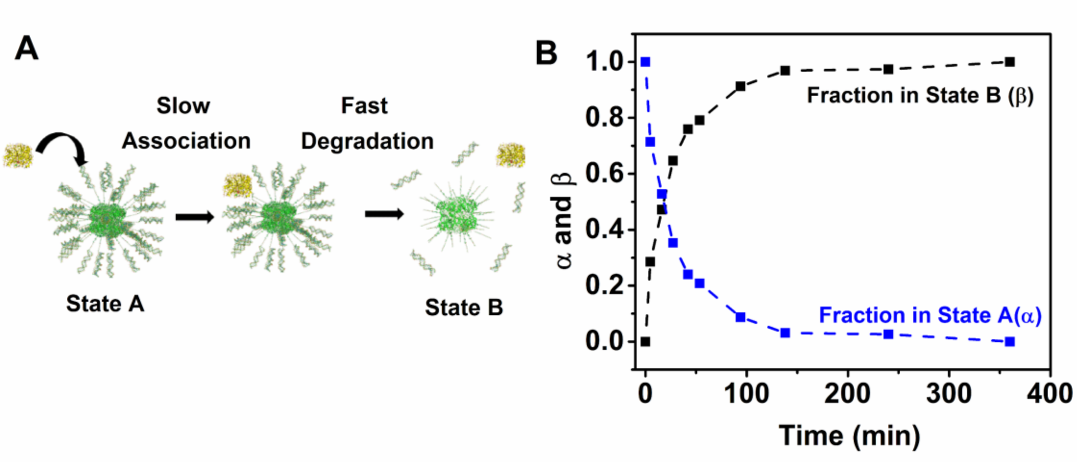

Figure 4.4: (A) Schematic of proposed reaction pathway consisting of a slow, rate determining enzyme-substrate association step and a fast substrate (DNA) degradation step resulting in either intact Pro-SNAs (State A) or degraded Pro-SNAs (State B). (B) Time evolution of fraction of Pro-SNAs in State A, α (blue) and State B, β (black) obtained by fitting intermediate SAXS intensity profiles with a linear combination of intensity profiles representative of State A and B, respectively.

Another implication of the two-state model is that the SAXS intensity profile I(q) measured from an aliquot of the reaction mixture sampled at any intermediate time point can be represented as a linear combination of the SAXS intensity profiles from the Pro-SNAs in State A and State B:

$$\Delta I(q) = \alpha I_A(q) + \beta I_B(q) \qquad [\alpha + \beta = 1] \qquad (4.3)$$

Here α and β represent the fraction of Pro-SNAs in State A and State B respectively such that the total number of Pro-SNAs in the system remains conserved. $I_A(q)$ is the measured intensity profile from a Pro-SNA conjugate before the addition of DNase I (0 min timepoint) and $I_B(q)$ is the measured intensity profile from the Pro-SNA-DNase I system at the end of the reaction (6 hour timepoint). The measured intensity at any intermediate timepoint can be fitted to Eq. 4.3 above resulting in a determination of α and β. Such a fitting process was carried out for all the measured SAXS intensity profiles depicted in Fig. 4.2(A) (Appendix A2, Sec. A2.4). This enabled a determination of the relative fractions of intact and degraded Pro-SNAs as the degradation reaction proceeded in time. As the reaction progresses, the fraction of Pro-SNAs in State A exhibits an exponential decay which is consistent with the observed decrease in the forward scattered intensity, $\Delta I(q = 0)$, from the Pro-SNA (Fig. 4.4(B)).

In order to elucidate the kinetic parameters governing the reaction pathway depicted in Fig. 4.4 (A), we consider the Michaelis-Menten model for enzyme-substrate kinetics[99]:

$$. \qquad E + S \underset{k_{-1}}{\overset{k_1}{\rightleftarrows}} X \xrightarrow{k_2} P + E \qquad (4.4)$$

Here, E and S refer to the enzyme (DNase I) and substrate (DNA) while X and P refer to the complex and products, respectively. The DNase I is assumed to associate with the Pro-SNA resulting in the formation of an enzyme-substrate complex with a rate constant given by k_1. The rate constant for the backward reaction is given by k_{-1} while the rate constant governing the formation of products from the enzyme-substrate complex is given by k_2. The initial rate of the reaction, v_0, defined as the amount of product produced per unit time at the start of the reaction can be expressed as a function of [E] and [S] through the Michaelis-Menten relation:

$$v_0 = \frac{V_m S}{S + K_m} \qquad (4.5)$$

Here V_m and K_m are the maximal velocity of the reaction and the Michaelis constant respectively and are given by:

$$V_m = k_2[E] \tag{4.6}$$

$$K_m = \frac{k_{-1} + k_2}{k_1} \tag{4.7}$$

According to the two-state model previously described, the association of DNase I to its DNA substrate is proceeded by the rapid degradation of the DNA shell. Thus, the rate of the backward reaction (k_{-1}) can be considered to be negligible. Putting $k_{-1} \approx 0$ in Eq. 4.7 enables us to extract the rate constants k_1 and k_2 through an examination of the initial rate of the reaction v_0 as a function of DNA concentration [S] at a fixed DNase I concentration [E]. Accordingly, SAXS was used to track the rate of progression of the enzymatic degradation reaction at varying concentrations of the

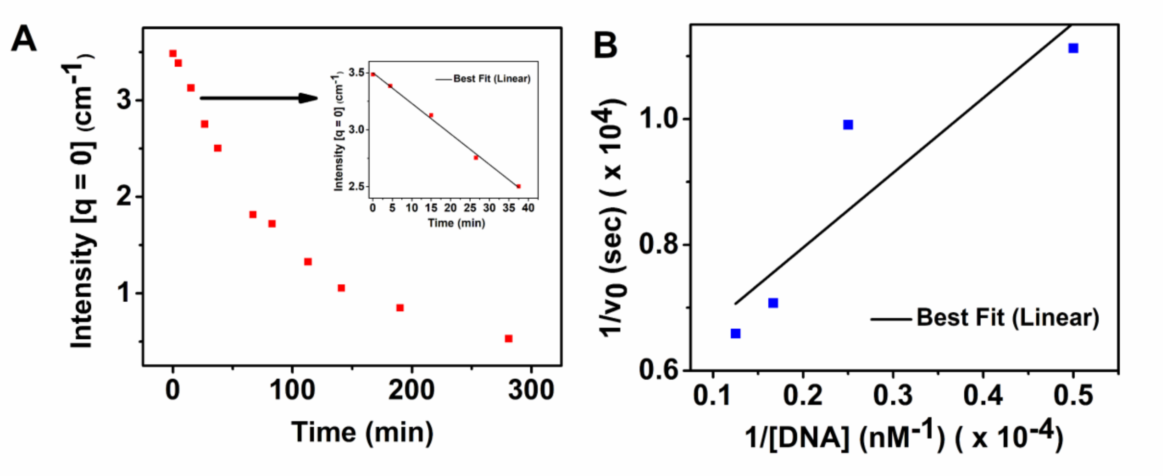

Figure 4.5: (A) Forward scattered Intensity I (q = 0) as a function of reaction time for the case of 2 µM Pro-SNA incubated with 43 nM DNase I. (Inset) I (q = 0) for the first five reaction time points were fitted with a straight line whose slope is proportional to the initial reaction rate, v_0. (B) Lineweaver-Burk plot of $1/v_0$ vs. 1/[DNA]. The slope and intercept of the best fit line were used to determine the rate constants k_1 and k_2.

Pro-SNA, and hence, the DNA substrate in solution. The concentration of the Pro-SNA in solution was varied from 0.5 – 2 µM corresponding to DNA concentrations ranging between 20 – 80 µM while the concentration of DNase I was held constant at 43 nM. For each concentration probed, SAXS measurements were made on aliquots of the reaction mixture sampled over the course of 1-2 hours (See Appendix A2, Sec. A2.5).

By definition, the initial rate of the reaction is equal to the tangent to the reaction progress curve. The progression of the degradation reaction considered here can be quantified through the measured decrease in the forward scattered intensity $I(q = 0)$ with time during the reaction (Fig. 4.5(A)). Using Eq. 4.3 at q = 0, the rate of decrease in the fraction of Pro-SNAs in State A, and hence the initial rate of the reaction, v_0, is found to be proportional to the rate of decrease in the forward scattered intensity, $I(q = 0)$:

$$v_0 = -\frac{d\alpha}{dt} = -\frac{dI(q=0)}{dt}\frac{1}{[I_A(q=0) - I_B(q=0)]} \tag{4.8}$$

Here, $I_A(q = 0)$ and $I_B(q = 0)$ represent the forward scattered SAXS intensities measured from the Pro-SNAs in State A and State B respectively. The decrease in the forward scattered intensity, $I(q = 0)$, measured from a reaction mixture containing 2 µM Pro-SNA is shown in Fig. 4.5 (A). The quantity $\frac{dI(q=0)}{dt}$ in Eq. 4.8 above is determined from the slope of the best fit line to $I(q = 0)$ measured at initial reaction time points. This allows for a determination of v_0 for each of the substrate concentrations probed. A plot of $1/v_0$ vs. $1/S$ (Fig. 4.5 (B)), referred to as a Lineweaver-Burk plot, can then be used to extract the rate constants k_1 and k_2 using Eq. 4.5 – 4.7. Using this process, the values of k_1 and k_2 for the enzymatic degradation reaction described by Eq. 4.4 were found to be 1.9 X 10^{-10} s^{-1} nM^{-1} and 4.2 X 10^{-6} s^{-1} nM^{-1} respectively. The finding that k_2 is 4 orders of magnitude higher than k_1 is consistent with our proposed model consisting of a slow association step proceeded by a fast degradation step.

Our use of in-situ SAXS in conjunction with SDS PAGE has revealed the following key insights into the DNase I mediated enzymatic degradation of Pro-SNAs:

(i) The enzymatic degradation of the DNA shell on a Pro-SNA follows a two-state model: In-situ SAXS presents a label-free method to track the progression of the DNase I catalyzed degradation of DNA functionalized onto a nanoparticle core. Isosbestic points observed in time course SAXS measurements of the Pro-SNA – DNase I system reveal that at any point during reaction the Pro-SNAs are either completely intact (State A) or degraded (State B). This model was further validated by SDS PAGE measurements which confirmed the existence of two distinct populations of Pro-SNAs.

(ii) The reaction pathway is characterized by a slow, rate determining DNase I-Pro-SNA association step and a fast DNA degradation step: The two-state model suggests a reaction pathway in which DNase I associates to a given Pro-SNA in a slow, rate determining step after which it catalyzes the complete hydrolysis of the DNA shell before acting upon a subsequent Pro-SNA. The dense DNA architecture on a Pro-SNA acts to preferentially template the enzymatic degradation reaction on the surface of the protein. This is consistent with previous studies which have reported a higher enzyme-substrate association constant for DNase I for the case of DNA functionalized onto the surface of a Au nanoparticle in comparison to free DNA.[16] It should be noted here that the reaction pathway described above is valid at low concentrations of Pro-SNA.

(iii) In-Situ SAXS reveals nanoscale structural changes to the DNA shell upon degradation by DNase I: Analysis of the SAXS Intensity profiles measured from the Pro-SNA before and after incubation with DNase I using both Pair Density Distribution Functions (PDDF) and appropriate structural models reveal that the DNA segments of the Pro-SNA shell are completely digested by the enzyme when it encounters a Pro-SNA.

These results demonstrate the power of in-situ SAXS to elucidate both the reaction pathway and the nanoscale structural changes to the DNA shell associated with the DNase I mediated enzymatic degradation of a Pro-SNA. The reaction rate and extent of structural modification to the DNA shell may be influenced by the effect of the reaction environment on the enzymatic activity of DNase I. The local counterionic environment associated with the highly negatively charged DNA shell on the Pro-SNA is of particular interest as it is expected to have a significant impact on the activity of DNase I. The buffer chosen for our system contains Tris-HCl in addition to the optimal quantities of Ca^{2+} and Mg^{2+} required to maintain the structural integrity and activity of DNase I. However, the composition of the local ionic environment associated with the DNA shell may differ from that of the bulk depending on the counterion neutralizing the negative charge of the DNA. In order to determine whether monovalent $Tris^{+}$ or divalent Ca^{2+}/Mg^{2+} is the dominant counterionic species in the DNA shell, we simulated our experimental conditions using Molecular Dynamics. The model system used for the Molecular Dynamics simulation employed an ellipsoidal protein core [a = b = 5.05 nm, c = 3.5 nm]. The linker and DNA strands were modelled with a coarse-grained bead model. The system also included $MgCl_2$ (3mM) and NaCl (7.52 mM) to represent the effective divalent and monovalent counterions in the buffer. Figure 4.6 shows density maps representing the concentrations of monovalent Na^+ (Fig. 4.6(A)) and divalent Mg^{2+} (Fig. 4.6(B)) counterions surrounding the protein projected onto the x-z plane. Due to the symmetry of the protein with respect to the x and y coordinates (a = b = 5.05 nm), an averaged snapshot of the x-z plane is representative of the positions of the ionic species surrounding the Pro-SNA. Also shown are ionic concentration profiles as a function of distance from the surface of the protein (R) taken along the dotted lines in Fig. 4.6 (A) – (B). MD simulations predict that the maximal concentrations of Na^+ and Mg^{2+} within the DNA shell are approximately 130 mM and 180 mM respectively. Further, of the negative charge compensated within the DNA shell, approximately 49 % and 51 % are compensated by Na^+ and Mg^{2+} ionic species. It should be noted here that the negative charge due to the DNA is not completely neutralized by cations within the DNA shell. The cations instead utilize the region beyond the DNA shell to completely compensate the negative charge due to Pro-SNA. Our MD results indicate that despite a higher concentration of monovalent ions in the bulk, the counterion cloud surrounding a Pro-SNA contains roughly equivalent quantities of mono- and di-valent ions. Further, simulations performed with a fewer number of DNA beads (shorter DNA) show that as the length of the DNA chain is reduced, the fraction of divalent counterions in the DNA shell increases. This suggests that stearic hinderance due to longer DNA chains prevents a greater number of divalent ions from entering the DNA shell for the case of proteins with 20 base-pair long DNA chains. Further, the predominance of divalent counterions in the DNA shell on a Pro-SNA should support the enzymatic function of DNase I. Such theoretical predictions of local ion density profiles surrounding DNA functionalized nanoparticles may be experimentally verified using Anomalous Small Angle X-ray Scattering

(ASAXS) as previously demonstrated.[90] The use of such an approach should be particularly instructive in mixed ion systems. For instance, the biological environments relevant to the therapeutic applications of Pro-SNAs typically contain roughly 150 mM monovalent salt and less than 1mM divalent salt. Understanding the influence of such solution salt conditions on the enzymatic degradation of DNA on a Pro-SNA should aid studies aimed at enhancing the stability of Pro-SNA formulations.

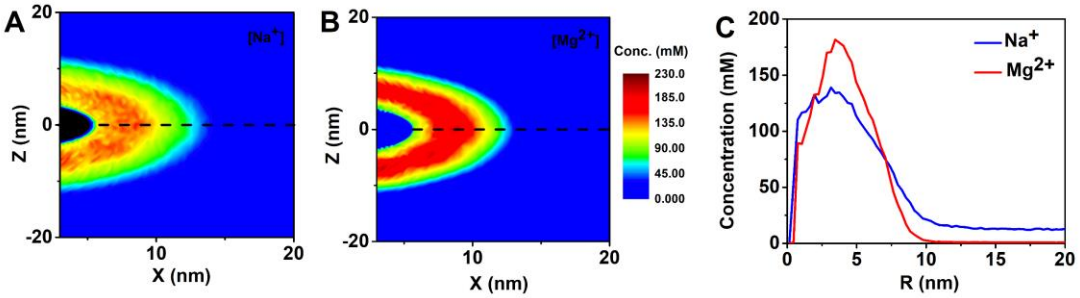

Figure 4.6: (A) Concentration heat maps for Na^+ and (B) Mg^{2+} counterions surrounding the Pro-SNA projected onto the x-z plane showing a slightly higher Mg^{2+} concentration within the DNA shell. (C) Concentration profiles of Na^+ (blue) and Mg^{2+} (red) as a function of distance R from the surface of the surface of the protein taken along the dashed lines shown in (A) and (B).

Conclusions

In conclusion, we have demonstrated the use of a label-free, solution X-ray scattering technique to quantitatively track the enzymatic degradation of the DNA shell on a Protein Spherical Nucleic Acid construct. Our in-situ measurements of the DNase I mediated degradation of the DNA on a Pro-SNA provides insights into nanoscale structural transformations inaccessible by typical fluorescence-based nuclease assays. In particular, structural modelling of measured SAXS intensity profiles from the Pro-SNA-DNase I system before and after incubation with DNase reveal that the DNA shell on a Pro-SNA is completely digested by DNase I resulting in the formation of predominantly dinucleotide DNA fragments.

In addition, time course SAXS measurements reveal a two-state reaction pathway for the enzymatic degradation of the DNA shell on Pro-SNAs. While the association of DNase I to its DNA shell substrate proceeds slowly, the high density of DNA presented on the protein surface templates a rapid DNase catalyzed hydrolysis of the DNA. This leads to the existence of Pro-SNA in one of two measurable states: Intact (State A) or degraded (State B). The observed reaction pathway should be relevant to intracellular applications wherein the concentration of Pro-SNAs employed is also relatively low. These findings should inform efforts towards enhancing the physiological stability of Pro-SNAs for therapeutic and intracellular transfection applications.

Proposed Future Work

Effect of Salt Concentration and DNA type on the enzymatic activity of DNase I

DNase I is a non-specific endonuclease whose activity is strongly influenced by solution conditions such as bulk mono- and divalent salt concentrations, temperature and pH. In addition, the type of DNA substrate is also known to influence the activity of DNase I – with the specific activity of DNase I reported to be 500-fold lower for single stranded DNA in comparison to double stranded DNA. A systematic investigation of the effect of these parameters on the rate of enzymatic degradation of the DNA shell on a SNA should allow us to identify parameter regimes which stabilize DNA-nanoparticle conjugates against enzymatic degradation. Towards this end, we propose studying the rate of DNase mediated enzymatic degradation of a Pro-SNA as a function of bulk monovalent salt concentration and DNA type.

The action of DNase is critically dependent on the presence of Ca^{2+} and Mg^{2+} ions. Molecular Dynamics and crystallographic data strongly suggest the presence of four distinct ion binding sites on DNase I – two of them occupied by Ca^{2+} and the other two by Mg^{2+}. Ca^{2+} is believed to stabilize the structure of DNase, while Mg^{2+} in conjunction with Ca^{2+} facilitate the electrostatic fit between the catalytically active site on DNase and its DNA substrate. Subsequently, the activity of DNase I is significantly reduced in buffers devoid of Ca^{2+}/Mg^{2+} or in those containing monovalent ions. For example, the activity of DNase is reported to drop two-fold when the concentration of monovalent salt (NaCl/KCl) in the buffer is increased from 0 to 30 mM. To test the effect of bulk monovalent salt concentration on the rate of enzymatic degradation of the DNA shell on a Pro-SNA, we performed time-course SAXS measurements on the Pro-SNA - DNase I system incubated in buffers containing 30mM and 300 mM NaCl. The results of these measurements are depicted in Fig. 4.7. Upon increasing the NaCl concentration in the reaction buffer from 30 mM to 300 mM, the SAXS profiles measured from the Pro-SNA-DNase I system over 1 hour do not exhibit any significant changes (Fig. 4.7(B)). In particular, the forward scattered intensity does not decrease with time and isosbestic points are not observed as is the case when the concentration of NaCl in solution is 30 mM (Fig. 4.7(A)). These preliminary results suggest that the activity of DNase towards Pro-SNAs is sensitive to the composition of the reaction buffer.

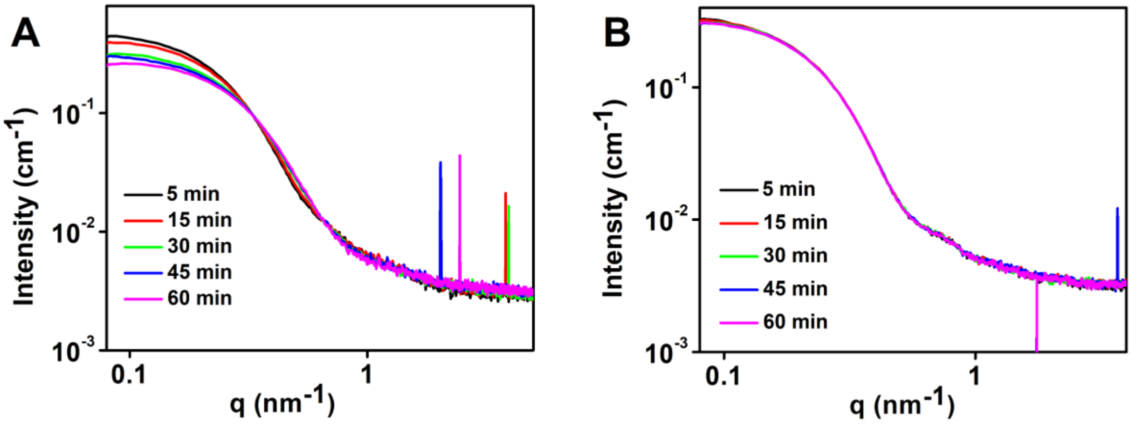

Figure 4.7: Solvent subtracted time course SAXS profiles of Pro-SNA-DNase I system in the presence of 30 mM NaCl (A) and 300 mM NaCl (B). Increasing the monovalent salt concentration in the buffer has the effect of reducing the rate of enzymatic degradation of the Pro-SNA as evidenced by the reduced rate of decrease in the forward scattered intensity.

Future studies of this salt dependency would focus on systematically investigating the rate of this reaction as a function of increasing salt concentration.

In addition, the activity of DNase is also influenced by the type of DNA substrate. DNase can hydrolyze single stranded DNA, but it does so with a reduced efficiency. Thus, studies aimed at elucidating the influence of DNA type (ssDNA vs. dsDNA) on the rate of enzymatic degradation of SNAs should inform future SNA design considerations for biological applications.

Chapter 5: The Competition Between Mono- and Divalent Counterions surrounding Protein Spherical Nucleic Acids

Abstract

Protein spherical nucleic acid conjugates (Pro-SNA) consist of a functional protein core and a dense shell of covalently bound DNA, which enables their cellular uptake and assembly into ordered crystalline lattices. However, in cellular applications, the oligonucleotide shell on Pro-SNAs is susceptible to degradation by nucleases such as Deoxyribonuclease I (DNase I). The activity of DNase I is inhibited by monovalent cations (Na^+) and enhanced in the presence of divalent cations (Mg^{2+} /Ca^{2+}). In a Pro-SNA, the high negative charge due to the DNA results in the formation of a dense counterionic cloud, the ionic composition of which could either inhibit or enhance the activity of DNase I present in the surrounding solution effectively altering stability of the Pro-SNA against enzymatic degradation. Thus, it is important to characterize the competing distributions of mono and divalent cations in the counterion cloud at varying relative concentrations of these ions in the bulk solvent. This will enable a nanoscopic understanding of the role played by the local ionic environment in stabilizing Pro-SNAs against enzymatic degradation, and in identifying conditions that maximize the efficacy of Pro-SNAs. In this study, we use to Anomalous Small Angle X-ray Scattering to simultaneously probe the distributions of monovalent Rb^+ and divalent Sr^{2+} surrounding Pro-SNA. Our approach provides quantitative insights into the local concentrations and relative spatial distributions of Rb^+ and Sr^{2+} counterions

surrounding Pro-SNAs as a function of varying bulk RbCl and $SrCl_2$ concentration and should prove instructive in predicting the stability of Pro-SNAs and other highly charged macromolecular complexes in biological applications.

Introduction

The biological milieu characteristic to human and animal systems contains a complex mixture of small molecules, macromolecules and ions.[100-101] Several vital physiological processes are governed by the identities and relative solution concentrations of ionic species.[102-104] For instance, ion channels and ion pumps exploit electrochemical gradients established by differential concentrations of mono and divalent ions to selectively facilitate the transport of ionic species across otherwise impermeable membranes.[105-106] Thus, it is clear that the function of entities entering the biological milieu should be strongly influenced by their interactions with the varying identities and concentrations of ionic species present therein.[107-108]

As nanoparticle-based therapeutics are increasingly gaining popularity, there is a need to fundamentally understand their interactions with ions in the intra and extra cellular matrix. One such formulation, the Spherical Nucleic Acid[5] (SNA) composed of a nanoparticle core and a dense oligonucleotide shell has shown great promise in gene regulation[17, 97], immunomodulation[12] and intracellular transfection.[56, 98] The DNA architecture on particle surface is stabilized due to the presence of dense a counterion cloud that serves to neutralize the high negative charge on the DNA.[16] All the interactions of these SNAs with the cell membrane and moieties in the intra and extra cellular matrix take place against the backdrop of the diffuse counterionic cloud bound to the oligonucleotide shell. As a result, the characteristics of the cloud are expected to influence the outcome of such interactions. The composition of the ionic cloud surrounding an SNA has a profound effect on an important serum interaction – that with nucleases capable of catalyzing the hydrolysis of the DNA shell on an SNA[16-17]. Several such nucleases, such as the widespread endonuclease Deoxyribonuclease I (DNase I), are salt-sensitive and realize their optimal efficiency only in the presence of divalent cations such as Ca^{2+} and Mg^{2+}.[73, 79-81, 84] For instance, DNase I is reported to possess 4 ion-specific binding sites – 2 each for Ca^{2+} and Mg^{2+}.[81, 109] Divalent Ca^{2+} ions have been shown to play a central role in the catalytic mechanism of DNase I and effectively facilitate the electrostatic fit between the active site on the enzyme and negatively charged DNA phosphate backbone substrate.[79] Magnesium ions (Mg^{2+}) on the other hand stabilize the functional conformation of DNase I.[109] Environments devoid of these cations or those containing high concentrations of monovalent ions cause a reduction in the enzymatic efficiency of DNase I. The identity of the counterionic species present in the cloud surrounding an SNA should therefore influence its stability against degradation by nucleases such as DNase I. Previous studies have suggested that enhanced concentrations of monovalent Na^{+} ions closely associated to the DNA shell on a Au nanoparticle SNA displace the divalent Ca^{2+} and Mg^{2+} ions bound to DNase I effectively inhibiting the degradation of the DNA shell.[16] While these studies enabled a fundamental understanding of the origin of the enhanced stability of SNAs against enzymatic degradation, they do not address the question of how the composition of the counterion cloud influences the stability of an SNA. The relative concentrations of ionic species (Ca^{2+}, Mg^{2+}, Na^{+}, K^{+}) in biological systems often exhibit drastic local variations, particularly across the cellular membrane.[110] For instance, the concentration of divalent Ca^{2+} is 10,000-fold greater outside the cell than inside while that of Na^+ is ~ 10-fold higher in the extracellular matrix. Accordingly, the composition of the local counterionic cloud surrounding an SNA and thus its stability against nuclease mediated enzymatic degradation is also expected to vary as the construct travels from the exterior to the interior of the cell. Thus, in such mixed ion systems, it is important to understand the competition between mono and divalent ions in neutralizing the charge on an SNA.

Herein, we address this challenge in the context of a Protein Spherical Nucleic Acid (Pro-SNA). Pro-SNAs are composed of a functional enzyme core and a dense, highly tailorable oligonucleotide shell and have demonstrated applications in programmable assembly[21, 37] and intracellular transfection.[36] They are particularly well suited for intracellular protein transfection and delivery applications due to the dual functionalities imparted by their oriented DNA shell which enables efficient cellular uptake and their functional protein core which can effect catalytic processes within cells. Like traditional Au nanoparticle SNAs, their physiological stability is threatened by the presence of nucleases, such as DNase, thus highlighting the need to develop strategies to combat their degradation in serum. The first step towards this goal is developing a complete understanding of the composition of the local counterionic cloud surrounding a Pro-SNA as a function of varying bulk mono and divalent salt concentrations. Elucidating the salt concentration regimes wherein divalent ions (such as Ca^{2+} and Mg^{2+}) outcompete monovalent ions (such as Na^+ and K^+) as the charge compensating counterions for the DNA on a Pro-SNA should enable a prediction of their stability as they are internalized by cells and effectively move between different biological environments. The competition between ionic species in solution is governed by a complex interplay between electrostatic, entropic and osmotic forces.[52, 111] While simple entropic considerations favor the replacement of two monovalent cations with one divalent cation for the compensation of a single unit of negative charge[112], factors such as osmotic pressure, ion size and the stearic hinderance created by the confined geometry of the Spherical Nucleic Acid architecture may produce counterintuitive effects. Thus, in addition to aiding efforts aimed at improving the physiological stability of Pro-SNA constructs, our research should deliver insight into the fundamental physical factors driving charge compensation in complex high density macromolecular systems.

Small Angle X-ray Scattering has proven to be an invaluable tool in probing the nanoscale structure and solution interactions of Pro-SNAs. Specifically, we have demonstrated the applicability of SAXS as an in-situ label free probe of the enzymatic degradation of Pro-SNAs by DNase I. Time course SAXS measurements revealed quantitative nanoscale structural changes to the Pro-SNA upon enzymatic degradation and enabled a determination of the reaction pathway. In addition, contrast variation SAXS techniques, such as Heavy Ion Replacement SAXS (HIRSAXS) and Anomalous SAXS (ASAXS), have been used to determine the counterionic distribution profile surrounding SNA constructs.[32, 90] ASAXS, in particular, stands out due to its ability to provide a nanometer scale element-specific map of the ionic species surrounding highly charged biomacromolecules and their complexes.[58] It has been extensively used to characterize the structure of the diffuse counterionic cloud surrounding DNA[60-61, 113], RNA[114] and polymer brushes.[43] Additionally we have previously demonstrated its utility in resolving the structure of the counterionic cloud surrounding Pro-SNA. ASAXS exploits the variation in the scattering strength of an element in the vicinity of an X-ray absorption edge to map out its spatial distribution. In particular, at energies close to an elements core electron binding energy, the atomic form factor of the element takes on an energy dependent complex form given by[42]:

$$f(E) = f_0 + f'(E) + if''(E) \qquad (5.1)$$

Here, f_0 is equivalent to the atomic number of the element, Z. $f'(E)$ and $f''(E)$ are the referred to as the resonant real and imaginary parts of the dispersion correction. Close to an elemental absorption edge, $f'(E)$ typically takes on negative values thus reducing the effective number of scattering electrons and subsequently the scattering strength of the element of interest. This in turn results in modulations in the measured scattered intensity from the macromolecule-counterion system which may be used to isolate the scattering contributions from the counterion cloud as previously demonstrated. In this work, in order to simultaneously probe the distribution of mono and divalent counterions surrounding a Pro-SNA using ASAXS, we use Rb^+ as the monovalent counterion and Sr^{2+} as the divalent counterion. The K - absorption edge energies of Rb^+(15.2 keV) and Sr^{2+}(16.1 keV) are easily accessible at synchrotron X-ray sources and are high enough to overcome the attenuation due to the aqueous phase. While the mono and divalent ions present in cellular environments are Na^+, K^+, Mg^{2+} and Ca^{2+}, their absorption edge energies are too low to overcome the attenuation due to the aqueous solvent. The replacement of divalent Ca^{2+}/ Mg^{2+} ions by Sr^{2+} and monovalent Na^+/ K^+ by Rb^+ is supported by the tested hypothesis that distribution of counterions surrounding a charged object depends only on ion valency and not ion size. [32]

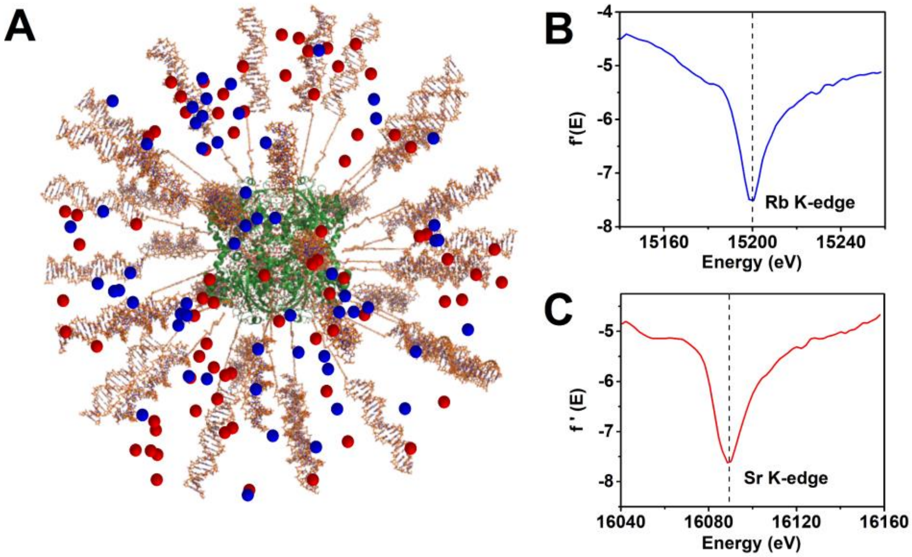

Figure 5.1: (A) Schematic representation of Pro-SNA comprised of Cg Catalase core and 20 bp long double stranded DNA along with charge neutralizing Rb^+ (blue) and Sr^{2+} (red) counterions. (B) Measured dispersion corrections $f'(E)$ as a function of incident x-ray energy near the Rb^+ K-edge (15. 2 keV) and (C) the Sr^{2+} K-edge (16.1 keV).

The Pro-SNA employed in this study is composed of a Cg Catalase protein core covalently functionalized with a shell of double stranded DNA which are 20 base-pairs in length (Fig. 5.1(A)).The chemical modification of Catalase with DNA is realized by a two part strategy[21] (described in detail in Materials and Methods) which relies on the conversion of the surface accessible amine functional groups on Catalase into azides through the attachment of tetraethylene glycol linkers containing a terminal Azide group followed by functionalization using a cycloaddition reaction (copper-free "click chemistry") between DBCO modified synthetic single stranded DNA and the azide groups on the labelled proteins. The DBCO DNA on the protein are then hybridized to a complementary DNA strand. This strategy results in a DNA loading density of approximately 40 DNA strands per protein. The Pro-SNA are then dispersed to a final concentration of 2 μM in a buffer containing varying concentrations of $SrCl_2$ and RbCl salts which act as the source of Sr^{2+} and Rb^+ counterions respectively. Four sets of samples were prepared with Pro-SNA suspended in buffers containing: (A) 50 mM RbCl, (B) 45 mM RbCl + 5 mM $SrCl_2$, (C) 40 mM RbCl + 10 mM $SrCl_2$ and (D) 30 mM RbCl + 20 mM $SrCl_2$. We then use ASAXS at the absorption edges of Rb^+ and Sr^{2+} to discern the scattering contributions from the monovalent Rb^+ and divalent Sr^{2+} ionic populations surrounding the Pro-SNA. Upon varying the bulk solution concentration of $SrCl_2$ from 0 to 20 mM, while maintaining a total bulk salt concentration of 50 mM (RbCl + $SrCl_2$), we find that the number of Rb^+ ions localized in the DNA shell decreases while the number of Sr^{2+} correspondingly increases. This change is accompanied by a decrease in the radial extension of both the Rb^+ counterionic cloud and the overall DNA shell. Interestingly, at a concentration of 20 mM $SrCl_2$ and 30 mM RbCl, we find that the Rb^+ ions within the DNA shell are not completely replaced by Sr^{2+}. A closer quantitative examination of these trends follows in the subsequent section.

Our ASAXS approach in conjunction with a judicious choice of particle core has enabled a simultaneous quantitative comparison of the local concentrations and spatial distributions of mono and divalent counterions surrounding Pro-SNA. In addition to providing a nanoscale structural characterization of mono and divalent ionic distribution profiles surrounding Pro-SNA, our study outlines a strategy to explore competitive ion binding events surrounding charged macromolecular complexes.

Materials and Methods

1. Sample Preparation

The DNA used for Pro-SNA studied in this work were synthesized on an ABI 392/394 automated DNA synthesizer using controlled pore glass (CPG) supports and reagents from Glen Research. Two DNA sequences were employed : the first (5' DBCO dT – $(Sp18)_2$ GTTCCTCGACCTTCCGACCC - 3') was anchored to a Catalase protein core using previously described methods[21] while a second complementary linker strand (5'-GGGTCGGAAGGTCGAGGAAC- 3') was used to duplex the DNA on the protein. Each Pro-SNA contains approximately 40 DNA strands. The DNA loading density was determined through UV-Vis absorption spectroscopy and the known molar extinction coefficients of the protein (ε_{405} = 324,000 M^{-1} cm^{-1}) and DNA (ε_{260} = 170,500 M^{-1} cm^{-1}). The Pro-SNA were then suspended to a final concentration of 2 μM in the buffers (A) – (D) described in the text.

2. X-ray Scattering Measurements

The X-ray Scattering measurements were performed at the Advanced Photon Source 5ID-D beamline. The incident x-ray beam size was 0.25 x 0.25 mm^2 and had an average flux of ~ 10^{11} photons/sec at 15 keV. An in-vacuum flow cell set up with a quartz capillary (1.5 mm diameter) was used to minimize air scatter. In order to prevent radiation damage, the sample was continuously flowed at a rate of 4 μl/s. SAXS data was collected using a Rayonix detector placed

7.5 m away from the sample stage. The collected SAXS intensities were normalized using the measured flux of the incident and transmitted beams. The Rb^+ and Sr^{2+} K-edges were calibrated using a XANES fluorescence scan from a 1 M solution of pure salt ($RbCl/SrCl_2$). At each incident ray energy, 5 frames were collected from each sample with an exposure time of 3 s/frame. The capillary was then thoroughly washed with pure water and Sodium Hydroxide following which SAXS profiles were collected from the empty capillary and water to ensure that the background level remained unchanged. SAXS profiles were also collected from pure buffers (A-D) to enable appropriate solvent subtraction. The 2D SAXS patterns were converted into 1-D intensity profiles through azimuthal integration. Solid angle, flat-field, transmission, exposure time and polarization corrections were also applied to the data. Finally, the SAXS profiles from the empty capillary and water were used to convert the data to an absolute scale using established procedures.[65]

Results and Discussion

In order to draw both qualitative and quantitative conclusions regarding trends in the number and spatial distribution profiles of monovalent Rb^+ and divalent Sr^{2+} ions in the counterion cloud surrounding Pro-SNAs as a function of bulk salt concentration, we performed ASAXS measurements on Pro-SNAs suspended in buffers containing: (A) 50 mM RbCl (B) 45 mM RbCl + 5 mM $SrCl_2$ (C) 40 mM RbCl + 10 mM $SrCl_2$ and (D) 30 mM RbCl + 20 mM $SrCl_2$. For simplicity, we describe the results and ASAXS analysis scheme for the case of Pro-SNA suspended in 50 mM RbCl here. A similar procedure was followed for Pro-SNAs dispersed in buffers (B) – (D).

The background subtracted SAXS intensity measured from a system of dilute, non-interacting particles and their counterions at x-ray photon energies below an absorption edge is given by:

$$\Delta I(q,E) = \frac{N}{V}[\,|F_0(q)|^2 + f'(E)\big(2F_0(q)v(q)\big)] \tag{5.2}$$

Here, q is the magnitude of the scattering vector and is given by $q = 4\pi \sin\theta/\lambda$, where 2θ is the scattering angle and λ is the wavelength of the incident x-rays. The first term of the above equation $|F_0(q)|^2$ is non-resonant and contains the form factor, $F_0(q)$, from a single Pro-SNA conjugate and its associated counterions. It represents the total scattering contribution from the nanoparticle-counterion system at energies far removed from an absorption edge (here, Rb K-edge: 15.2 keV, Fig. 5.1(B)). The second term is a resonant cross-term which additionally comprises the real part of the anomalous dispersion correction $f'(E)$ which is seen to exhibit a sharp decrease in magnitude in the vicinity of an absorption edge. The negative values taken on by $f'(E)$ close to the absorption edge (Fig. 5.1(B)) correspond to a reduction in the effective number of scattering electrons from Rb^+ [$f_0 + f'(E) = 36 + f'(E)$]. This decrease is expected to modulate the intensity, $I(q,E)$, measured close to an absorption edge. This term also contains $v(q)$, which is the Fourier transform of the excess counterion density profile surrounding the particle,$[n(r) - n_B]$, where n_B is the bulk number density of the ion. This term encodes the spatial distribution of the targeted ion (here, Rb^+) surrounding the particle. The pre-factor $\frac{N}{V}$ represents the concentration of the particles (here, Pro-SNA). The background subtracted SAXS intensity profiles measured from Pro-SNA suspended in 50 mM RbCl at four incident x-ray energies below the Rb K absorption edge (15.2 keV) are shown in Fig. 5.2(A). The four incident x-ray energies used and the corresponding values of $f'(E)$ at these energies are tabulated in Fig. 5.2(A). The magnitude of $f'(E)$ as a function of incident energy was determined with the help of an experimentally measured fluorescence scan and through the use of the Kramers-Kronig relations (Appendix A3, Sec A3.1). At low values of q, $F_0(q)$ and $v(q)$ are expected to be positive as a result of which $\Delta I(q,E)$ should decrease in

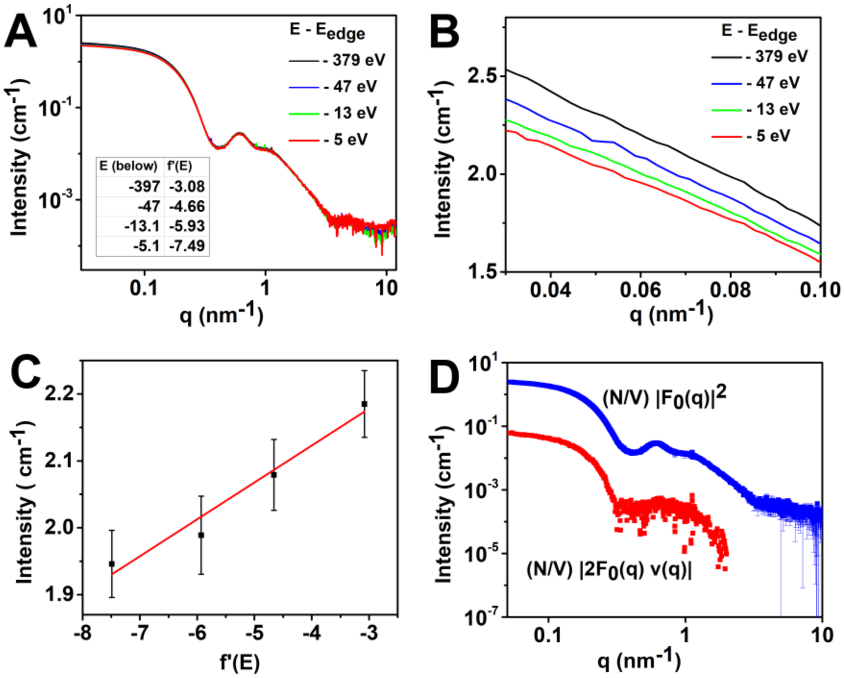

Figure 5.2: (A) Background subtracted SAXS intensity profiles measured from 2 µM Pro-SNA dispersed in 50 mM RbCl at four incident x-ray energies (Table, inset). (B) Magnified view of intensity profiles at low q showing a decrease in magnitude as incident energy approaches K-edge energy (15.2 keV). (C) Example of a linear fit to $\Delta I(q,E)$ vs. $f'(E)$ data at q = 0.06 nm^{-1}. (D) Extracted non-resonant (blue) and resonant (red) intensity profiles.

magnitude as the energy of the incident x-ray photon approaches that of the absorption edge. A magnified view of the scattered intensities at low q plotted on a linear scale (Fig. 5.2(B)) demonstrates the expected trend – as the energy of incident x-rays are varied from a value 397 eV below the edge $(f'(E) = -3.08)$ to one 5 eV below $(f'(E) = -7.49)$ the magnitude of the scattered intensity decreases by ~ 10.9%. This demonstrates that ASAXS is sensitive to the distribution of excess Rb^+ surrounding the Pro-SNA. In order to isolate the two partial intensity terms described in Eq. 5.2, a linear fit procedure was employed. Briefly, the measured $\Delta I(q, E)$ vs. $f'(E)$ data was fitted to a straight line, following which the terms $\frac{N}{V}\left(2F_0(q)v(q)\right)$ and $\frac{N}{V}[\,|F_0(q)|]^2$ were extracted as the slope and y-intercept of the best fit line. An example of such a fit at q = 0.6 nm^{-1} is shown in Fig. 5.2(C). This process was carried out for all the q-values in the measured range (q = 0.05 – 10 nm^{-1}) resulting in the extraction of the non-resonant profile,$\frac{N}{V}[\,|F_0(q)|^2]$, and the resonant cross term $\frac{N}{V}\left(2F_0(q)v(q)\right)$. The non-resonant intensity profile and the magnitude of the resonant intensity profile are shown in Fig. 5.2(D). The magnitude of the resonant intensity is only depicted upto 2 nm^{-1} due to the high degree of experimental uncertainty observed beyond this value. A visual inspection of these partial intensity profiles reveals certain key qualitative insights. The position of the first minima in the resonant intensity profile occurs at q = 0.31 nm^{-1} while that for the non-resonant intensity profile occurs at q = 0.40 nm^{-1} indicating that the Rb^+ counterion cloud extends beyond the DNA shell on the Pro-SNA. A similar result was reported for the case of Pro-SNA functionalized with single-stranded DNA dispersed in 50 mM RbCl.[90] The qualitative differences observed in the forms of the non-resonant and resonant intensity profiles (Fig. 5.2(D)) are due to the influence of $v(q)$ – the Fourier transform of the excess Rb^+ density distribution indicating that our ASAXS approach is uniquely sensitive to resonant scattering contributions from the Rb^+ counterion cloud. Further, the resonant intensity profile, $\frac{N}{V}\,\left(2F_0(q)v(q)\right)$, is observed to be 2 orders of magnitude lower than the non-resonant profile, $\frac{N}{V}\left[\,|F_0(q)|^2\right]$ highlighting the inherent challenge in using ASAXS to extract the resonant counterion-dependent scattering profile within reasonable experimental uncertainty. This procedure was repeated for SAXS profiles collected from Pro-SNA dispersed in buffers (B) – (D) below both the Rb^+ K-edge (15.2 keV) and the Sr^{2+} K-edge (16.1 keV) resulting in the extraction of the non-resonant and resonant intensity profiles in each case (Appendix A3, Sec A3.2).

In order to explore the competition between monovalent Rb^+ and divalent Sr^{2+} ions surrounding the Pro-SNA, we first consider the observed ASAXS effect due to both counterionic species as a function of bulk $SrCl_2$ concentration. The ASAXS effect discussed here is defined as the relative decrease observed in the forward scattered intensity I (q = 0) upon moving from an energy away from the edge (397 eV below) to an energy close to the edge (5 eV below). The ASAXS effect

[RbCl] (mM)	**[$SrCl_2$] (mM)**	**ASAXS effect (Rb^+)**	**ASAXS effect (Sr^{2+})**
50	0	10.9 %	--
45	5	10.2 %	0.7 %
40	10	7 %	5.2 %
30	20	4.9 %	6.6 %

Table 5.1: The ASAXS effect, defined as the decrease in the forward scattered intensity, I(q=0), when the incident x-ray energy is varied from well below the absorption edge (397 eV below) to just below edge (5 eV below), observed for Pro-SNA dispersed in buffers with varying concentrations of RbCl and $SrCl_2$.

observed at the Rb^+ and Sr^{2+} K-edges from samples dispersed in the four aforementioned buffers is summarized in Table 5.1.

As the concentration of $SrCl_2$ in the buffer is increased from 0 to 20 mM, the ASAXS effect from the Rb^+ counterions decreases from a maximum value of 10.9 % in 50 mM RbCl to 4.9% in 30 mM RbCl + 20 mM $SrCl_2$. This is accompanied by a concomitant increase in the ASAXS effect from Sr^{2+} indicating that as the concentration of $SrCl_2$ in solution is increased, a greater number of Sr^{2+} ions enter the counterion cloud surrounding the SNA. This is the intuitively expected result due to increase in the number of available divalent Sr^{2+} counterions in the bulk solution and the fact that the localization of a single divalent ion is more entropically favorable than the localization of two monovalent ions for the neutralization of a negative charge.[112] Up to 5 mM $SrCl_2$, the ASAXS effect from Sr^{2+} is negligible (0.7 %) and lower than the average experimental uncertainty suggesting that under these conditions Rb^+ is the predominant counterion for the DNA. Interestingly, in a buffer containing 20 mM $SrCl_2$, the ASAXS effect from Sr^{2+} is ~ 6.6 %, however that from Rb^+ is also significant (~ 4.9 %). Thus, at 20 mM $SrCl_2$, all the Rb^+ in the counterionic cloud is not replaced by Sr^{2+} counterions.

We next investigate trends in the forms of the non-resonant and resonant intensity profiles as a function of solution $SrCl_2$ concentration. Figure 5.3(A) shows the non-resonant intensity profiles isolated from Pro-SNAs suspended in buffers (A) – (C). As the concentration of $SrCl_2$ is increased, the position of the first minima in the profile is seen to shift to higher values of the scattering vector q. This indicates a reduction in radial extent of the DNA shell on the Pro-SNA. Such a compaction of the DNA induced by increasing solution ionic strength has been previously observed for the case of Pro-SNA suspended in buffers containing increasing concentrations of monovalent NaCl salt (Appendix A5). This effect is hypothesized to occur due to increased screening of the negative charge on the DNA at higher salt concentrations. The DNA may then assume a tighter and more folded conformation due to a reduction in the effective inter- and intra-strand columbic repulsion caused by the negatively charged DNA phosphate backbones. The resonant intensity profiles due to scattering from the Rb^+ counterions surrounding Pro-SNA suspended in buffers (A) – (C) (Fig. 5.3(B)) mirror this trend with the position of the first minima moving to higher values of q with increasing divalent Sr^{2+} ion concentration. This suggests that the decrease in the radial extent of the DNA shell is accompanied by a decrease in the extent of surrounding Rb^+ counterion cloud. Thus, as the DNA shell contracts in length with increasing divalent salt concentration, the cloud of Rb^+ counterions associated with the Pro-SNA also reduces in overall extent. In order to verify that the changes in the form of the resonant intensity profile from Rb^+ (Fig 5.3(B)) are not solely due to the changes in the non-resonant factor $F_0(q)$ in the resonant cross term ($\left(2F_0(q)v(q)\right)$), we extracted the term $v(q)$ using the measured non-resonant and resonant intensity profiles from Rb^+. The form of $v(q)$ also exhibits an increase in the q-position of the first minima with increasing $SrCl_2$ concentration (Appendix A3, sec A3.3) which validates the conclusion that the Rb^+ ionic cloud moves closer to the Pro-SNA core as the DNA shell contracts in length. The resonant and non-resonant intensity profiles from Rb^+ in Figs 5.3(A)-(B) have only been depicted for the case of buffers (A) –(C). For the case of buffer (D) (30 mM RbCl + 20 mM $SrCl_2$), the extracted profiles have uncertainties greater than 70% beyond 0.2 nm^{-1} (Appendix A3, Sec A3.2).

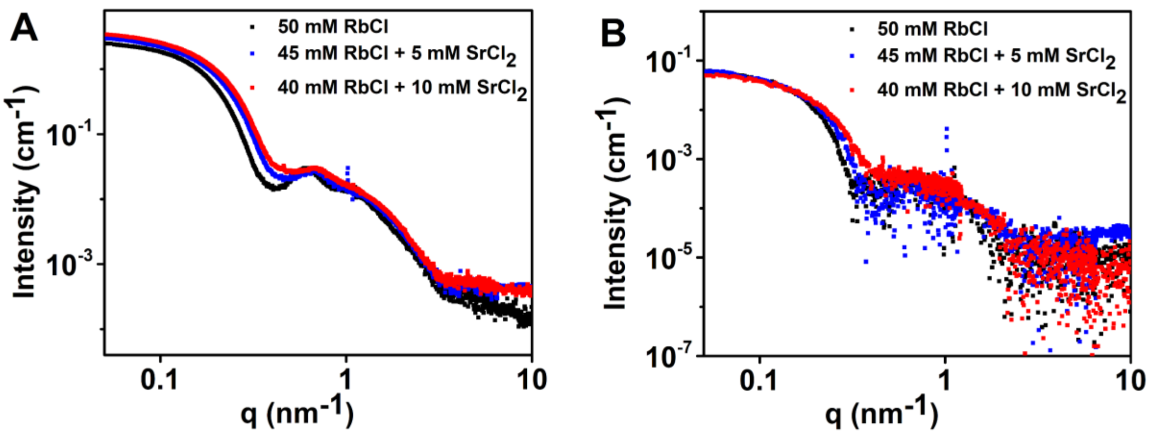

Figure 5.3: (A) Non-resonant and (B) Resonant Intensity profiles extracted from Pro-SNA dispersed in 50 mM RbCl (black), 45 mM RbCl + 5 mM $SrCl_2$ (blue) and 40 mM RbCl + 10 mM $SrCl_2$ (red). These profiles were extracted from SAXS profiles collected below the Rb^+ K-edge: while the non-resonant profiles are invariant of incident energy, the resonant cross term profiles contain the Fourier transform of the excess Rb^+ density, v(q), and hence depend on the distribution of Rb^+ ions surrounding the Pro-SNA.

A quantitative first-order approximation of the number of Rb^+ and Sr^{2+} ions within the DNA shell on a Pro-SNA may be obtained through an inspection of the forward scattered intensities, I (q = 0), measured close to and away from the Rb^+ and Sr^{2+} absorption edges. The forward scattered intensity measured at an incident energy E_{Rb1} (14.807 keV) away from the Rb edge is given by:

$$I_{Rb1} = \frac{N}{V}\left[\Delta F_0^2 + 2\left(f'_{Rb1} + if''_{Rb1}\right)\Delta N_{Rb}\Delta F_0\right] \tag{5.3}$$

Here, ΔF_0 is the total excess number of electrons from the Pro-SNA, $\Delta F_0 = F_0 - V_P\rho_S$, where F_0 is the total number of electrons in the Pro-SNA, V_P is the volume occupied by the Pro-SNA and ρ_S is the electron density of the solvent. f'_{Rb1} and f''_{Rb1} are the real and imaginary parts of the anomalous dispersion correction for Rb$^+$ at an energy E$_{Rb1}$. ΔN_{Rb} is the number of excess Rb$^+$ ions in the shell, $\Delta N_{Rb} = N_{Rb} - N_B$, where N_B is the number of Rb$^+$ ions from the bulk solvent in the volume occupied by the Pro-SNA. In a similar manner, the forward scattered intensity measured at an incident energy E$_{Rb2}$ (15.199 keV) close to the edge is given by:

$$I_{Rb2} = \frac{N}{V}\left[\Delta F_0^2 + 2\left(f'_{Rb2} + if''_{Rb2}\right)\Delta N_{Rb}\Delta F_0\right] \tag{5.4}$$

Subtracting Eqs. (5.3) and (5.4) gives:

$$\Delta I_{Rb} = \frac{N}{V}\left[2\,\Delta(f' + if'')_{Rb}\Delta N_{Rb}\Delta F_0\right] \tag{5.5}$$

where $\Delta(f' + if'')_{Rb} = \left(f'_{Rb1} + if''_{Rb1}\right) - \left(f'_{Rb2} + if''_{Rb2}\right)$. The imaginary part of the dispersion correction, f'', is practically constant at energies below an absorption edge and thus, $\Delta(f' + if'')_{Rb}$ reduces to the difference between the real parts of the dispersion correction: $f'_{Rb1} - f'_{Rb2}$. Similarly, if I_{Sr1} and I_{Sr2} represent the forward scattered intensities measured at energies E$_{Sr1}$ (15.817 keV) and E$_{Sr2}$ (16.109 keV) away from and close to the Sr^{2+} absorption edge, then the difference in these values is given by:

$$\Delta I_{Sr} = \frac{N}{V}\left[2\,\Delta(f' + if'')_{Sr}\Delta N_{Sr}\Delta F_0\right] \tag{5.6}$$

The ratio of Eqs. (5.5) and (5.6) gives the ratio of excess Rb$^+$ to Sr^{2+} ions in the DNA shell:

$$\frac{\Delta N_{Rb}}{\Delta N_{Sr}} = \frac{\Delta(f' + if'')_{Sr}\,\Delta I_{Rb}}{\Delta(f' + if'')_{Rb}\,\Delta I_{Sr}} \tag{5.7}$$

Using equation (5.7) and the measured values of ΔI_{Rb}, ΔI_{Sr}, $\Delta(f')_{Sr}$ and $\Delta(f')_{Rb}$, we can determine the ratio of excess Rb$^+$ to Sr^{2+} ions in the DNA shell of the Pro-SNA in each of the buffers, (B) – (D),(Table 5.2). Additionally, this ratio can be written as:

$$\frac{\Delta N_{Rb}}{\Delta N_{Sr}} = \frac{N_{Rb} - N_{B,Rb}}{N_{Sr} - N_{B,Sr}} \tag{5.8}$$

where $N_{B,Rb}$ and $N_{B,Sr}$ are the numbers of Rb^+ and Sr^{2+} ions in the volume occupied by the Pro-SNA from the bulk solvent at each concentration. These quantities can be estimated using the bulk number densities of Rb^+ and Sr^{2+} ions in the buffer and the volume of the Pro-SNA conjugate. To estimate the volume of the Pro-SNA, the protein core is considered ellipsoidal with semi-axes given by a = b = 5.05 nm; c = 3.5 nm and the DNA shell is considered to be 9 nm in length. Further, using the simplifying assumption that the total charge due to the DNA (Q_{DNA} = 1600) is completely compensated by Rb^+ and Sr^{2+}, we can write:

$$N_{Rb} + 2N_{Sr} = Q_{DNA} \tag{5.9}$$

Equations 5.8 and 5.9 can be solved for N_{Rb} and N_{Sr} to determine the approximate number of total Rb^+ and Sr^{2+} ions within the DNA shell. The results of these calculations are summarized in Table 5.2 below.

[RbCl] (mM)	[$SrCl_2$] (mM)	$\frac{\Delta \boldsymbol{N_{Rb}}}{\Delta \boldsymbol{N_{Sr}}}$	$\boldsymbol{N_{Rb}}$	$\boldsymbol{N_{Sr}}$
50	0	-	-	-
45	5	10.6	1337	131
40	10	0.91	634	482
30	20	0.53	429	585

Table 5.2: Ratio of excess Rb^+ ions to Sr^{2+} ions in the DNA shell on a Pro-SNA and rough estimates of the number of Rb^+ and Sr^{2+} ions localized in the DNA shell.

At 5 mM $SrCl_2$, the number of Rb^+ ions are found to be ~ 10 times greater than the number of Sr^{2+} ions in the shell, indicating that Rb^+ is the predominant counterion in the shell under this condition neutralizing approximately ~ 83% of the negative charge due to the DNA. However, at 10 mM $SrCl_2$, Sr^{2+} ions outcompete Rb^+ as the primary counterion for the DNA and compensate ~ 60 % of the charge on the DNA. The ratio of Rb^+ to Sr^{2+} in the DNA shell is further decreased (0.53) when the concentration of $SrCl_2$ is increased to 20 mM. At this concentration, Sr^{2+} counterions compensate ~ 73% of the charge on the DNA. These estimates may be benchmarked against predictions from the Poisson-Boltzmann equation and ion density profiles computed using Molecular Dynamics simulations.

Conclusions

Overall, our use of ASAXS to probe the distributions of Rb^+ and Sr^{2+} surrounding the Pro-SNA has revealed the following key insights:

(i) ASAXS is a sensitive probe of the competing distributions of monovalent Rb^+ and divalent Sr^{2+} surrounding Pro-SNA: The relatively low electron density of the Catalase core and DNA shell components coupled with the enhanced local concentration of Rb^+/Sr^{2+} due to the high negative charge on the DNA ensures the feasibility of ASAXS to discern the scattering from the counterionic cloud. In particular, we find a maximal ASAXS effect from Rb^+ of 11% in 50 mM RbCl demonstrating the sensitivity of ASAXS to scattering from Rb^+. This in turn enabled an extraction of the Rb^+/Sr^{2+} counterion dependent resonant scattering profiles over a range of solution conditions.

(ii) The ASAXS effect from Rb^+ decreases while that from Sr^{2+} increases with increasing bulk $SrCl_2$ concentration: As the concentration of $SrCl_2$ in solution is increased from 0 to 20 mM while

keeping the total cation concentration constant (50 mM), the ASAXS effect measured from the Rb^+ counterions is seen to decrease from ~ 11% (50 mM RbCl) to ~ 5 %(30 mM RbCl + 20 mM $SrCl_2$) while that from $SrCl_2$ is seen to increase from ~ 0.7 % (45 mM RbCl + 5 mM $SrCl_2$) to ~ 6.6 % (30 mM RbCl + 20 mM $SrCl_2$) suggesting that a greater number of Sr^{2+} begin populating the counterion cloud. However, in this buffer (30 mM RbCl + 20 mM $SrCl_2$), the finite ASAXS effect measured from Rb^+ suggests that the Rb^+ is not completely outcompeted by Sr^{2+} in the DNA shell.

(iii) The radial extent of the DNA shell and its associated counterionic cloud decrease with increasing divalent ion concentration: As the concentration of Sr^{2+} ions in the bulk is increased, the negative charge on the DNA backbone is effectively screened to a greater extent, allowing the DNA shell to assume a more compact form. This is accompanied by a proportional contraction in the overall radial extent of the Rb^+ counterionic cloud associated with the Pro-SNA as evidenced by the shift of the minima positions of the resonant and non-resonant intensity profiles to higher values of q. This indicates that while the spatial distribution of the counterions changes with increasing divalent salt concentration, this change is induced by the compaction of the DNA shell. Thus, the relative spatial distribution of the counterions with respect to the DNA shell remains conserved in spite of the increase in the number of Sr^{2+} in the counterion cloud. This result has been previously reported in a similar study of the competing distributions of Rb^+ and Sr^{2+} counterions surrounding free DNA[115] and is supported by predictions of the Poisson-Boltzmann model.[116-117] Further, a qualitative estimate of the ratio of excess Rb^+ ions to Sr^{2+} ions in the DNA shell as a function of solution salt concentration reveals that at ~ 10 mM $SrCl_2$, Sr^{2+} outcompete Rb^+ in the counterion cloud.

We have successfully demonstrated the use of Anomalous Small Angle X-ray Scattering to distinguish the scattering contributions from two different charge-neutralizing counterionic species surrounding a Pro-SNA. Through this study we have explored the competition between monovalent Rb^+ and divalent Sr^{2+} in the counterionic cloud in different bulk salt concentration regimes. These results should aide our understanding of the composition of the counterionic cloud surrounding a Pro-SNA as it migrates between biological environments consisting of varying concentrations of ionic species, which in turn should be invaluable towards designing stable Pro-SNAs for therapeutic and transfection applications.

Proposed Future Work

We propose the use of structural modelling to derive the nanoscale attributes of the Pro-SNA as a function of salt concentration including the lengths and average electron densities of the protein core, DNA and linker components. In order to obtain a more detailed quantitative picture of the shape of the Rb^+ and Sr^{2+} counterion distribution profile surrounding a Pro-SNA, we propose the use of Molecular Dynamics to determine the ion density profile under the four experimentally probed solution conditions. The protein core will be modelled as an uncharged ellipsoid with a uniform density and semi-axes given by $a = b = 5.05$ nm; $c = 3.5$ nm while the dsDNA will be modeled using a coarse-grained DNA bead model where each bead represents 2 base pairs and thus has a charge of -4. The linker is also modelled using a bead model such that the total charge on each linker is -3. The system will also include mono and divalent counterions at concentrations that mimic buffers (A)-(D) used in the experiment. This system will be run at a temperature of 298

K and snapshots of ionic positions over the course of the simulation time will be used to derive the ionic density profiles n(**r**). The Fourier transform of these excess density profiles can then be used for comparison to the ASAXS extracted resonant cross term profiles. This approach should allow us to map the local Rb^+ and Sr^{2+} concentrations surrounding the construct and determine the number of each species in the counterionic cloud as a function of bulk salt concentration.

Chapter 6: Summary and Outlook

In the preceding chapters a detailed exploration of the nanoscale structure, counterionic environment and enzymatic degradation mechanisms pertaining to Protein Spherical Nucleic Acid conjugates was presented. Our scientific approach highlighted the power of In-situ Small Angle X-ray Scattering in conjunction with other biophysical characterization tools towards elucidating structure-function relationships in Pro-SNAs and established strategies for the nanoscale characterization of similar complex and highly charged macromolecular constructs.

First, a complete nanometer-scale description of the structural attributes and local ionic environment surrounding a Pro-SNA was provided through the use of a combined Anomalous SAXS and DFT based approach. Conventional SAXS allowed access to the lengths and electron densities of the components of a Pro-SNA while ASAXS enabled a mapping of the Rb^+ counterionic concentrations surrounding a Pro-SNA. In particular, Rb^+ ion density profiles as a function of radial distance from the center of the protein core revealed that the negative charge of a Pro-SNA is undercompensated within the DNA shell (~ 90%) and that the Rb^+ counterionic cloud extends approximately 1.3 nm beyond the shell to completely neutralize the charge on the Pro-SNA. Further, it was found that the highly negatively charged DNA on a Pro-SNA causes a 3.5-fold enhancement of the Rb^+ concentration in the vicinity of the DNA shell (175 mM) in comparison to the bulk solution (50 mM). These findings provide fundamental insight into the potential energy landscape surrounding a Pro-SNA and should provide a roadmap towards understanding the electrostatic interactions of Pro-SNAs with solution bound species including enzymes, small molecules and ionic species.

One such interaction intimately tied to the counterionic cloud surrounding an SNA and profoundly related to its physiological stability is that with the intracellular nuclease – DNase I. The interaction between DNase I and a Pro-SNA is explored in detail in Chapter 4 where time course SAXS measurements, Gel Electrophoresis and Molecular Dynamics simulations are used to shed light on the structural modifications, reaction mechanism and counterionic cloud composition during the course of the enzymatic degradation of Pro-SNA by DNase I. Importantly, a label-free x-ray scattering approach allowed us to quantitatively monitor the degradation reaction in-situ and revealed a two-state reaction pathway wherein Pro-SNAs are either in an intact or completely degraded state without the formation of any measurable intermediates. This discovery was corroborated with Gel Electrophoresis measurements and guided the hypothesis that the reaction pathway is composed of a slow, rate determining DNase I – Pro-SNA association step and a rapid DNase I mediated DNA hydrolysis step. This unique reaction pathway is facilitated by the high density of DNA on the SNA surface which essentially templates the enzymatic degradation reaction. These considerations are relevant to conditions wherein the relative concentration of the

Pro-SNA is low and therefore should be especially instructive towards understanding the serum interactions of Pro-SNAs in therapeutic applications. Additionally, unlike traditional fluorescence-based assays, in-situ SAXS measurements can efficiently access macroscopic structural information associated with SNAs subjected to enzymatic degradation. In particular, both structural modelling and model-independent PDDF analyses reveal that the entirety of the DNA functionalized onto the Pro-SNA is digested by DNase I during the course of the reaction. Thus, in addition to illuminating the Pro-SNA-DNase I reaction pathway, we have established the use of a powerful label-free approach to probe enzymatic reactions in situ.

Finally, we investigated the competition between mono- and divalent counterions surrounding a Pro-SNA as a function of varying bulk solution conditions. The question of preferential ion binding is of vital significance in the context of SNAs which are expected to migrate between varying ionic environments in their biological applications. Through the use of Anomalous SAXS we simultaneously probed the distributions of Rb^+ and Sr^{2+} counterions surrounding Pro-SNAs as a function of bulk Rb^+ and Sr^{2+}. While the relative spatial distributions of the Rb^+ and Sr^{2+} counterionic cloud remain invariant with changing bulk solution concentration, a result predicted by the Poisson-Boltzmann equation, the numbers of these ionic species within the DNA shell changed to mirror their concentrations in the bulk solution. Further, increasing the solution ionic strength was found to increase the extent of electrostatic screening resulting in a compaction of the DNA shell and a concomitant decrease in the radial extent of the counterionic cloud surrounding the Pro-SNA. These results should enable a prediction of the stability of Pro-SNAs against degradation by salt-sensitive enzymes in intracellular transfection applications and aide studies aimed at enhancing their physiological stability.

Appendix

A1. Supporting Information for Chapter 3

A1.1. ASAXS Model calculations

Here we demonstrate the feasibility of ASAXS for our Pro-SNA Rb^+ case. Determination of the structure of the counterion cloud relies on the measurement of subtle changes in the scattered intensity from a DNA nanoparticle-counterion system which arise due to sharp modulations in the effective scattering strength $f\,(q,\,E)$ of the counterion in the vicinity of a core-electron binding energy:

$$f(q,E) = f_0(q) + f'(E) + if''(E) \tag{A1.1}$$

Here $f_0\,(q)$ is the energy independent form factor for the ion. In the small angle limit, $f_0\,(q) \sim Z$, the number of electrons in the ion. $f'\,(E)$ and $f''\,(E)$ are the energy dependent real and imaginary parts of the dispersion correction. For the case of Rb^+, the expected variation of $f'\,(E)$ and $f''\,(E)$ with energy in the vicinity of a K absorption edge[118] (15.200 keV) is shown in Fig. A1.1 (A). In order to avoid strong fluorescence above an X-ray absorption edge, ASAXS measurements are typically performed at photon energies below the absorption edge of the targeted ion.[31, 59] At energies below the Rb K absorption edge the imaginary part of anomalous dispersion correction $f''\,(E)$ is practically zero (Fig. A1.1 (A)). Thus, the ASAXS effect is primarily dictated by $f'\,(E)$. We have performed model calculations 5 eV below the edge where $f'\,(E) = -7.58$.[118] Following Dingenouts et. al.,[31] the energy dependent scattered intensity from a Pro-SNA-Rb^+ system above scattering from the salt solution can be written as:

$$I(q,E) - I_{RbCl}(q,E) = \frac{N}{V}\left[\,|F_0(q)|^2 + f'(E)\,(2F_0(q)v(q)) + \left(f'(E)v(q)\right)^2\right] \qquad \text{(A1.2)}$$

Here $I(q,E)$ and $I_{RbCl}(q,E)$ represent the scattered intensities from the 50 mM RbCl solution with and without the Pro-SNA conjugate respectively. $\frac{N}{V}$ is a scale factor proportional to the concentration of the Pro-SNA. The first term of the above equation is independent of energy and is equal to the scattered intensity from the Pro-SNA-Rb$^+$ system at energies far below the Rb K edge. This term is modelled using a core-shell form factor[119] as follows:

$$F_0(q) = 3V_p(\rho_p - \rho_D)\frac{[\sin q R_p - qR_p \cos qR_p]}{(qR_p)^3} + 3V_t(\rho_D - \rho_s)\frac{[\sin q R_t - qR_t \cos qR_t]}{(qR_t)^3} \qquad \text{(A1.3)}$$

The bare protein is modelled as a sphere with a radius R_p = 4.5 nm and a uniform electron density ρ_p = 403 e$^-$/nm^3. The protein electron density (ρ_p) is extracted using CRYSOL[67] and the corresponding protein data bank entry for the Catalase enzyme[120] (PDB 4B7F). The DNA shell is modelled as having a thickness t = 9 nm which is inclusive of both the ssDNA strand (D) and the linker (L) segment covalently attaching the DNA to the protein core. The model does not take into account the electron density contrast between the linker and DNA segments and instead assigns an effective electron density ρ_D = 346 e$^-$/nm^3 to the DNA shell. The total radius of the conjugate is R_t = R_p + t = 13.5 nm. The electron density of the surrounding 50 mM RbCl solution is ρ_s = 333.28 e$^-$/nm^3. V_p and V_t are the volumes of the protein core and the DNA functionalized protein respectively. The second energy dependent term of Eq. A1.2 additionally contains $v(q)$, the

Fourier transform of the excess Rb$^+$ density. Assuming that the Pro-SNA-Rb$^+$ system is spherically symmetric, $v(q)$ can be written[32] as:

$$v(q) = 4\pi \int_0^\infty [n_{Rb}(r) - n_B] \frac{\sin qr}{qr} r^2 dr \qquad \text{(A1.4)}$$

Here $n_{Rb}(r)$ is the number density of Rb$^+$ as a function of radial distance from the center of the conjugate and n_B is the number density in the bulk solution far away from the conjugate. For 50 mM RbCl, n_B = 0.03 ions/nm^3. In order to compute $v(q)$, a simplified geometric model is used for the excess Rb$^+$ density as follows:

$$n_{Rb}(r) - n_B = \begin{cases} -n_B, & r < R_p \\ n_l - n_B, & R_p < r < R_p + L \\ \left(\dfrac{N_{DNA} \times N_b}{4\pi t r^2}\right) - n_B, & R_p + L < r < R_t \\ 0\,, & r > R_t \end{cases}$$

(A1.5)

The Rb$^+$ density is set to zero ($n_{\mathrm{Rb}}(r) = 0$) in the region occupied by the protein core. Since each linker group (with length L) has a charge of -3e$^-$, the linker region is assigned a uniform Rb$^+$ charge density (n_l = 0.08661/ nm^3) equal to the Rb$^+$ density required to neutralize the linker's negative charge. The excess Rb$^+$ density in the linker region is thus given by $n_l - n_B$. Within the DNA shell it is assumed that the excess Rb$^+$ density follows the charge density of the DNA. Namely, each unit of negative charge on the DNA is compensated by a corresponding Rb$^+$ which occupies the same radial position as the negative charge it neutralizes. Since the Pro-SNA-Rb$^+$ system is assumed to be spherically symmetric, the excess Rb$^+$ density is modeled to fall off as the inverse square of r within the DNA shell. This is reflected in Eq. A1.5 where N_{DNA} refers to the number of DNA strands per protein and N_b refers to the number of bases per DNA strand. The number of DNA strands per protein, N_{DNA} is set to 40 – this loading density was determined using UV-Vis absorption spectroscopy using the known molar extinction coefficients for the protein (ε_{405} = 324,000 M^{-1} cm^{-1}) and DNA (ε_{260} = 188,300 M^{-1} cm^{-1}). The number of DNA bases N_b in our chosen DNA sequence is 18. Finally, the excess Rb^+ density is set to zero beyond the DNA shell. The calculated partial intensities corresponding to the first, second and third terms of Eq. A1.2 are shown in Fig. A1.1 (B). At $q = 0$, the ratio of the second to the first term of Eq. A1.2, $2|F_0(q)f'(E)v(q)|/[F_0(q)]^2 = 0.073$ which implies that in going from an X-ray energy far below the Rb K-edge to an energy 5 eV below the edge, the change in the second term of Eq. A1.2 is ~ 7.3% which should be measurable above typical experimental uncertainties. The third term, however, is 3 orders of magnitude lower than the non-resonant term$[F_0(q)]^2$. In particular at $q =$ 0, $[f'(E)v(q)]^2$ / $[F_0(q)]^2$ = 0. 0013.This implies that the third term in Eq. A1.2 changes by only 0.13 % upon going from an X-ray energy far below the K-edge to one 5 eV below the edge. Such changes are lower than the typical statistical uncertainties of the experiment and cannot be measured reliably. Thus, we will neglect the third term $[f'(E)v(q)]^2$ of Eq. A1.2 in the subsequent analysis. This approximation is further supported by an analysis of experimental SAXS data as described in detail below.

An inspection of SAXS profiles from the Prot-DNA measured at 5 eV and 398 eV below the Rb K-absorption edge can be used to estimate the relative magnitudes of the non-resonant term, cross term and pure resonant term. At an incident energy 5 eV below the edge, the background subtracted intensity can be written as:

$$I_{on}(q,E) = \frac{N}{V}[\,|F_0(q)|^2 + f'(E)\,(2F_0(q)v(q)) + \left(f'(E)v(q)\right)^2] \qquad \text{(A1.6)}$$

At an incident energy 398 eV below the edge, resonant effects are expected to be negligible and the measured scattered intensity is given as:

$$I_{off}(q,E) = \frac{N}{V}[\,|F_0(q)|^2] \qquad \text{(A1.7)}$$

The ratio of the intensities measured on and off the absorption edge can be obtained by dividing eq. (1) and (2) and is given by:

$$\left[\frac{f'(E)v(q)}{F_0(q)}\right]^2 + \frac{2f'(E)v(q)}{F_0(q)} + 1 = \frac{I_{on}(q,E)}{I_{off}(q,E)} \qquad \text{(A1.8)}$$

For small values of q (q < 0.2 nm^{-1}), $v(q)$ is expected to be positive and the above quadratic equation can be solved to obtain the ratio of the pure resonant term to the leading non-resonant term, $\left[\frac{f'(E)v(q)}{F_0(q)}\right]^2$. For the case of 1μM Prot-DNA-Rb$^+$, ratio of the scattered intensities measured 5 eV and 398 eV below the edge ($\frac{I_{on}(q,E)}{I_{off}(q,E)}$) at q = 0.083 nm^{-1} is 0.91. Thus, the ratio $\left[\frac{f'(E)v(q)}{F_0(q)}\right]^2$ is 0.0021, indicating that the pure resonant term is only 0.2 % of the leading non-resonant term.

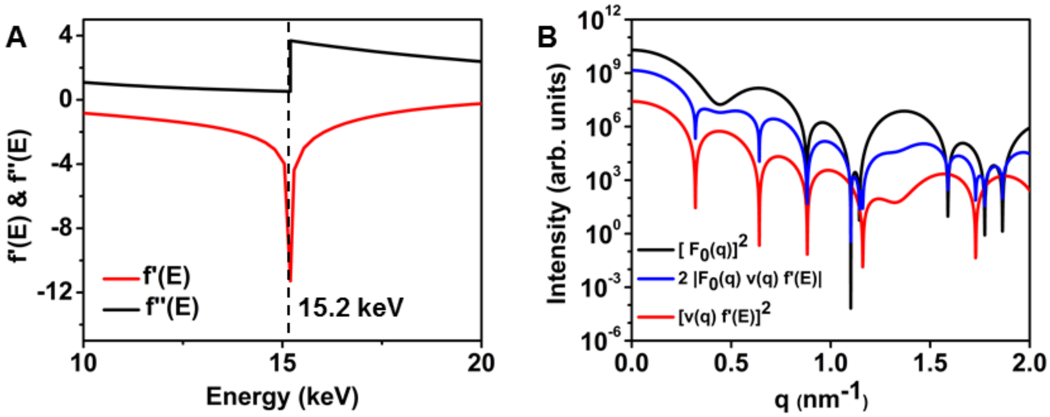

Figure A1.1: (A) Expected variation of f' (E) and f'' (E) with incident photon energy for Rb^+ in the vicinity of the K absorption edge (15.200 keV). (B) Model calculations of the non-resonant (black) and resonant (blue & red) terms of Eq. A1.2 for Pro-SNA dispersed in 50 mM RbCl. These calculations were performed for an incident photon energy that is 5 eV below the K-edge where f' (E) = -7.58.

A1.2. Determination of Rb K absorption edge and *f' (E)*

In order to calibrate the position of the Rb K-absorption edge and experimentally determine the value of the anomalous dispersion correction *f' (E)* as a function of incident photon energy in the vicinity of the edge, the transmitted intensity from a 1 M RbCl solution was measured over a 100 eV energy range around the expected Rb K edge (15.200 keV). A plot of the transmitted intensity as a function of incident photon energy is shown in Fig. A1.2 (A). The position of the Rb

K edge was experimentally determined to be at 15.202 keV. The slight deviation in the measured value of the K-edge from its expected value is due to the resolution of the monochromator. The real [*f'* (*E)*] and imaginary [*f''* (*E*)] parts of the anomalous dispersion correction were determined using CHOOCH[62], a program that produces *f'* (*E*) and *f''*(*E*) curves using a user supplied transmission or fluorescence energy scan. Briefly, the program evaluates *f'' (E)* using the optical theorem[121]:

$$f''(E) = \frac{mc\varepsilon_0 E\mu_a}{e^2\hbar} \tag{A1.9}$$

Here μ_a is the absorption coefficient of the targeted atom and the physical constants have their usual meaning. CHOOCH determines *f'* (*E*) by numerically integrating the Kramers-Kronig transformation:

$$f'(E_0) = \frac{2}{\pi}\oint \frac{Ef''(E)}{E_0^2 - E^2}\, dE \tag{A1.10}$$

E_0 is the absorption edge of the targeted element which in our case is Rb with a K-edge $E_k = 15.200$ keV. Using these expressions CHOOCH determines the value of *f'* (*E*) and *f''* (*E*) directly from knowledge of the absorption coefficient as a function of energy. The determined *f'* (*E*) and *f''* (*E*) are shown in Fig. A1.2 (B) in red and black respectively.

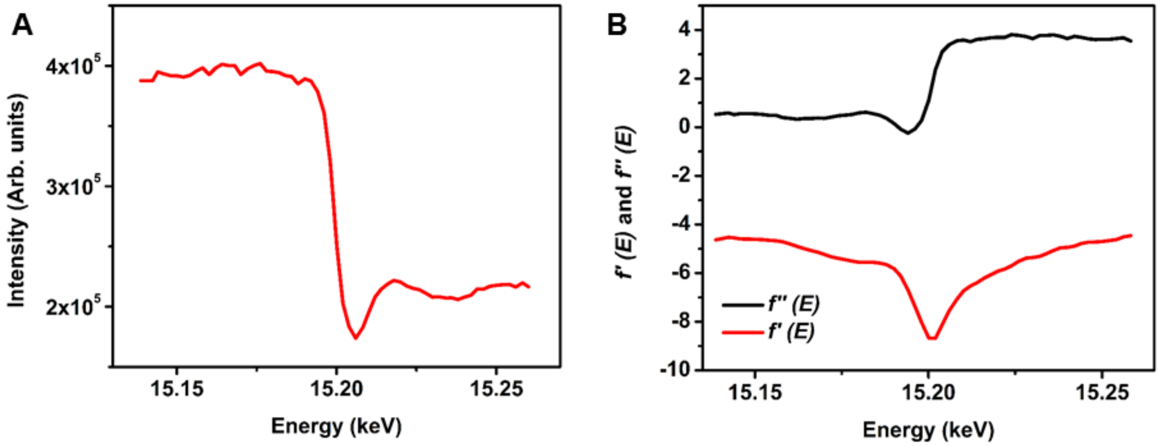

Figure A1.2: (A) Transmitted intensity from a 1 M RbCl solution as a function of incident photon energy in the vicinity of the K absorption edge (E_K = 15.202 keV). (B) The variation in $f'(E)$ (red) and $f''(E)$ (black) near E_K.

A1.3. ASAXS of bare protein and charge on protein

The isoelectric point (pI) of the native Catalase enzyme is 5.4[63]. A theoretically calculated[64] pH titration curve showing the surface charge on a Catalase enzyme as a function of solution pH is depicted in Fig. A1.3 (A). Fig.A1.3 (A) shows that the surface charge on a native protein in 50 mM RbCl solution is negligible in comparison to the charge of the DNA coating (-840). For instance, at pH 7 the charge on the protein is -17. Accordingly, the native enzyme is not expected to exhibit a significant ASAXS effect in the vicinity of the Rb K edge. This is validated by ASAXS measurements on bare proteins. Figure A1.3 (B) shows SAXS profiles of a bare protein at a 1 µM concentration in 50 mM RbCl at four incident photon energies below the Rb K-edge. At $q = 0$, the difference in the scattered intensities for the largest incident energy change (between $E_K - E = 379.1$

eV and E_K - E = 5.1 eV) is ~ 0.4%. In comparison, the change in the scattered intensities (at q = 0) for a Pro-SNA for the largest incident energy change is ~ 10%. This demonstrates that the protein core does not have an appreciable influence on the excess Rb^+ ion distribution surrounding the Pro-SNA.

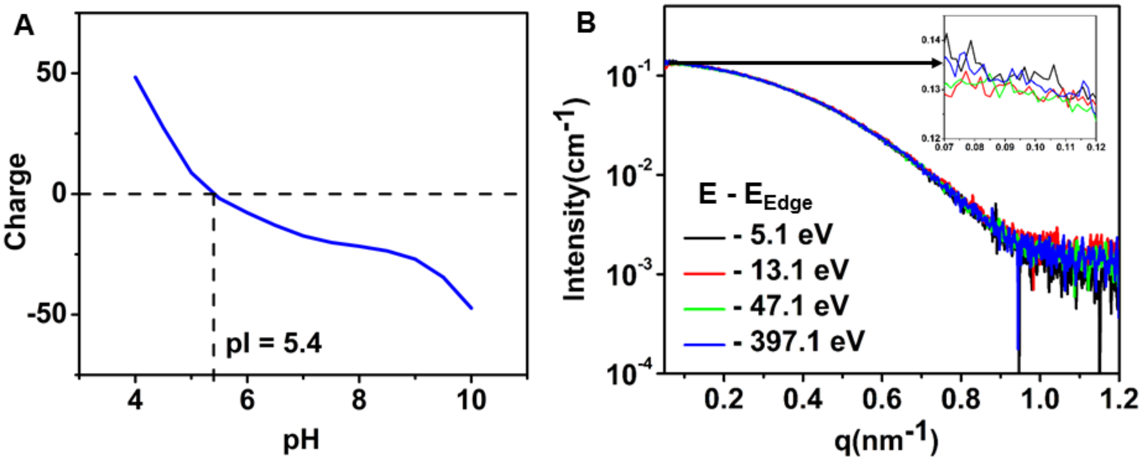

Figure A1.3: (A) Theoretical pH titration curve for *Cg* Catalase showing the variation of surface charge with solution pH. Catalase has an isoelectric point (pI) of 5.4. (B) SAXS profiles from a native Catalase enzyme at four energy points below Rb K-edge (E_k = 15.202 keV).

A1.4. Extraction of resonant and non-resonant terms: Linear fit procedure

In order to extract the first and second terms of Eq.A1.2, a linear fit to the $I(q, f'(E))$ vs. $f'(E)$ data is carried out for each 'q' in the range 0.05 – 1.2 nm^{-1} resulting in the extraction of the resonant $[\frac{N}{V}(2F_0(q)v(q))]$ and non-resonant $(\frac{N}{V}[F_0(q)]^2)$ profiles. This procedure is summarized for the case of 1 µM Pro-SNA below. A similar procedure was employed for the case of 4 µM Pro-SNA.

SAXS profiles from a 1 µM Pro-SNA-Rb$^+$ system at 4 incident photon energies below the Rb K edge (15.2 keV) are shown in Fig. A1.4 (A). Intensity data on a linear scale at low q (Fig. A1.4 (B), inset) exhibits the expected trend, with the scattered intensity lowest for $E - E_{Edge}$ = -5.1 and increasing with increasing $E - E_{Edge}$ since $F_0\,(q)$ and $v\,(q)$ are both positive at low q. At q = 0.3 nm^{-1}, $v\,(q)$ crosses the x-axis (Fig. A1.4 (E), red) as a result of which the measured scattered intensities at the 4 energies are equivalent, as indicated in Fig. A1.4 (B). Between q = 0.3 nm^{-1} and q = 0.6 nm^{-1}, $v\,(q)$ is negative [Fig. A1.4 (E)] as a result of which the trend in the SAXS profiles is reversed. The cross-over point in the SAXS intensity profiles is depicted in Fig.A1.4 (B) (top inset).Figs. A1.4 (C) – (D) show examples of linear fits to $I(q, f'(E))$ vs. $f'(E)$ before and after the crossover point: Fig. A1.4(C) shows a fit at q = 0.08 nm^{-1} where the slope ($2F_0(q)v(q)$) and y-intercept ($[F_0(q)]^2$) are both positive. At q = 0.33 nm^{-1} (Fig. A1.4 (D)), the slope becomes negative – this represents the position of the first minima in the resonant term (Fig. A1.4 (F), red curve). Fig. A1. 4 (F) shows the results of this extraction over an extended q-range (0.05 – 1.2 nm^{-1}).

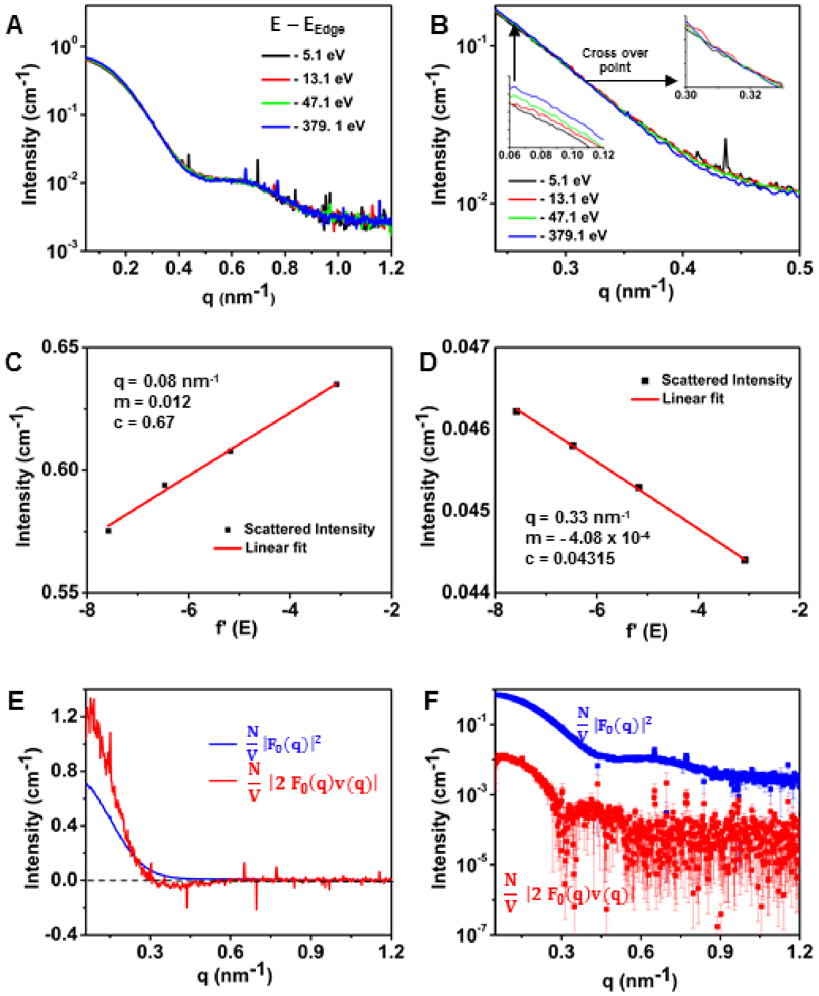

Figure A1.4: (A) SAXS profiles from 1μM Pro-SNA-Rb^+ at 4 incident photon energies below the Rb K edge. (B) SAXS intensity profiles between $q = 0.2 – 0.5$ nm^{-1} depicting the position of the crossover point at $q = 0.3$ nm^{-1}. The insets show magnified intensities on a linear scale before and after the crossover point. Examples of linear fits to $I(q, f'(E))$ at $q = 0.08$ nm^{-1} (C) and 0.3 nm^{-1} (D). (E) Linear scaled $\frac{N}{V}|2F_0(q)v(q)|$ (red) and $\frac{N}{V}|F_0(q)|^2$ (blue) profiles depicting the zero crossings of $\frac{N}{V}|2F_0(q)v(q)|$ due to the effect of v (q). (F) Log scaled $\frac{N}{V}|2F_0(q)v(q)|$ (red) and $\frac{N}{V}|F_0(q)|^2$ (blue) intensity profiles over an extended q-range.

A1.5. Bare Protein: SAXS Profile fitting

In order to extract the radius of the protein core (R_p) for subsequent fitting, the SAXS profile for an unmodified protein was fit with a model which employs the form factor of a homogenous sphere with a uniform electron density[119]:

$$F_p(q) = -3r_e V_p\left(\rho_p - \rho_s\right)\frac{[\sin qR_p - qR_p \cos qR_p]}{(qR_p)^3} \qquad \text{(A1.11)}$$

The protein core and surrounding RbCl solution are assigned uniform electron densities ρ_p = 403 e^-/nm^3 and ρ_s = 333.28 e^-/nm^3 respectively. r_e is the classical electron radius given by $r_e = 2.8179 \times 10^{-13}\, cm$ used to convert the intensity to an absolute scale. The model is fit to the data using the protein concentration and radius R_p as parameters. The best fit of the spherical form factor model to the SAXS profile of a bare protein is depicted in Fig.A1.5 (A). The best-fit value obtained for the protein radius (R_p) is 4.5 nm. The SAXS profile evaluated by CRYSOL[67] using the atomic coordinates from the protein data bank entry (PDB 4B7F) for Catalase[120] is also depicted in Fig. A1.5 (A). Given the experimental range (q < 1.2 nm^{-1}) where the scattered intensity is measurable above the background, the close shape agreement between the SAXS profiles generated using the spherical form factor model (Eq. A1.11) and CRYSOL demonstrates the validity of modeling the protein as a spherical core. Further, this corresponds to a radius of gyration $R_g = \sqrt{(3/5)} \times R_p$ = 3.5 nm which is close to the value predicted by CRYSOL (R_g = 3.7 nm). Additionally, Guinier analysis was performed for the bare protein SAXS profile to estimate R_g in a model independent manner. Briefly, in the Guinier region of the data ($qR_g <\sim 1$), the scattered intensity can be approximated by the Guinier equation[119]:

$$\ln I\,(q) = \ln\,(I_0) - \frac{q^2 R_g^2}{3} \qquad \text{(A1.12)}$$

A linear fit to the $Ln\, I\,(q)$ vs q^2 data described by Eq. A1.12 yields the radius of gyration R_g as the slope. Fig. A1.5 (B) depicts a Guinier plot for the unmodified protein along with the corresponding linear fit. The radius of gyration determined through this approach is 3.77 nm which is in close agreement with that predicted by CRYSOL.

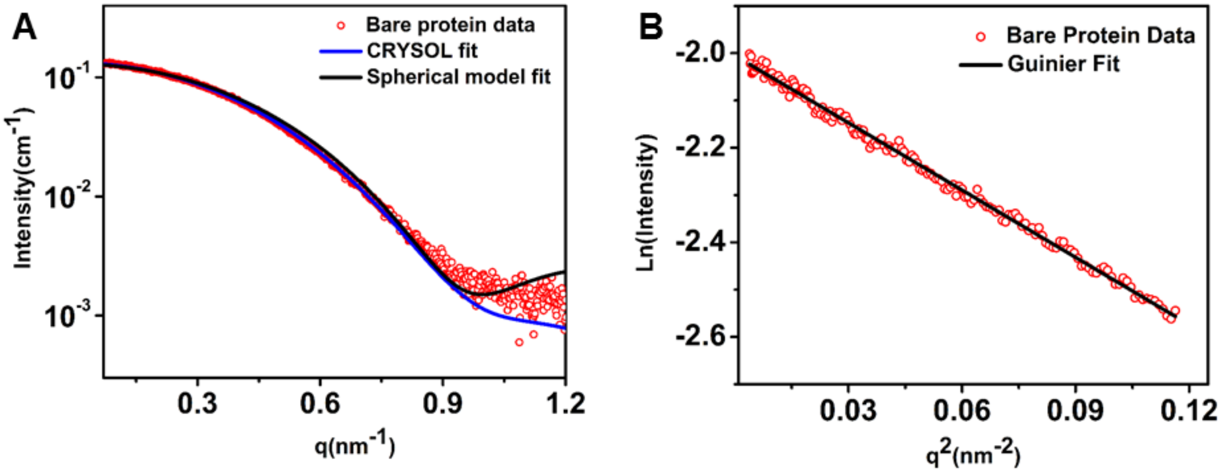

Figure A1.5: (A) SAXS profile of the bare protein (red) and fits using a spherical form factor model (black) and CRYSOL (blue). (B) Guinier plot for the bare protein (red) and the corresponding linear fit (black). The slope and y-intercept of the fit are -4.74 and -2.0 respectively.

A1. 6. Core-Shell model for Non-resonant term and fitting

Following the linear fit procedure outlined in section A1.4, the first two intensity contributions to Eq. A1.2 were extracted: the non-resonant ($\frac{N}{V}|F_0(q)|^2$) and resonant ($\frac{N}{V}\ |2F_0(q)v(q)|$) intensity profiles [Figs. 3.3(C) and (D)]. The non-resonant intensity is equivalent to the scattering from the Pro-SNA, ions and water at X-ray energies away from the Rb K-edge and is modeled using a spherical core-shell model. The protein is modeled as a sphere having a fixed radius of $R_p = 4.5$ nm (section A1.5) and a uniform electron density of 403 e/nm^3. The oligonucleotide shell is composed of linker segments and single stranded DNA, which are modeled as cylindrical rods with a radius of 0.5 nm.[122] The number of electrons in the linker and DNA segments is fixed based on the chemical composition of the linker and DNA. The number of DNA + linker strands per protein was set to $N_{DNA} = 40$ based on the average loading density experimentally determined through UV-Vis absorption spectroscopy. The lengths of the linker (L) and DNA (D) segments and the concentration of the Pro-SNA conjugates (c) are used as fitting parameters. This concentration is related to the scale factor N/V appearing in both the non-resonant and cross term intensity profiles. The multiplicative scale factor N/V is given by:

$$\frac{N}{V} = c \times 6.022 \times 10^{14}\ cm^{-3} \tag{A1.13}$$

The non-resonant intensity profile ($\frac{N}{V}|F_0(q)|^2$) was thereafter fit to a spherical core shell model function[119] given by:

$$I_{NR}(q) = \frac{N}{V}\,[F_o(q)]^2 + bkg \tag{A1.14}$$

$$F_0(q) = F_1(q) + F_2(q) + F_3(q) \tag{A1.15}$$

$$F_1(q) = -3r_e V_p(\rho_p - \rho_s)\frac{[\sin q\,R_p - qR_p\cos qR_p]}{(qR_p)^3}$$

$$F_2(q) = -r_e\,\pi r_o^2 N(\rho_L - \rho_s)\int_{R_p}^{R_p+L}\frac{\sin qr}{qr}dr$$

$$F_3(q) = -r_e \pi r_o^2 N(\rho_D - \rho_s) \int_{R_p+L}^{R_p+L+D} \frac{\sin qr}{qr} dr$$

Here, $\frac{N}{V}$ is the particle concentration dependent scale factor described by Eq. A1.10. V_p and V_t refer to the volume of the protein core and the DNA functionalized protein respectively, calculated using a radius of R_p = 4.5 nm for the protein and a radius of $R_t = R_p + L + D$ for the functionalized protein. The electron densities of the solvent, protein core, linker and DNA segments are given by ρ_s, ρ_p, ρ_L and ρ_D respectively. The experimentally extracted non-resonant intensity profile is then fit to the core-shell model described by Eq. A1.15 using non-linear least squares curve fitting with constraints placed on the fitting parameters. The best fit of this model to the experimentally extracted non-resonant intensity profile is shown in Fig 3.4 for the two protein concentrations studied. The optimized values of *c, D and L* are listed in Table 3.1.

A1. 7. DFT derived Rb$^+$ distribution profile to fit cross-term

Density functional theory was used to compute ion density profiles surrounding the Pro-SNA for a bulk RbCl concentration of 50 mM. The Fourier transform of the excess Rb$^+$ density profile yielded *v(q)* which was then multiplied by *F*$_0$*(q)* and the protein concentration-dependent scale factor *N/V* to obtain the resonant cross term profile ($\frac{N}{V}$ $|2F_0(q)v(q)|$) which was then directly compared to its ASAXS extracted counterpart. The Rb$^+$ density was computed for various combinations of linker and ssDNA lengths. The linker length was varied between 2.5 nm and 6.5

nm in 0.5 nm increments. The ssDNA length was varied between 2.5 nm and 7.5 nm in 0.5 nm increments. Therefore, 9 x11 = 99 combinations of linker and ssDNA lengths were computed. Furthermore, the effect of three other parameters was explored: the excluded volume in the linker region, the excluded volume in the ssDNA region, and the DNA diameter. The linker excluded volume and the ssDNA excluded volume represent the volume in that region inaccessible to ions due to the steric repulsions. The ssDNA diameter affects the distribution of DNA charge and excluded volume. Increasing this parameter represents a transition from a more rigid structure where the ssDNA is immobilized in a cylinder to one where the average density is more spread out. The above 99 combinations of linker and ssDNA lengths were computed for each set of parameters listed below in **Error! Reference source not found.**. We found that results were not sensitive to these parameter choices for reasonable ranges. The subset of ion density calculations with a moderately low linker excluded volume of 1.3 nm^3, ssDNA excluded volume of 4.0 nm^3 and ssDNA diameter of 1.2 nm were used for comparison with the experimentally extracted cross term profile.

Linker excluded volume (nm^3)	ssDNA excluded volume (nm^3)	ssDNA diameter (nm)
0.0	0.0	1.2
1.3	4.0	1.2
1.3	4.0	2.4
1.3	4.0	3.6
1.3	4.0	4.8

5.0	4.0	1.2
9.0	4.0	1.2

Table A1.1: Sets of linker excluded volumes, ssDNA excluded volumes, and ssDNA diameters for which the above 99 combinations of linker and ssDNA lengths were calculated.

To quantify the agreement with the ASAXS experiments, the resonant intensities were calculated from the predicted cation densities. For each resonant intensity $I\ (q)$, the residual $r\ (q)$ was calculated by:

$$r(q) = \frac{I_{experiments}(q) - I_{simulation}(q)}{\sigma(q)} \tag{A1.16}$$

where $\sigma(q)$ is the standard deviation of the measured intensity at q. The individual residuals were then combined using a Huber loss function with tuning constant=1.345. The Huber loss function is more robust to outliers than the standard least squares measure. It reflects an assumption that points with high z-scores are indicative of data that is not normally distributed, and therefore assigns these points a higher probability than they would from a normal distribution. This prevents shifting the entire curve to fit a few outliers. An effective Huber χ^2 parameter was determined for each set of parameters (Linker and DNA lengths) by dividing the Huber loss function by the number of data points in the experimental curve. A lower limit of 8 nm was placed on the total length of the DNA shell based on the value obtained from a uniform core-shell model fit to the non-resonant ($\frac{N}{V}|F_0(q)|^2$) profile. The DNA shell length determined through a uniform core shell model is effectively a lower limit for the possible length of the DNA shell because the model assigns a uniform electron density to the DNA shell and does account for the $1/r^2$ drop off in the DNA and linker electron density due to their arrangement on a roughly spherical protein core. A contour plot of Huber χ^2 as a function of DNA and linker length is shown in Fig.A1.6 (A). The lowest value of Huber χ^2 (2.8) was obtained for the case of L = 4 nm and D = 4 nm. Within a confidence defined by $\chi^2 + 1$, total DNA shell lengths (L+D) ranging from 8 – 10.5 nm provide an acceptable match to the experimentally extracted cross term profile. The low resolution of ASAXS for the length of the DNA shell is expected since the cross term profile can be reliably extracted only over a limited range in q (up to 0.6 nm^{-1}). The DFT calculated Rb density profile for the case of the best fit parameters (L = 4 nm; D = 5nm) obtained from the core-shell model fit to the non-resonant profile results in a Huber $\chi^2 = 3.0$. Since this value of χ^2 lies within the $\chi^2 + 1$ confidence interval, the parameters L = 4 (± 0.5) nm and D = 5 (± 0.6) nm obtained from the non-resonant core-shell fit are deemed to reasonably describe the lengths of the linker and DNA segments. Huber χ^2 values corresponding to the DFT best match parameters (L = 4 nm and D = 4 nm) and the best fit parameters from the core-shell model fit (L= 4 nm and D = 5 nm) to the non-resonant profile are depicted by the pink and black markers in Fig. A1.6 (A). Fig. A1.6 (B) demonstrates that the experimentally extracted cross term profile (blue) is described equally well by both parameter sets.

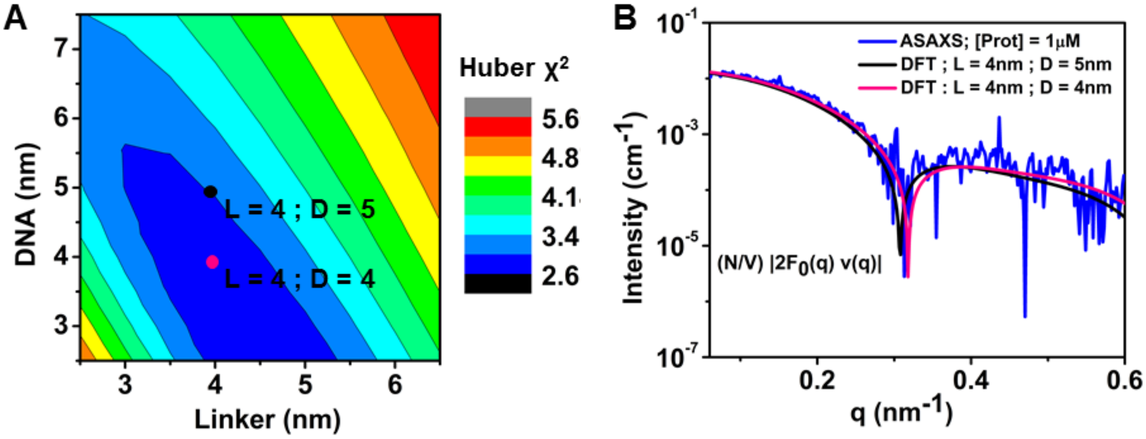

Figure A1.6: (A) 2D contour plot of χ^2 as a function of linker (*L*) and DNA (*D*) length. (B) Comparison of $I_{ASAXS}(q)$ (blue) to simulated DFT $I_{DFT}(q)$ profiles for the case of *L* = 4 nm; *D* = 5 nm (black) and *L* = 4 nm; *D* = 4 nm (pink).

A2. Supporting Information for Chapter 4

A2.1. SAXS on pure DNase I

SAXS Intensity profiles were collected from pure DNase I dispersed in the enzyme buffer to a final concentration of 0.005 mg/ml (166 nM). The resultant solvent subtracted intensity profile is depicted in Fig. A2.1(A). At the highest concentration of DNase employed in this study (166 nM), the SAXS profile of DNase does not show any appreciable structural features over the q-range of interest (0.07 – 1.2 nm^{-1}). Fig. A2.1(B) shows a comparison of the SAXS intensity profiles collected from pure water, reaction buffer and DNase I suspended in the reaction buffer corrected for scattering from the empty capillary. The presence of DNase has the effect of adding a finite intensity background to the scattering from the buffer. Thus, in order to ensure appropriate background subtraction, the SAXS profile collected from DNase I dispersed in the reaction buffer were used for solvent subtraction for the SAXS profiles from the ProSNA-DNase I system (Fig. 4.1(B), Fig. 4.2(A)).

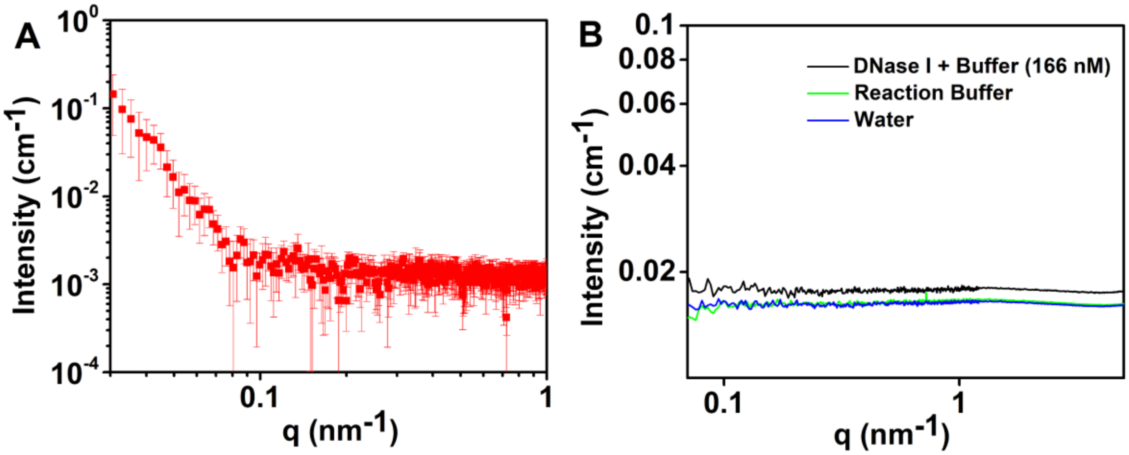

Figure A2.1: (A) Solvent subtracted SAXS Intensity Profile from DNase I (166 nM) (B) SAXS Intensity profiles from pure water (blue), reaction buffer (green) and 166 nM DNase I dispersed in the reaction buffer (black). These profiles were corrected for scattering from the empty capillary and demonstrate that the scattering from DNase I is negligibly small (8% higher than scattering from water).

A2.2. Effect of DNase I on native Catalase

While single stranded DNA, double stranded DNA and RNA are all known to be substrates for DNase I, the enzyme has not been reported to chemically modify or denature the native structure of Catalase. To verify that DNase I does not have any effect on the Catalase core of a Pro-SNA, we incubated 4 μM native Catalase with 166 nM DNase I at room temperature for 2 hours after which a SAXS profile was collected from the Catalase-DNase I sample. The solvent subtracted SAXS intensity profiles from native Catalase before and after incubation with DNase I are identical and are seen to overlay with each other. This confirms that DNase I does not chemically alter or destabilize the native conformation of Catalase and that the observed changes to SAXS intensity profile of the Pro-SNA upon incubation with DNase I occur due to a degradation of the DNA shell.

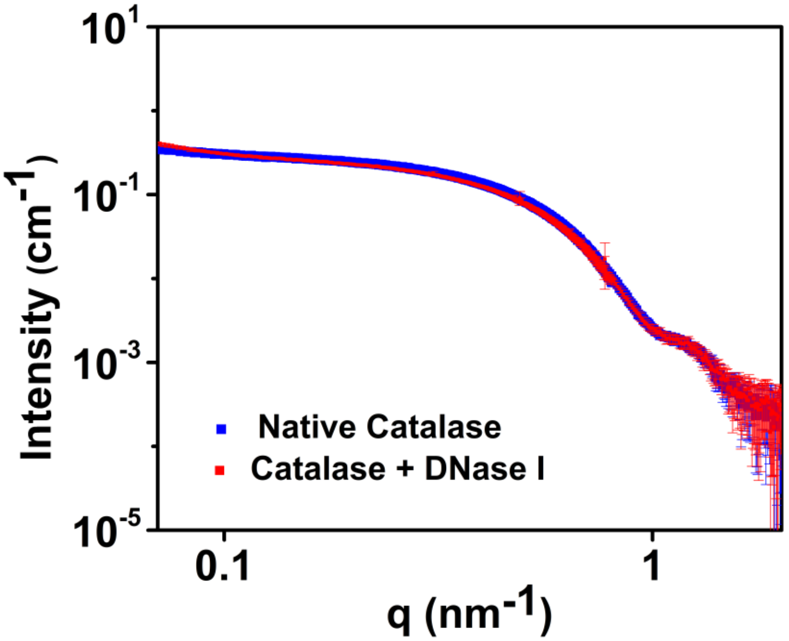

Figure A2.2: Background subtracted SAXS profiles from Native Catalase before (blue) and after (red) incubation with DNase I showing no appreciable changes

A2.3. Pair Density Distribution Function Analysis

Pair Density Distribution Function (PDDF) analysis is a useful model-independent tool which may be applied to Small Angle X-ray Scattering data from systems of dilute, non-interacting macromolecules to derive intuitive insight into particle dimensions. The pair density distribution function, P(r), is the distribution of distances between all pairs of points within the particle weighted by their respective electron densities. The P(r) function may be determined through a direct Fourier transform of the scattered intensity profile, I(q), as follows:

$$P(r) = \frac{r}{2\pi^2}\int_0^\infty qI(q)\sin(qr)dq \tag{A2.1}$$

The P(r) function is smooth and non-negative and approaches zero at the maximum dimension of the particle. It can therefore be used to determine the maximum diameter of the particle, referred to as D_{max}. In this study, we use PDDF analysis to determine the variation in the maximum diameter (D_{max}) of the Pro-SNA upon enzymatic degradation by DNase I. The P(r) function for the bare protein and Pro-SNA in States A and B were computed using GNOM program of the ATSAS software suite which calculates an indirect transform of user supplied small-angle scattering data. This program also enabled a determination of the maximum diameter (D_{max}) of the samples. The maximum diameter of the native Catalase determined through this method is 12.8 nm while those for the Pro-SNA in State A and B were determined to be 27.7 nm and 16.7 nm respectively. This

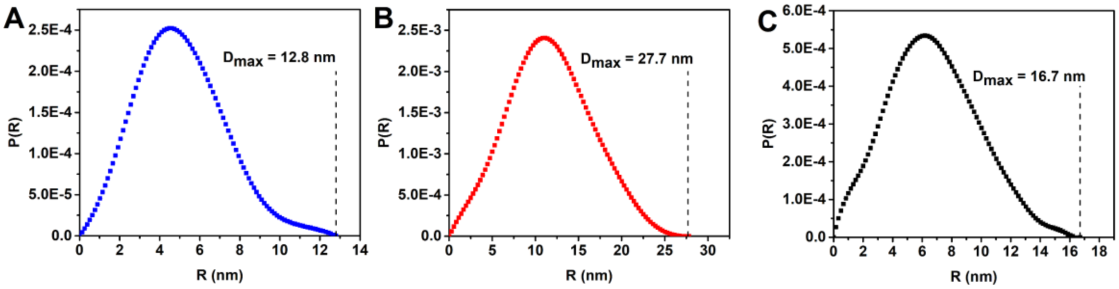

Figure A2.3: Pair Density Distribution Functions calculated for native Catalase (blue), Pro-SNA in State A (red) and Pro-SNA in State B (black). The decrease in the maximum diameter (D_{max}) of the Pro-SNA is consistent with a complete digestion of the DNA segment of the shell by DNase I.

suggests that the length of the shell on the Pro-SNA reduced from 7.4 nm to 1.9 nm indicating that ~ 6 nm of the DNA was digested by the DNase I. This is consistent with a complete hydrolysis of the 20 bp dsDNA segment of the shell by DNase I. The resultant Pro-SNA in State B is thus expected to have only linker segments attached to its surface.

A2.4. The Two-State Model: Linear Combination Fitting

The two-state model presented in the text implies that the measured SAXS intensity from the Pro-SNA-DNase I system sampled at any intermediate reaction timepoint may be expressed as a linear superposition of the SAXS intensities measured from the system in State A (intact Pro-SNA) and State B (degraded Pro-SNA):

$$I(q) = \alpha I_A(q) + \beta I_B(q) \tag{A2.2}$$

Here α and β represent the fraction of Pro-SNAs in State A and State B respectively such that the total number of Pro-SNAs in the system remains conserved ($\alpha + \beta = 1$). $I_A(q)$ is the measured SAXS intensity from the Pro-SNA before the addition of DNase I. For the Pro-SNA degradation reaction depicted in Fig. 4.2(A), this corresponds to the SAXS profile at the "0 minute" timepoint (black curve). The SAXS intensity profile measured from the Pro-SNA-DNase I system at the end of the degradation reaction (Fig. 4.2(A), 6-hour timepoint curve) is taken to be the intensity in State B, $I_B(q)$. The measured intensity profiles at intermediate timepoints are then fit to Eq. A2.2 above to determine the values of α and β. Nonlinear least squares curve fitting was used to determine optimal values of α and β through a minimization of χ^2. The linear combination fit for 4 representative intermediate timepoints is shown in Fig.A2.4. The values of α and β obtained as a result of this linear fit procedure are summarized in Table A2.1. It should be mentioned here that a summation at the level of intensity in Eq. A2.2 is justified since the solution of Pro-SNAs is dilute and there are assumed to be no interparticle interactions.

Reaction time point	Fraction in State A (α)	Fraction in State B (β)
5 min	0.71	0.29
16 min	0.53	0.47
27 min	0.35	0.65
42 min	0.24	0.76
54 min	0.21	0.79
1.5 hrs.	0.09	0.91
2.5 hrs.	0.03	0.97

Table A2.2: Fraction of Pro-SNAs in State A (α) and State B (β) as a function of time.

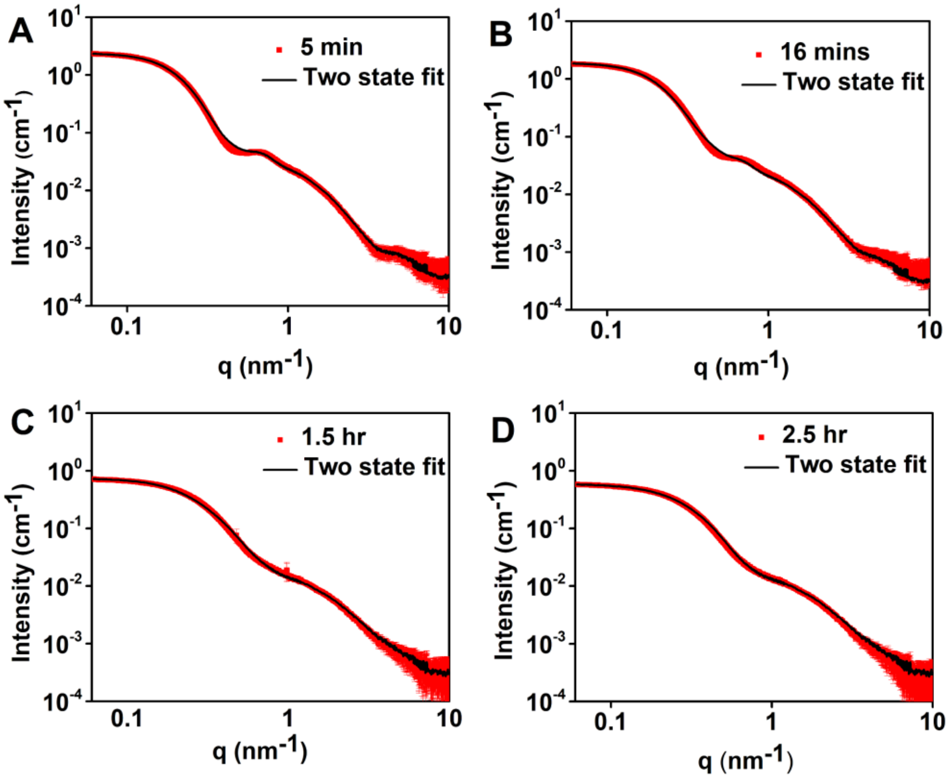

Figure A2.4: Examples of SAXS profiles measured from the Pro-SNA-DNase I system at 4 intermediate time points: 5 minutes (A), 16 minutes (B), 1.5 hours (C) and 2.5 hours (D) fitted with Eq.A2.2.

A2. 5. Lineweaver-Burk Analysis

The classical Michaelis-Menten equation used to describe enzyme-substrate kinetics is given by Eq. 4.5, reproduced below:

$$v_0 = \frac{V_m S}{S + K_m}$$

Here, v_0 is the initial rate of the overall reaction and S is the concentration of the substrate, which in our case is the DNA shell on the Pro-SNA. The quantities V_m and K_m are referred to as the maximal velocity of the reaction and the Michaelis constant and are related to the rate constants describing the reaction depicted in Eq. 4.4 by Eqs. 4.6-4.7. Since it is difficult to precisely determine the kinetic parameters V_m and K_m from a direct plot of v_0 vs. [S], the Michaelis-Menten equation is typically cast into a linear transformation. The most commonly used of these is called the Lineweaver-Burk plot. The Lineweaver – Burk equation is obtained by taking the inverse of the Michaelis-Mention relation above:

$$\frac{1}{v_0} = \frac{1}{S}\frac{K_m}{V_m} + \frac{1}{V_m} \tag{A2.3}$$

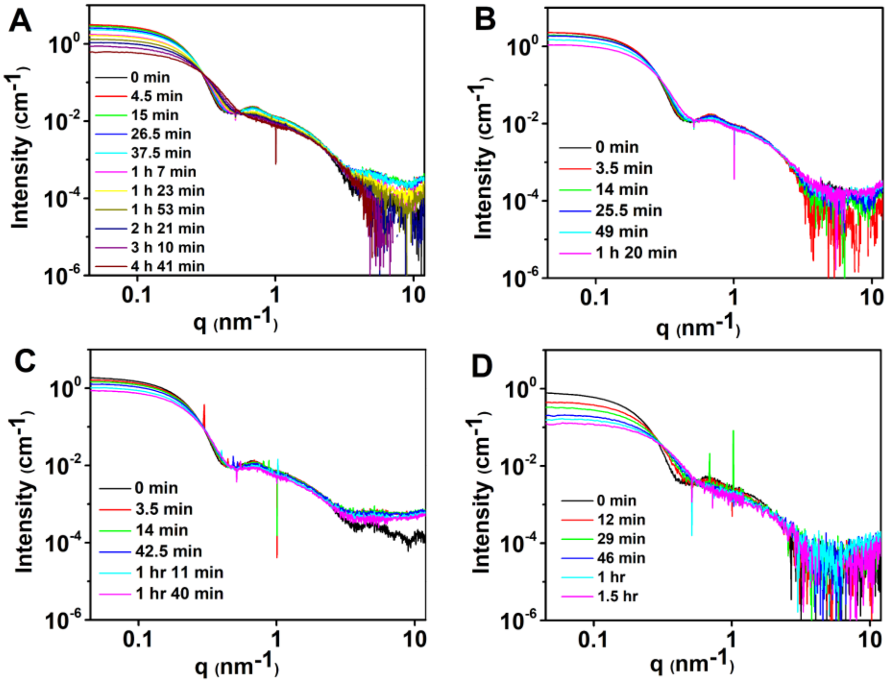

Figure A2.5: Background subtracted SAXS Intensity profiles from Pro-SNA-DNase I systems as a function of reaction time for 2 µM Pro-SNA (A), 1.5 µM Pro-SNA (B), 1.0 µM Pro-SNA (C) and 0.5 µM Pro-SNA at a fixed DNase I concentration (43 nM).

Thus, a plot of $\frac{1}{v_0}$ vs. $\frac{1}{S}$ can be used to extract V_m and K_m from the intercept and slope. An example of such a Lineweaver-Burk plot for our system is depicted in Fig. 4.4(B). The initial rate of the reaction v_0 for each of the Pro-SNA concentrations probed was determined from slope of the best fit line to decrease in the forward scattered intensity at initial time points (For instance, Fig. 4.4(A) and inset). The measured SAXS intensity profiles from Pro-SNA-DNase I systems for the different Pro-SNA concentrations probed are depicted in Fig. A2.5. The concentration of DNase I used in these reactions is kept constant at 43 nM. The isosbestic points exhibited by these sets of SAXS profiles are seen to occur at identical values of q (0.32 nm^{-1}, 0.54 nm^{-1} and 2.2 nm^{-1}) suggesting similar reaction pathways.

A2.6. Fluorescence Assay: Stability of Pro-SNAs vs. linear DNA against enzymatic degradation

DNA functionalized onto the surface of a Au nanoparticle core (a spherical nucleic acid or SNA) has been shown to exhibit a greater resistance to enzymatic degradation by DNase I in comparison to linear free DNA. In order to determine whether DNA functionalized onto the surface of a protein (Pro-SNA) also demonstrates an enhanced stability, a fluorescence based spectroscopic assay was performed. Briefly, the 3’ terminus of a 5’ DBCO modified oligonucleotide was labelled with a Cyanine 3 (Cy3) fluorescent dye (Sequence: 5’-DBCO dT CCCAGCCTTCCAGCTCCTTG Cy3-3’). This DBCO modified DNA strand was then functionalized onto the surface of a Cg Catalase protein using previously described methods (See Materials and Methods). A duplexer strand labelled with a BHQ2 quencher was then hybridized to the DBCO DNA on the protein surface (Sequence: 5’- BHQ2 CAAGGACTGGAAGGCTGGG-3’). In this duplexed state, the fluorescence intensity emitted from the Cy3 (Excitation: 547 nm, Emission: 563 nm) is quenched by BHQ2(Absorption: 560 – 670 nm). In order to facilitate a comparison with an analogous molecular (free) DNA system, a Cy3 labelled oligonucleotide duplexed with a BHQ2 labelled strand was used. The DNA sequences employed in the Pro-SNA and molecular system are identical. The dye-labelled Pro-SNA was suspended in the DNase I reaction buffer to a final concentration of 25 nM such that the concentration of the DBCO-Cy3 DNA on the protein surface was approximately 1000 nM. The concentration of the DBCO-Cy3 DNA on the surface of the protein was determined using UV-Vis absorption spectroscopy and the known molar extinction coefficient of the DNA. The free molecular DNA described above was also dispersed in the reaction buffer such that the final concentration of the duplex in solution was 1000 nM (equivalent to DNA concentration in Pro-SNA system). 100 µl samples of the Pro-SNA and molecular system were then placed in a 96-well fluorescence microplate at 37°C and allowed to equilibrate for 10 minutes. DNase I was then added to the samples at a concentration of nM. The fluorescence of the sample was then measured at 563 nm every 74 seconds for 12 hours. The results of this measurement are shown in Fig. A2.6. The fluorescence intensity measured from the Pro-SNA system is observed to be lower than that from the molecular system. Further, the rate of increase in the fluorescence intensity from the molecular system is greater than that for the Pro-SNA system indicative of a higher initial reaction velocity. These results suggest that the rate at which the fluorophore-labelled DNA is degraded by DNase I is greater when the DNA are free in solution compared to when they are attached onto the surface of a protein. Thus, similar to Au nanoparticle

SNAs, Protein SNAs exhibit an enhanced resistance to enzymatic resistance by DNase I in comparison to linear free DNA.

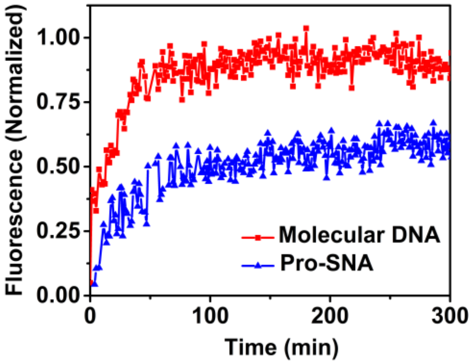

Figure A2.6: Fluorescence Intensity measured from Pro-SNA (blue) and molecular DNA (red) system as a function of time corrected for background fluorescence from reaction buffer.

A2.7. MALDI Mass Spectrometry of reaction product

In order to identify the products of the enzymatic degradation of the DNA shell on a Pro-SNA by DNase I, we used MALDI Spectrometry. Pro-SNA (4 µM) was incubated with DNase I (332 nM) for 2 hours at room temperature. The degraded DNA products were isolated from the Pro-SNA and DNase I by ultracentrifugation using Amicon Ultra 30 kDa spin filters. The run-off was collected, mixed with 2',4'- DHAP MALDI matrix and plated on a MALDI plate. The sample was then analyzed using MALDI-TOF mass spectrometry on a Bruker AutoFlex spectrometer. The resultant mass spectrum, depicted in Fig. A2.7, displays a dominant peak corresponding to a molecular mass of 594 Da. This is roughly equivalent to the mass of two DNA bases (such as CT = 593 Da) and is thus consistent with formation of dinucleotides. Along with additional peaks present at lower values, the observed spectrum suggests that the DNase I degradation reaction results in the production of mono and di-nucleotide fragments.

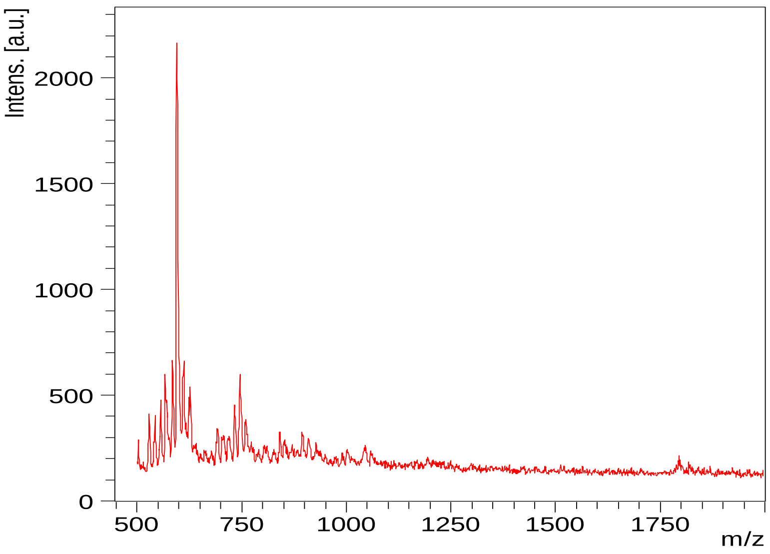

Figure A2.7: MALDI Mass spectrum collected from the DNA products of the enzymatic degradation reaction isolated from reaction mixture.

A3. Supporting Information for Chapter 5

A3.1. Extraction of f'(E) for Rb^+ and Sr^{2+}

The K-edges of Rubidium (15.2 keV) and Strontium (16.1 keV) were calibrated using a transmission scan collected from 1M solutions of pure Rubidium Chloride and Strontium Chloride respectively (Fig. A3.1 (A)-(B)). The transmitted intensities were collected over a 100 eV range around the expected values of the K-edges. The positions of the Rb^+ and Sr^{2+} K-edges were determined to be approximately keV and keV respectively. The slight deviations from the theoretical edges are due to the resolution of the monochromator. The values of the anomalous dispersion corrections for Rb^+ and Sr^{2+}, f'(E) and f''(E), were determined using the Optical Theorem and the Kramers-Kronig relations implemented using the script CHOOCH. CHOOCH

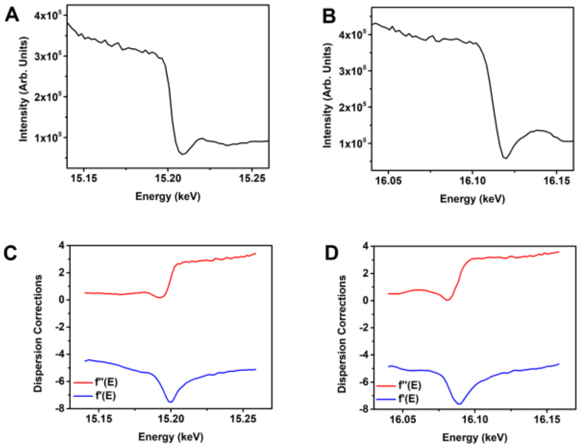

Figure A3.1: (A) Transmitted Intensity as a function of incident x-ray energy in the vicinity of the Rb and (B) Sr K-edges. (C) Extracted dispersion corrections f'(E) and f''(E) for Rb+ and (B) Sr2+ around their K-absorption edges.

numerically evaluates f'(E) and f''(E) for a given element using user supplied transmission or fluorescence energy scans. Extracted f'(E) and f''(E) values for Rb^+ and Sr^{2+} are shown in Figs A3.1 (C) and (D).

A3.2. Extracted Non-Resonant and Resonant Cross Terms

The Non-Resonant and Resonant cross terms in Eq. are extracted from the SAXS intensity profiles collected below the Rb^+ and Sr^{2+} K-edges for each of the buffers (A) – (D) described in the text. The procedure to isolate these terms was identical to that described in the text for the case of Pro-SNA dispersed in 50 mM RbCl. The SAXS intensity profiles and the extracted non-resonant and

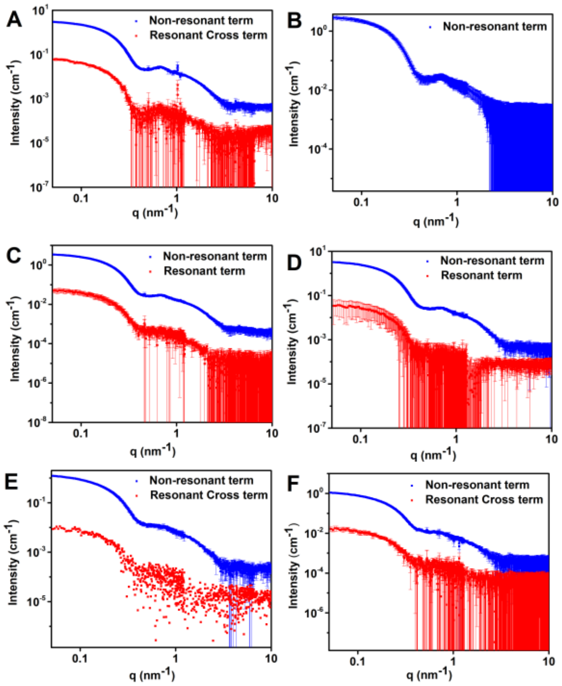

Figure A3.2: Extracted Non-resonant and Resonant Cross term profiles from Pro-SNA dispersed in Buffer B (A&B), Buffer C (C&D) and Buffer D (E&F) from profiles measured below the Rb K-edge (A, C &E) and Sr K-edge (B, D & F).

resonant cross term profiles for Rb^+ and Sr^{2+} are shown in Fig A3.2 (A) – (F). Note that the resonant cross term from 5mM $SrCl_2$ is not shown due to the large degree of experimental uncertainty.

A3.3 Extracted $v(q)$ as a function of $SrCl_2$ concentration.

We extracted the term $v(q)$ using the measured non-resonant and resonant intensity profiles from Rb^+. The term $v(q)$, is also seen to an exhibit an increase in the position of the first minima with increasing $SrCl_2$ concentration (Fig. A3.3) which suggests a reduction in the radial extent of the Rb^+ counterionic cloud. This verifies that the changes in the form of the resonant cross term from Rb^+ $\left(\left(2F_0(q)v(q)\right)\right)$, (Fig 5.3(B)) are not solely due to the changes in the non-resonant factor $F_0(q)$.

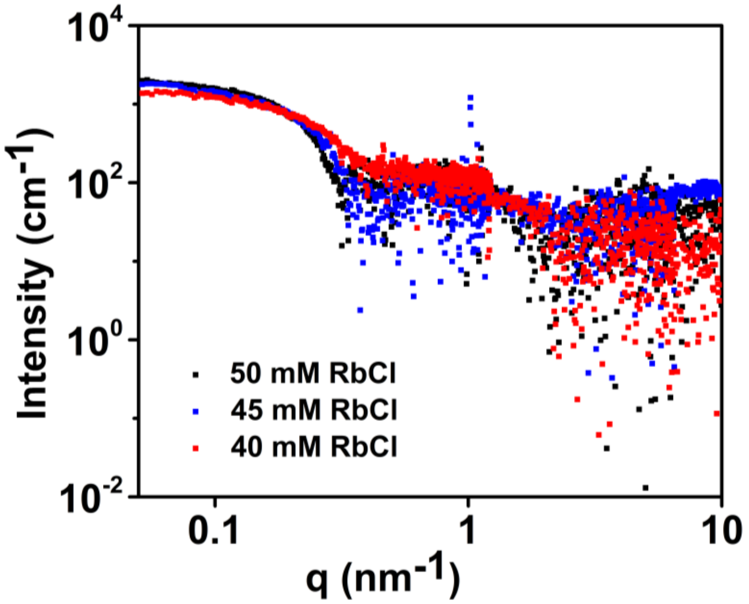

Figure A3.4: Fourier transform of the excess Rb^+ density distribution surrounding a Pro-SNA as a function of $SrCl_2$ concentration.

A4. The Synthesis of Pro-SNAs for X-ray Scattering Measurements

The purpose of this appendix is to provide an overview of the protocols and procedures involved in the synthesis of Protein Spherical Nucleic Acid (SNA) conjugates. This appendix is divided into two parts: the first describes the synthesis of the oligonucleotides required for Protein SNAs, while the second discusses the functionalization procedure for Protein SNAs.

A4.1 Synthesis, Purification and Characterization of DNA

A4.1.1 Solid Phase Oligonucleotide synthesis

The synthesis of Spherical Nucleic Acid conjugates (Au nanoparticle and protein cores) typically begins with the synthesis of the oligonucleotides required for particle functionalization. Oligonucleotide synthesis is carried out using standard DNA phosphoramidite chemistry on solid-phase supports using an automated DNA synthesizer such as an ABI 392/394 or MerMade 12 (MM12). The solid-phase supports used for DNA synthesis are typically controlled pore glass (CPG) beads which are rigid, insoluble particles with pore sizes between 500 – 2000 A to which the oligonucleotide is bound during synthesis. Phosphoramidite DNA synthesis proceeds in the 3' to 5' direction, opposite to the 5' to 3' direction observed in the biosynthesis of DNA. In this section, the steps in the phosphoramidite method will be briefly discussed. A more detailed

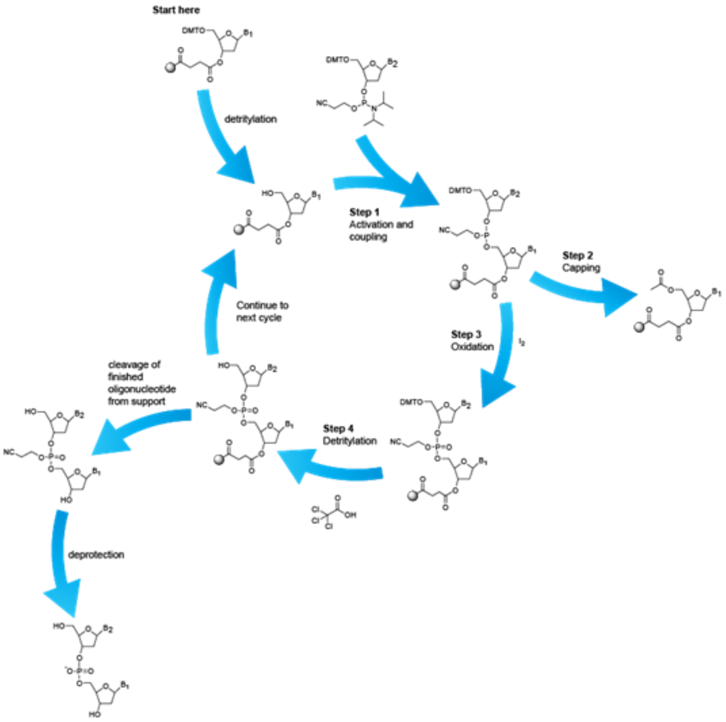

Figure A4.1: The phosphoramidite DNA synthesis cycle

description can be found at: https://www.atdbio.com/nucleic-acids-book. Figure A4.1 below depicts the typical steps in a DNA synthesis cycle.

The steps in the cycle are:

1. Detritylation: The nucleoside bound to the CPG is protected by a 5’-DMT (4,4’-dimethoxytrityl) to prevent polymerization during resin functionalization. In the detritylation step, the DMT group is removed by TCA (Trichloroacetic Acid) in DCM (dichloromethane) which results in the production of the orange-colored DMT carbocation. The DMT carbocation absorbs at 495 nm which can be used to monitor coupling efficiency.

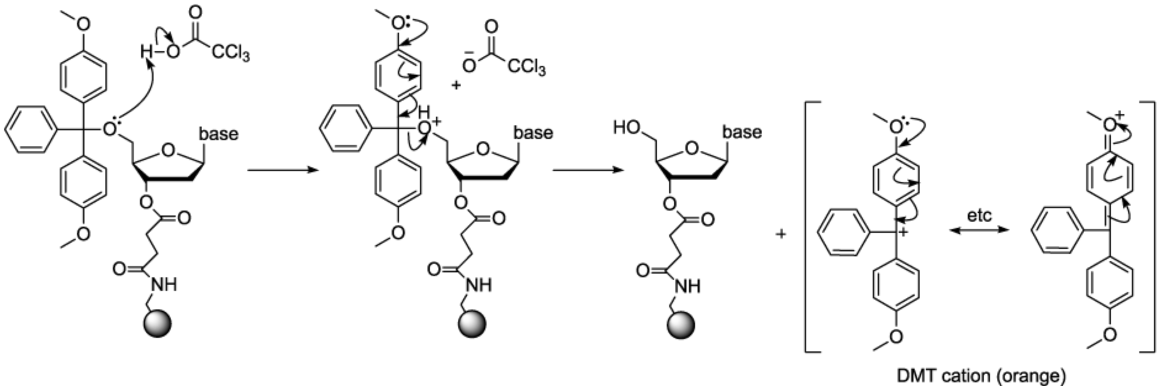

Figure A4.2: Phosphoramidite nucleoside detritylation

2. Coupling: The free 5’-OH group on the CPG-bound nucleoside is then reacted with the next nucleoside which is supplied as a phosphoramidite monomer. Prior to this, diisopropylamino group on the incoming monomer is “activated” (protonated) by ETT (5-(ethylthio)-1H-tetrazole). This activated phosphoramidite is then supplied in a many-fold excess to drive the reaction to completion.

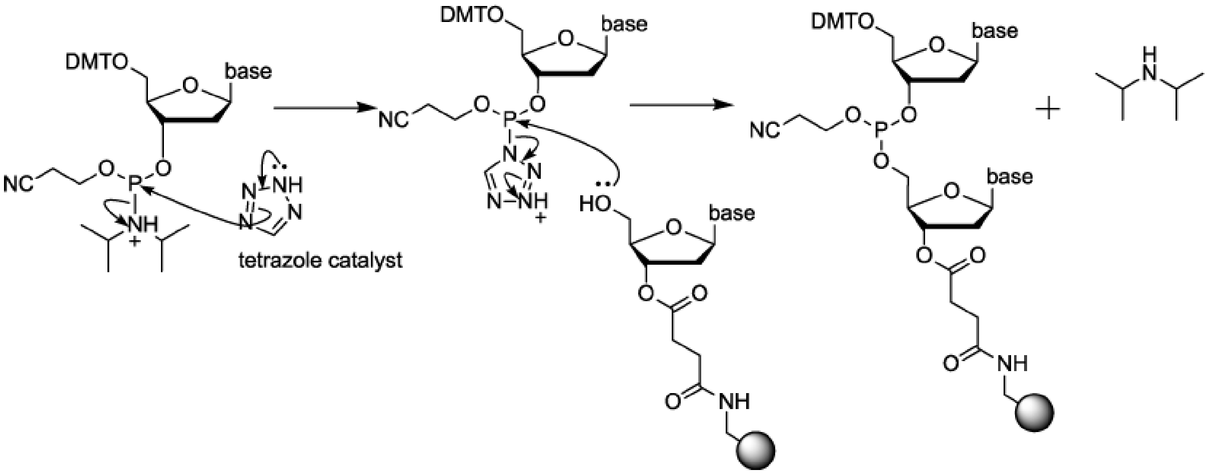

Figure A4.3: Phosphoramidite coupling

3. Capping: In order to prevent the unreacted 5’-hydroxyl groups on the CPG-bound nucleotide from reacting with the next incoming phosphoramidite, they are acetylated through the addition of

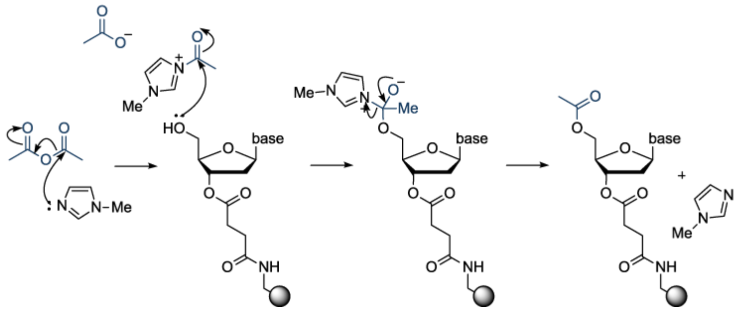

Figure A4.4: Phosphoramidite capping

two capping agents: Acetic anhydride and *N*-methylimidazole (NMI). This electrophilic mixture rapidly acetylates alcohols and renders them inert to subsequent reactions.

4. Oxidation: The phosphate triester (P(III)) is unstable and must be converted into a stable species (P(V)) prior to the start of the next cycle. This is achieved by oxidation of the triester by a mixture of Iodine, water and pyridine. The resultant phosphotriester is a standard DNA backbone protected by a β-cyanoethyl protecting group.

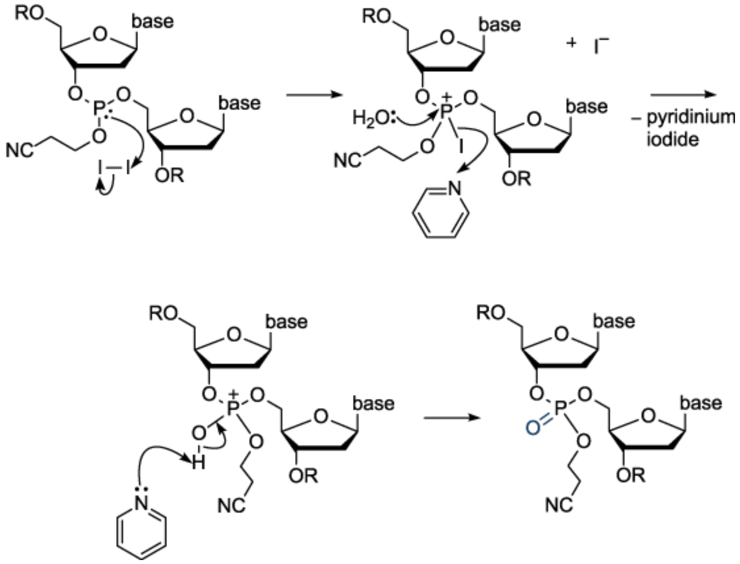

Figure A4.5: Oxidation

5. Detritylation: The DMT protecting group at the 5’ end of the DNA chain on the CPG is then removed using TCA in DCM so that the primary hydroxyl group can react with the next incoming phosphoramidite. These steps are then repeated to obtain the desired oligonucleotide.

Next, we describe the protocol used to synthesize DNA and the subsequent processing and purification steps required before the DNA are ready for particle functionalization. The protocol described below pertains to the synthesis of DNA on the ABI 392/394 synthesizer. In order to reserve time on the ABI, input your name and sequences into the ABI synthesis spreadsheet. Make sure to plan ahead and input your sequences a few days before your planned synthesis start date. Access to the ABI spreadsheet will be granted upon being trained on the instrument. The ABI 392 synthesizer is well suited for large scale (10 µM) DNA synthesis and for those requiring specialty phosphoramidites such as DBCO dT or dyes such as Cy3/Cy5. All the DNA used in this work were synthesized on an ABI 392 synthesizer and were processed using the following protocol:

1. Packing the columns: To begin, the starting CPG reagent must be weighed out and packed into a twist-type DNA synthesis column. We typically use universal CPG supports (Chemgene, Universal UnyLinker support 1000 A, Cat.no. N-4000-10) for the DNA for protein functionalization which do not have a pre-attached nucleoside. This allows for their use in synthesis with any (A,T,C,G) phosphoramidite at the 3' end. The scale of the DNA synthesis refers to the quantity of starting reagent (in this case CPG). For a given synthesis scale, the appropriate quantity of CPG required may be estimated by using the µmol/g conversion provided on the bottle

Figure A4.6: Universal UnyLink Supports

(See image below). For a 10 µM scale synthesis, this corresponds to approximately 251 mg of universal CPG. To synthesize DNA for AuNP functionalization, thiolated CPGs need to be used

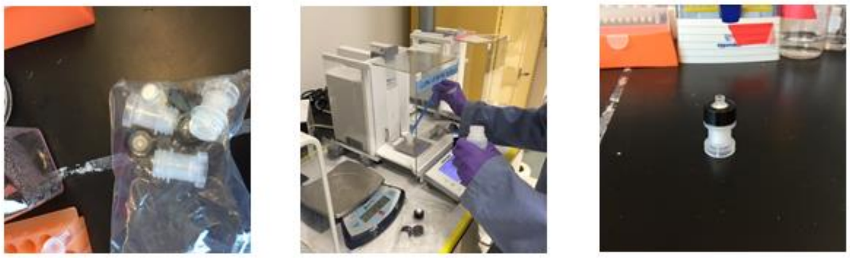

Figure A4.7: (Left) Parts of a twist type DNA column. (Center) Weighing out the CPGs (Right) Packed column

(3'-Thiol-Modifier C3 S-S CPG, Glen Research Cat no. 20-2933-01). These CPGs then need to weighed out and put into an ABI twist type DNA synthesis column. These columns consist of three parts (see figure below): a column, a top fret and a black twist cap. Upon placing the weighed-out CPS into the column and covering with the top fret, a small spatula and N2 gun may be used to ensure that there are no CPGs stuck to the top rim of the column. The top fret must then be pressed onto the column tightly using a small mallet or the bottom of a glass bottle to ensure that it is tightly sealed and that there are no leaks. The black twist cap may be then be twisted onto the column.

2. Preparing the reagents: The reagents required for DNA synthesis include the phosphoramidites, activator, Capping agents (Cap A & Cap B), Oxidizer, deblocking agent and anhydrous ACN. These reagents are pre-mounted on the ABI synthesizer. Prior to the start of synthesis, input the number of bases in your sequences into the ABI synthesis spreadsheet “Reagent Calculator”. A

snapshot of this spreadsheet is provided below. The reagent calculator predicts the amount of each reagent required for your synthesis (See Total Vol (mL) for 10 umol scale column).

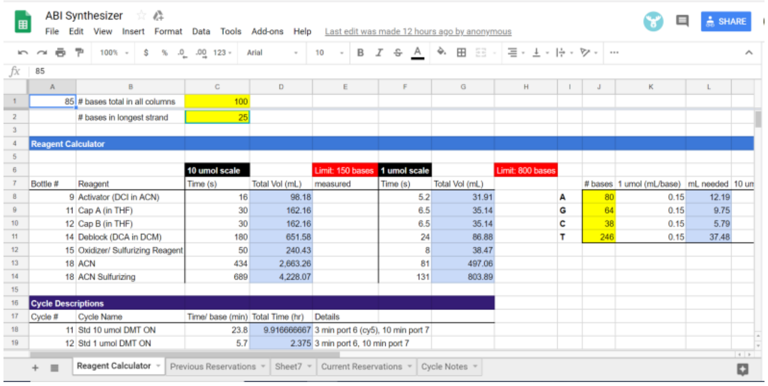

	A	B	C	D	E	F	G	H	I	J	K	L	
1	85	# bases total in all columns	100										
2		# bases in longest strand	25										
3													
4	Reagent Calculator												
5													
6			10 umol scale		Limit: 150 bases	1 umol scale		Limit: 800 bases					
7	Bottle #	Reagent	Time (s)	Total Vol (mL)	measured	Time (s)	Total Vol (mL)			# bases	1 umol (mL/base)	mL needed	10 um
8	9	Activator (DCI in ACN)	16	98.18		5.2	31.91		A	80	0.15	12.19	
9	11	Cap A (in THF)	30	162.16		6.5	35.14		G	64	0.15	9.75	
10	12	Cap B (in THF)	30	162.16		6.5	35.14		C	38	0.15	5.79	
11	14	Deblock (DCA in DCM)	180	651.58		24	86.88		T	246	0.15	37.48	
12	15	Oxidizer/ Sulfurizing Reagent	50	240.43		8	38.47						
13	18	ACN	434	2,663.26		81	497.06						
14	18	ACN Sulfurizing	689	4,228.07		131	803.89						
15													
16	Cycle Descriptions												
17	Cycle #	Cycle Name	Time/ base (min)	Total Time (hr)	Details								
18	11	Std 10 umol DMT ON	23.8	9.916666667	3 min port 6 (cy5), 10 min port 7								
19	12	Std 1 umol DMT ON	5.7	2.375	3 min port 6, 10 min port 7								

Figure A4.8: ABI synthesis spreadsheet showing the reagent calculator

Check the quantities of phosphoramidites already on the synthesizer – if these are insufficient for your synthesis run, prepare fresh A, T, C and G phosphoramidites. A 0.1 M solution of these phosphoramidites maybe be prepared by adding the following quantities of anhydrous ACN to 2g packs of the phosphoramidites:

(i) dA-CE phosphoramidite (Cat no. 10-1000-20): 24 mL

(ii) dT-CE phosphoramidite (Cat no. 10-1030-20): 27 mL

(iii) Ac-dC-CE phosphoramidite (Cat no.10-1015-20): 26 mL

(iv) dmf-dG-CE phosphoramidite (Cat no. 10-1029-20): 24 mL

If Spacer 18 (Hexaethylene glycol spacer) is required, dissolve a 100 mg pack of Spacer 18 (ChemGenes, Cat no. CLP-9765) in 6 mL of anhydrous ACN. If any other specialty phosphoramidites are required (For e.g. DBCO dT), the appropriate amount of ACN/solvent required to dissolve a given pack size can be found on the respective Glen Research product page.

For example, DBCO dT requires 1.0 mL Trimer diluent (Anhydrous Acetonitrile/Dichloromethane 1:3 (v/v)) for a 100 µmole pack size (Cat. no. 10-1539-90, see page: http://www.glenresearch.com/data/ProductInfo.php?item=10-1539). The product page also contains useful information regarding the coupling, oxidation and deprotection conditions required for the phosphoramidite. The ACN is stored in dry N_2 to prevent contamination by water, and thus must be taken out using a Schlenk line set up (See figure below). Once the ACN is added, the phosphoramidites may be vortexed and sonicated for 30s to ensure that they are dissolved.

Figure A4.9: Diluting the phosphoramidites: (Left) The N_2 supply valve for the Schlenk line (Center) Drawing out Anhydrous ACN by piercing septum with long needle (Right) Adding ACN to the vented phosphoramidite bottles.

3. Setting up the synthesis: Once the phosphoramidites are prepared they can be loaded onto the ABI synthesizer. On the main display of the ABI synthesizer chose Main Menu > Next Page > Change Bottle. Type in the bottle number – the phosphoramidites are labeled 1- 8, while the remainder of the reagents are labelled 9 – 18. Hit Start. The instrument will then rinse and flush the line to the bottle with Argon. When this cycle is complete and the instruction to replace the

bottle appears, physically remove the bottle – the phosphoramidites may be removed by pushing down on the black button and pulling the bottle out while the reagent bottle may be twisted off. Top off the phosphoramidites and reagent bottles using the freshly prepared phosphoramidites and reagent stock bottles provided in the hood/below the hood next to the ABI synthesizer. The phosphoramidite bottles can be replaced by pushing down on the black button, inserting the bottle into the slot and then releasing the button. The reagent bottles need to be twisted back on until a click sound is heard. Old/waste bottles need to be rinsed with Acetone and disposed of in the broken glass waste bin. Phosphoramidites (A, C, G and T) are housed in ports 1-4, while ports 5-8 are used for specialty amidites. For instance, Spacer 18 is generally put on port 5 while DBCO dT is generally loaded on port 8. Note that when the quantity of amidite is < 2 mL, it is advisable to put it into a small glass tube before putting into the brown amidite bottle so as to ensure that all the liquid is taken up by the tubing. Once the bottle has been replaced, press resume. Repeat this process for all the amidites and reagents. Ensure that the waste bucket is not full, empty it if it is before starting synthesis. Check the levels on the Argon tank - Left gauge should be at ~ 40; right gauge not lower than 200 psi. Put columns onto synthesizer – remove the dummy fret and replace with column.

4. Inputting the sequences: Once the bottles have been changed etc., do not touch the synthesizer and now start the Oligonet Program on the computer. Choose Function > Edit sequence. Input the required sequences from 5'>3' end, Name the sequence and to save choose File > send to synthesizer. Note that the ABI synthesizer assumes that CPGs with the first 3' base are loaded onto the synthesizer, thus it skips this base during synthesis. To prevent this always type a dummy base at the 3' end of your sequence. While inputting your sequence, note that the phosphoramidites are referenced using capital letters – A, C, G, T while the specialty amidites are referenced using the number of the port they have been loaded on, for example: 5' -55GTCT-3' will put two Spacer 18 groups on the 5' end and skip the first T on the 3' end. To save your sequence, chose file > send to synthesizer.

Figure A4.10: (Left) Phosphoramidite bottles loaded onto synthesizer using the black tab buttons. (Right) CPG filled columns affixed onto the synthesizer – reagents flow into the column from the bottom and come out through the tubing on the top.

5. Selecting cycle and setting up synthesis: For a standard 10 µmol scale synthesis, chose Function > Set up Synthesis and in the cycle drop down menu, chose: 10 um CE. This cycle performs regular coupling on all ports 1-8. Assign the cycles to the appropriate columns and select the correct sequence for each column. Check “DMT” on to leave a DMT group on the DNA at the final step. For standard DNA without any modifications, this allows purification of the DNA using HPLC by exploiting the hydrophobicity of the DMT group. Then chose File > send to synthesizer. When you are ready to begin the synthesis, chose Synthesizer > Prepare to start. On the synthesizer, press start. You may wait until the first detritylation step to visually check that the orange color due to leaving DMT carbocation is present.

6. Coupling DBCO: The DNA sequence for protein functionalization has a DBCO group on the 5’ end. This group is typically added onto the regular sequence prepared in the step above as a second synthesis because it requires a longer coupling time (12-15 minutes) and the use of a CSO oxidizer. Using the change bottle function, change out the Iodine oxidizer to the CSO oxidizer and place the diluted DBCO phosphoramidite on port 8. Since the volume of the DBCO is less than 2 mL place it into a small clear glass tube before placing it into the empty bottle. Remove the columns that contain sequences that do not need to be modified with DBCO. To couple the DBCO onto the DNA choose Function > edit sequence. Modify the sequence to 5’ – 8T – 3’. Here 8 refers to the port on which the DBCO was mounted and T is a dummy base. Then choose Function > Set up synthesis. Choose the cycle (10 um CE DBCO dT) and assign it to the appropriate column. Make sure that DMT is checked “off”. The DBCO group is sufficiently hydrophobic and thus the sequence does not require a DMT group at the 5’ end for purification. Save your work by choosing

Function > send to synthesizer. Start the synthesis by choosing Synthesizer > Prepare to start. Start the synthesis – the coupling will take approximately 30 minutes.

7. Cleaning the synthesizer: After synthesis, the ports that specialty amidites were used on need to be cleaned using MeCN. On the synthesizer panel: Main Menu > Next Page > Manual Control. The display will show Function (). Enter 77 in the parenthesis, this will flow ACN to port 8 (18 to 8). Let it flow for 20 s. Watch the timer on the synthesizer display panel. After 20 s abort the process and input function 13 [flush to 8 (with Ar)]. Repeat 3X. Remove the bottle wash the bottle and the test tube with acetone. Return the empty bottle to the drawer and trash the test tube. Put back the ACN bottle in port 8 and rinse with ACN (Function 77) and flush with Ar (Function 13). *Note the function menu is posted in a separate sheet next to the synthesizer.

Figure A4.11: The DBCO phosphoramidite pack (left) and diluent (center). (Right) DBCO placed in a small glass tube inside an empty bottle and mounted on port 8 and CSO oxidizer mounted on port 15.

Clean the amidite port with NH_4OH (Section 5 in the instruction sheet). On the synthesizer panel: Main Menu > Next Page > Manual Control. The display will show Function (). Enter 36 in the parenthesis, this will flow NH_4OH to ports 1-4. Abort the process when the collection vials are 1/4th full. Enter 5 to flush all ports with Ar. Repeat 3x. Note you can choose to rinse only the ports that you used 1-3 in the example case. Take out the collection vials, empty them, rinse with acetone and blow dry. Replace the vials to their original location on the synthesizer. Enter 42 for rinsing the tubing with ACN for 20s. Followed by 2 for flushing ports 1-4 with Ar for 10 s. Rinse the mixing block inside the synthesizer with ACN (64), followed by flushing with Ar (1) for 20 s.

A4.1.2. Deprotection

After synthesis, the DNA must be subjected to a deprotection step which serves to cleave the DNA from the solid CPG supports, remove the protecting groups on the nucleobases as well as the cyanoethyl protecting group on the DNA phosphate backbone. The deprotection is usually carried out with concentrated Ammonium Hydroxide (28 – 33%). Note that the Ammonium Hydroxide must be fresh (opened within the last two weeks). The rate limiting step in the deprotection is the removal of the protecting group on the G base. Based on the type of dG phosphoramidite used and the temperature, the time required for complete deprotection can be found on the Glen Research website : http://www.glenresearch.com/Technical/Deprotection.pdf. The steps in the deprotection protocol are as follows:

1. Twist off the black cap on the synthesized DNA column and using pliers very carefully twist off the top fret taking care to ensure that none of the CPG beads fall out. Dump the dried CPG beads into a 20 mL scintillation vial.
2. Add 5 mL of fresh Ammonium Hydroxide (30%) to the vial and vortex for 30 seconds.

3. Leave the vial overnight at room temperature for 17 hours, or at the temperature required for complete deprotection for the recommended time based on Table 1 in the Glen Research document (http://www.glenresearch.com/Technical/Deprotection.pdf). For the case of DBCO modified DNA, 17 hours at RT is recommended.

4. At the end of 17 hours, use the Multivap to evaporate the Ammonium Hydroxide from the DNA mixture:

(i) Turn on the N_2 flow and power on the instrument.

(ii) Make sure the black gas toggle is in the on position.

(ii) Replace the glass pipettes on the line you intend to use. Lift the gas manifold up by turning the black knobs on the side of the manifold and refastening them after the manifold moves up. Uncap the glass vials and place them in the vial holders on the instrument.

(iv) Carefully move the manifold back down and ensure that the pipettes are about 0.5 – 1 inch below the rim of the glass vials. Turn on the switch on the gas manifold line you plan to use.

(v) Adjust the gas flow using the black screw knob.

(vi) Take the vials off the Multivap in about 1-1.5 hours and ensure that no smell of Ammonia remains.

Figure A4.12: The Multivap Instrument

5. Wash the CPG beads with water thoroughly (3 times) and place the resultant mixture into a 15 mL conical tube. Centrifuge the tube to concentrate the CPGs and separate them from the liberated DNA present in the water (See figure below).

6. Syringe filter the resultant supernatant (containing the DNA) into a separate tube to remove any residual CPGs or impurities.

Figure A4.13: (Left) Centrifuged DNA-Water-CPG mixture showing separated CPGs at the bottom and DNA at the top. (Right) Syringe filtering the supernatant.

A4.1.3 Purification by HPLC

After cleavage from the solid support and deprotection, the success strands must be separated from the failure strands. In order to do this, we use Reverse-Phase High Performance Liquid Chromatography (RP-HPLC). HPLC separates molecules based on their hydrophobicity. In RP-HPLC, the molecules to be purified are in a mobile liquid phase which interacts with a stationary hydrophobic phase. The stationary phase is composed of a non-polar adsorbent such as silica which has been modified with straight-chain alkyl groups while the analyte is dissolved in a slightly polar mobile phase which is pumped through a column containing the stationary phase. The extent of interaction of the mobile analyte with the stationary phase determines the elution time of each component in the analyte mixture. Most standard oligos are synthesized with a hydrophobic DMT group at the 5' end – thus the success strands with the DMT group will have a stronger interaction with the column and elute at a later time, while the failure strands will elute at an earlier timepoint. For the case of DBCO modified DNA, the DBCO-dT is sufficiently hydrophobic and will elute at approximately the same time (~20 minutes) as a DMT-capped oligo. The protocol to purify DNA on the HPLC (Varian ProStar) is as follows:

1. Check that there is sufficient solvent for the column type and run time you are planning on using. The solvents (buffers) required for the HPLC are:

(i) Buffer A: 1880 mL of filtered Nanopure H_2O + 60 mL TEAA + 60 mL ACN.

(ii) Buffer B: 100 % ACN

2. Ensure that the waste bucket is not full.

3. Check that the correct column is connected for how much DNA you want to inject. The small columns (flow rate: 3 ml/min) can take DNA synthesized on a 5 µmol scale, while the big columns (flow rate : 15 ml/min) can take DNA synthesized on a 10 µmol scale. We typically use the big C18 type columns for the purification of DNA synthesized on the ABI.

4. Turn on the switches on the three HPLC units and launch the HPLC software. The top panel of the “System Control” software controls the pumps while the bottom panel controls the spectrometer.

5. On the bottom panel choose “Options” > “Lamp Operations” and check the boxes next to UV and Vis. Visually confirm that the lamps have come on.

6. To turn on the pumps, hit “Activate” in the top panel – you should be able to hear the pumps turning on and the solvent will start flowing through the line. This activates both pump A and pump B for buffers A and B respectively. Make sure that the pressure in pump A stays below 1300 psi.

7. To clean out the column, choose “Manual Control” and switch Buffer B to 98% with a ramp time of at least 5 minutes. Make sure the flow rate is appropriate for the type of column selected. Hit start ramp. Once the ramp is done, ramp back down to 2% Buffer B over 5 minutes.

8. While the column is being flushed, rinse the injection loop with about 15 mL of H_2O.

9. To run your sample, make sure that the correct method is selected. The methods are named as BC_DNA_75_45, which means that the system will ramp up to 75% Buffer B over 45 minutes. The exact pump program for the method can be viewed and modified using the method builder. For DBCO DNA select, “BC_DNA_75_45DBCO”. This method monitors the absorption wavelength of DBCO (310 nm) in addition to that of the DNA bases (254 nm).

10. Choose Inject > Inject single sample > Inject. With the injection loop still in the load position, physically inject your sample into the loop. The maximum sample volume per injection is ~ 2 mL. When the message on the top panel changes from “Not Ready” to “Waiting”, turn the lever on the injection loop down to the load position and hit the “Inject” button on the top panel. The message should change to running.

11. Success strands typically elute at ~ 20 minutes while failure strands elute at ~10 minutes. If in doubt, collect each fraction in separate labelled falcon tubes for further analysis.

12. At the end of your run, press the stop button. Flush out the column by repeating step 7 and rinse the injection loop. Turn off the pumps and the lamps and exit the software. Turn off the three HPLC units.

13. Freeze your collected fractions with liquid N_2 and lyophilize overnight.

A4.1.4 Removal of the DMT group

After HPLC purification, standard DNA contains a DMT group which must be removed. Note that DBCO DNA does not contain this DMT group and thus this step may be skipped for DBCO DNA. To cleave the DMT group:

1. Make a 20% (v/v) solution of Acetic Acid and add about 3-4 mL per 5 µM of DNA synthesized to the dry DNA.
2. Let sit for 1 hour at RT.
3. Then add approximately the same quantity of ethyl acetate to each tube. Vortex for 15 seconds and then centrifuge to separate out the ethyl acetate (top layer) from the DNA (bottom layer).
4. Remove the Ethyl Acetate and repeat step 3 twice. After removing the Ethyl Acetate, freeze and lyophilize the samples overnight.

A4.1.5. MALDI

MALDI which stands for Matrix Assisted Laser Desorption/Ionization is used to confirm the quality of the DNA samples synthesized. The matrix commonly used for DNA is 2,5 Dibenzohydrobenzoic acid (DHB). In MALDI, the matrix absorbs laser light (UV, ~ 300 nm) and heats up. This is sufficient to desorb and ionize the DNA sample mixed with the matrix. The ionized molecules are then driven across a potential and time of flight (TOF) mass spectrometry is used to determine the charge to mass (Q/m) ratio. The following are the steps to perform a MALDI measurement on the synthesized DNA sample:

1. Dissolve the DNA in 1mL of water. Clean the MALDI chip and place 1 µl of the matrix on any position on the chip. Then place 1 µl of the DNA on the matrix and mix the DNA into the matrix by pipetting up and down. Repeat this for each of the DNA strands synthesized. Let the chip dry.
2. Make a reservation for the MALDI ToF instrument. It is located in IMSERC and may be reserved through NUCORE.
3. Once at the instrument, open the software for the MALDI instrument. Hit the eject button – this will cause the coin chip holder to come out of the instrument. Place your coin chip in any position on the holder making sure that it is flush. Make a note of the position of your chip and place the holder back on the carrier. Hit the eject/load button again.
4. In the method selection tab, select LN_(4k_20kDa) _New_Oligo.par.
5. While the sample is loading, select the sample carrier tab in the bottom of the screen. Choose random walk "OFF". This will allow you to choose the location where the laser hits on the sample manually.
6. Select the correct position of your chip on the rectangle illustrated version of the plate. Similarly, select the sample position on the chip.
7. Make sure the laser power is between 25 and 30% by moving the cursor in the top panel.
8. Select "start". Move the cross-hair by clicking on the image in the top panel to manually select the position on the sample.
9. Use "save as" in the same panel to save the file. Repeat for any other samples on the chip.

Once done, hit eject to take out the Plate and the chip. Load the plate back after taking the chip out.

The Mass spectrum obtained may be automatically opened in the analysis software on the instrument called FlexAnalysis. The peaks observed in the spectrum may then be compared to the expected values of the Molecular weights for the synthesized DNA to confirm the quality of the DNA. The molecular weights and extinction coefficients of any DNA sequence may be determined using the IDT Oligoanalyzer tool on the IDT website.

A4.1.6. UV-Vis Spectroscopy

UV-Vis Spectroscopy is used to determine the quantity of DNA synthesized through a simple application of Lambert Beers law which relates the Absorbance (A) of a material to its molar extinction coefficient (ε), the path length (b) and the concentration (c):

$$A = \varepsilon\, b\, c$$

The protocol to use the Agilent UV-Vis Spectrometer is as follows:

1. Clean a 1 cm path length Quartz cuvette with water, bleach and dry using N_2.
2. Fill the cuvette with 1 mL Nanopure water.
3. Take a baseline scan: On the instrument, select the Scan Application from the CaryWIN UV folder. Choose setup > Baseline > Baseline correction > Ok. Insert the cuvette into the instrument and take a baseline scan by hitting baseline.
4. Then dissolve about 1-2 µL of the DNA stock solution in the 1 mL of water contained in the cuvette and insert into the instrument.

5. Hit Start to collect the UV-Vis spectrum and note down the absorbance value at 260 nm to determine the concentration of DNA using Lambert-Beers law as discussed above.

This process completes the characterization of the synthesized DNA. The DNA may now be used for particle functionalization.

A4.2 Protein Functionalization Protocol

The functionalization of Catalase with DNA is carried out via a two-step process: In the first step, the amine functional groups on the surface of the protein are converted into azides and in the second step the DBCO modified DNA is reacted with the Azide groups on the surface of the protein to result in DNA functionalization. A more detailed description of the chemistry of the reaction is provided in Section 2.1 of Chapter 2 (Methods). The protocol to carry out this functionalization reaction is as follows:

1. Transfer 300-400 µL of Catalase from Corynebacterium Glutamicum into a 0.5 mL 100 kDa spin filter (Amicon Ultra) housed in a centrifuge tube. Ultracentrifuge the sample at 15,000 rpm for 1.5 minutes to concentrate the protein in the filtrate. Discard the run-off and fill the filter basket with Sodium Bicarbonate buffer (100 mM $NaHCO_3$, 0.5 M NaCl, pH 9). Repeat this wash 4-5 times to concentrate the protein and effectively exchange into the Sodium Bicarbonate buffer.
2. Use 5µL of this concentrate in a volume of 1000 µL (200 X dilution) and measure its absorbance at 405 nm on a UV-Vis Spectrophotometer (Cary 5000). Using the molar extinction coefficient of Catalase at 405 nm (324,000 M^{-1} cm^{-1}), determine the concentration of the protein.

3. Disperse the proteins in the Sodium Bicarbonate buffer to a final concentration of 50 μM in a total volume of 100 μL. Add 6 mg of NHS-PEG$_4$-Azide linker (Cat. no. 26130) taking care to pipette slowly since the linker is viscous. Pipette/Vortex to mix taking care to ensure that the linker does not stick to the walls and cap of the Eppendorf tube. Place the Eppendorf tube in a Benchmark Multitherm shaker and allow to reaction for 2 hours at 25°C while shaking at 1500 rpm.

4. After 2 hours, remove the Eppendorf tube. Remove the excess linkers from the solution by washing the proteins 5 times using a 100 kDa spin filter as described in Step 1. Exchange the proteins into PBS buffer by 5-10 rounds of ultracentrifugation. Determine the concentration of proteins in the PBS buffer by UV-Vis (see step 2).

5. To functionalize the proteins with DBCO-modified DNA, disperse the proteins in PBS to a concentration of 1 μM and add the DNA to a final concentration of 300 μM in a total volume of 1000 μL. Place the tube in the shaker and allow the reaction to proceed for 3 days at 25°C while shaking at 1500 rpm.

6. After 3 days, the unreacted DNA can be removed by washing the proteins 10 times using a 100 kDa spin filter as described in step 1. The concentration of the protein and DBCO DNA on the protein can be determined through UV-Vis spectroscopy using the known molar extinction coefficients of the protein and DNA. The ratio of the concentration of DNA to that of the protein is used to determine the DNA loading density.

7. In order to duplex the ssDNA on the protein, a complementary strand may be added at a 100 times excess to the protein concentration. After approximately 2 hours of incubation, the unreacted duplexer strands may be removed by ultracentrifugation.

A5. The Effect of Solution Ionic Strength on the structural attributes of DNA functionalized onto a Protein

Several factors are known to influence the secondary structure of DNA functionalized onto nanoparticle surfaces. Interparticle hybridization effects, DNA type (dsDNA vs ssDNA), DNA loading density, core nanoparticle curvature and environmental conditions such as solution ionic strength have all been shown to affect the structural attributes of DNA within this spherical architecture. In order to deconvolute the effect of ionic strength from the other aforementioned factors and to better understand how DNA arranges itself on the nanoparticle surface under varying ionic conditions, we have investigated the structure of the DNA shell functionalized onto the surface of a protein. The use of a protein, as opposed to a traditional Au core allows us to measure the effective thickness of the DNA shell using small angle x-ray scattering. In addition, we use Circular Dichroism (CD) spectroscopy to corroborate our SAXS results. CD spectroscopy allows us to track changes in the secondary structure of DNA both on the particle surface and free in solution thus allowing us to probe the effect of functionalization on the salt dependent structural transitions of the DNA. We also use Dynamic Light Scattering to determine the effect of solution ionic strength on the effective Hydrodynamic radius of the Pro-SNA.

Results

In order to probe the structural attributes of the DNA corona functionalized onto the surface of a native protein as a function of ionic strength, SAXS profiles were collected for both native proteins and proteins modified with single and double stranded DNA suspended in NaCl salt solutions with concentrations ranging from 0.05 M NaCl to 2M NaCl. The corresponding SAXS intensities as a function of the scattering vector q are depicted in Figure A5.1(A) and (B) for the case of single and double stranded DNA respectively. In each of these plots, the position of the first minima is seen to shift to higher values of q with increasing salt concentration. Assuming a spherical shape for the construct, the radius of the conjugate R may be related to the q position of the first minima by:

$$R \sim \frac{4.5}{q_{min}} \tag{A5.1}$$

Thus, a shifting of the position of the first minima to higher q values implies a decrease in the radial extent of the conjugate with increasing salt concentration. Through an examination of native protein SAXS profiles it has been verified that the protein core does not undergo any structural changes with increasing NaCl salt concentration. As a result, the observed decrease in the overall size may be attributed to an effective shrinking of the DNA shell caused by increased electrostatic screening of the negative charges on the DNA at higher ionic strengths. In order to provide a model independent first order estimate of the size of the conjugate, Guinier analysis was applied to the DNA modified proteins at each of the salt concentration points probed. The results of this analysis are summarized in A5.1(C) and indicate that the average size of the construct decreases with increasing salt over the concentration range probed. Further, it is observed that at a given salt concentration the thickness of a double stranded DNA shell is greater than that for a single stranded shell. This result is intuitively expected since the hybridization of a duplexer strand to a single stranded DNA segment confers it with additional rigidity promoting a radially extended rod like structure.

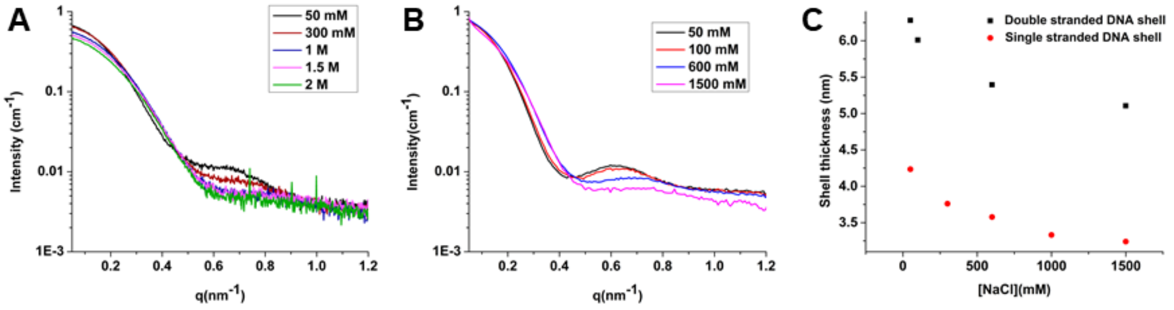

Figure A5.1: (A) SAXS Intensity profiles from single and double (B) stranded DNA functionalized proteins showing an increase in the q-position of the first minima indicative of a decrease in overall radial extent. (C) Variation in the thickness of a single and double stranded DNA shell on a protein as a function of solution NaCl

In addition to determining the size of the DNA shell via SAXS fits, we performed Circular Dichroism Spectroscopy on the bare protein, protein modified with ssDNA and dsDNA as well as free ssDNA and dsDNA in solution to investigate secondary structural changes within these constructs with increasing solution ionic strength. The CD spectra of a DNA functionalized protein is equivalent to the sum of the spectra measured from a native protein and free single or double stranded DNA (Fig. A5.2(A)). This is consistent with previous reports and suggests that DNA modification does not alter the secondary structure of the Catalase protein. Upon increasing the ionic strength, the CD spectra from proteins functionalized with ssDNA does not display any appreciable changes (Fig. A5.2(B)) indicating that the conformation of the ssDNA is unchanged.

However, for the case of proteins functionalized with dsDNA, the CD peak at 280 nm is seen to decrease upon increasing the salt concentration to 1M. This effect has previously been observed for free DNA wherein a conformation change from B-form to C-form DNA was seen when the monovalent salt concentration was raised to 4M. This decrease has been associated with an increase in the average rotation of the DNA double helix. These results represent a first important step towards obtaining a better understanding of the structural changes occurring within the DNA corona in high ionic environments. A complete characterization of this salt dependence will allow us to deconvolute the effects of ionic strength on DNA structure from other contributing factors.

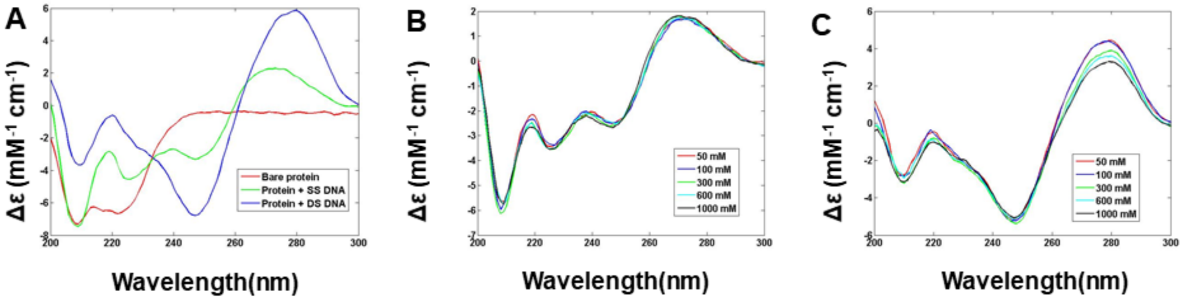

Figure A5.2: (A) CD Spectra from native protein (red) and protein functionalized with single-stranded (green) and double-stranded (blue) DNA (B) CD Spectra from single and (C) double stranded DNA functionalized protein as a function of NaCl concentration.

References

1. Solis, F. J.; Olvera de la Cruz, M., Collapse of flexible polyelectrolytes in multivalent salt solutions. *J. Chem. Phys.* **2000,** *112* (4), 2030-2035.

2. Bloomfield, V. A., DNA condensation by multivalent cations. *Biopolymers: Original Research on Biomolecules* **1997,** *44* (3), 269-282.

3. Scatchard, G., The attractions of proteins for small molecules and ions. *Annals of the New York Academy of Sciences* **1949,** *51* (4), 660-672.

4. Collins, K. D., Ions from the Hofmeister series and osmolytes: effects on proteins in solution and in the crystallization process. *Methods* **2004,** *34* (3), 300-311.

5. Mirkin, C. A.; Letsinger, R. L.; Mucic, R. C.; Storhoff, J. J., A DNA-based method for rationally assembling nanoparticles into macroscopic materials. *Nature* **1996,** *382*, 607.

6. Macfarlane, R. J.; Lee, B.; Jones, M. R.; Harris, N.; Schatz, G. C.; Mirkin, C. A., Nanoparticle Superlattice Engineering with DNA. *Science* **2011,** *334* (6053), 204.

7. Park, S. Y.; Lytton-Jean, A. K.; Lee, B.; Weigand, S.; Schatz, G. C.; Mirkin, C. A., DNA-programmable nanoparticle crystallization. *Nature* **2008,** *451* (7178), 553.

8. Auyeung, E.; Li, T. I. N. G.; Senesi, A. J.; Schmucker, A. L.; Pals, B. C.; de la Cruz, M. O.; Mirkin, C. A., DNA-mediated nanoparticle crystallization into Wulff polyhedra. *Nature* **2013,** *505*, 73.

9. Elghanian, R.; Storhoff, J. J.; Mucic, R. C.; Letsinger, R. L.; Mirkin, C. A., Selective colorimetric detection of polynucleotides based on the distance-dependent optical properties of gold nanoparticles. *Science* **1997,** *277* (5329), 1078-1081.

10. Rosi, N. L.; Mirkin, C. A., Nanostructures in Biodiagnostics. *Chemical Reviews* **2005,** *105* (4), 1547-1562.

11. Rosi, N. L.; Giljohann, D. A.; Thaxton, C. S.; Lytton-Jean, A. K. R.; Han, M. S.; Mirkin, C. A., Oligonucleotide-Modified Gold Nanoparticles for Intracellular Gene Regulation. *Science* **2006,** *312* (5776), 1027-1030.

12. Radovic-Moreno, A. F.; Chernyak, N.; Mader, C. C.; Nallagatla, S.; Kang, R. S.; Hao, L.; Walker, D. A.; Halo, T. L.; Merkel, T. J.; Rische, C. H., Immunomodulatory spherical nucleic acids. *Proceedings of the National Academy of Sciences* **2015,** *112* (13), 3892-3897.

13. Jin, R.; Wu, G.; Li, Z.; Mirkin, C. A.; Schatz, G. C., What Controls the Melting Properties of DNA-Linked Gold Nanoparticle Assemblies? *J. Am. Chem. Soc.* **2003,** *125* (6), 1643-1654.

14. Patel, P. C.; Giljohann, D. A.; Daniel, W. L.; Zheng, D.; Prigodich, A. E.; Mirkin, C. A., Scavenger receptors mediate cellular uptake of polyvalent oligonucleotide-functionalized gold nanoparticles. *Bioconjugate chemistry* **2010,** *21* (12), 2250-2256.

15. Chithrani, B. D.; Ghazani, A. A.; Chan, W. C., Determining the size and shape dependence of gold nanoparticle uptake into mammalian cells. *Nano letters* **2006,** *6* (4), 662-668.

16. Seferos, D. S.; Prigodich, A. E.; Giljohann, D. A.; Patel, P. C.; Mirkin, C. A., Polyvalent DNA nanoparticle conjugates stabilize nucleic acids. *Nano Lett.* **2009,** *9* (1), 308-311.

17. Giljohann, D. A.; Seferos, D. S.; Prigodich, A. E.; Patel, P. C.; Mirkin, C. A., Gene Regulation with Polyvalent siRNA-Nanoparticle Conjugates. *Journal of the American Chemical Society* **2009,** *131* (6), 2072-2073.

18. Lee, J.-S.; Lytton-Jean, A. K. R.; Hurst, S. J.; Mirkin, C. A., Silver Nanoparticle Oligonucleotide Conjugates Based on DNA with Triple Cyclic Disulfide Moieties. *Nano letters* **2007,** *7* (7), 2112-2115.

19. Cutler, J. I.; Zheng, D.; Xu, X.; Giljohann, D. A.; Mirkin, C. A., Polyvalent Oligonucleotide Iron Oxide Nanoparticle “Click” Conjugates. *Nano Letters* **2010,** *10* (4), 1477-1480.

20. Banga, R. J.; Chernyak, N.; Narayan, S. P.; Nguyen, S. T.; Mirkin, C. A., Liposomal Spherical Nucleic Acids. *Journal of the American Chemical Society* **2014,** *136* (28), 9866-9869.

21. Brodin, J. D.; Auyeung, E.; Mirkin, C. A., DNA-mediated engineering of multicomponent enzyme crystals. *Proc. Natl. Acad. Sci. U.S.A.* **2015,** *112* (15), 4564–4569.

22. Walenta, E., Small angle x-ray scattering. Von O. GLATTER und O. KRATKY. London: Academic Press Inc. Ltd. 1982. ISBN 0-12-286280-5. X, 515 Seiten, geb.£ 43, 60; US $81.00. *Acta Polymerica* **1985,** *36* (5), 296-296.

23. Li, T.; Senesi, A. J.; Lee, B., Small Angle X-ray Scattering for Nanoparticle Research. *Chemical Reviews* **2016,** *116* (18), 11128-11180.

24. Boal, A. K.; Ilhan, F.; DeRouchey, J. E.; Thurn-Albrecht, T.; Russell, T. P.; Rotello, V. M., Self-assembly of nanoparticles into structured spherical and network aggregates. *Nature* **2000,** *404* (6779), 746.

25. Polte, J.; Erler, R.; Thunemann, A. F.; Sokolov, S.; Ahner, T. T.; Rademann, K.; Emmerling, F.; Kraehnert, R., Nucleation and growth of gold nanoparticles studied via in situ small angle X-ray scattering at millisecond time resolution. *ACS nano* **2010,** *4* (2), 1076-1082.

26. Kammler, H. K.; Beaucage, G.; Mueller, R.; Pratsinis, S. E., Structure of flame-made silica nanoparticles by ultra-small-angle X-ray scattering. *Langmuir* **2004,** *20* (5), 1915-1921.

27. Bernadó, P.; Mylonas, E.; Petoukhov, M. V.; Blackledge, M.; Svergun, D. I., Structural characterization of flexible proteins using small-angle X-ray scattering. *Journal of the American Chemical Society* **2007,** *129* (17), 5656-5664.

28. Mertens, H. D.; Svergun, D. I., Structural characterization of proteins and complexes using small-angle X-ray solution scattering. *Journal of structural biology* **2010,** *172* (1), 128-141.

29. Rambo, R. P.; Tainer, J. A., Bridging the solution divide: comprehensive structural analyses of dynamic RNA, DNA, and protein assemblies by small-angle X-ray scattering. *Current opinion in structural biology* **2010,** *20* (1), 128-137.

30. Lipfert, J.; Doniach, S., Small-Angle X-Ray Scattering from RNA, Proteins, and Protein Complexes. *Annual Review of Biophysics and Biomolecular Structure* **2007,** *36* (1), 307-327.

31. Dingenonts, N.; Patel, M.; Rosenfeldt, S.; Pontoni, D.; Narayanan, T.; Ballauff, M., Counterion distribution around a spherical polyelectrolyte brush probed by anomalous small-angle X-ray scattering. *Macromolecules* **2004,** *37* (21), 8152-8159.

32. Kewalramani, S.; Zwanikken, J. W.; Macfarlane, R. J.; Leung, C.-Y.; Olvera de la Cruz, M.; Mirkin, C. A.; Bedzyk, M. J., Counterion Distribution Surrounding Spherical Nucleic Acid–Au Nanoparticle Conjugates Probed by Small-Angle X-ray Scattering. *ACS Nano* **2013,** *7* (12), 11301-11309.

33. Mann, S., Life as a Nanoscale Phenomenon. *Angewandte Chemie International Edition* **2008,** *47* (29), 5306-5320.

34. Pawson, T.; Scott, J. D., Signaling through scaffold, anchoring, and adaptor proteins. *Science* **1997,** *278* (5346), 2075-2080.

35. Liang, X.; Potter, J.; Kumar, S.; Zou, Y.; Quintanilla, R.; Sridharan, M.; Carte, J.; Chen, W.; Roark, N.; Ranganathan, S., Rapid and highly efficient mammalian cell engineering via Cas9 protein transfection. *Journal of biotechnology* **2015,** *208*, 44-53.

36. Brodin, J. D.; Sprangers, A. J.; McMillan, J. R.; Mirkin, C. A., DNA-Mediated Cellular Delivery of Functional Enzymes. *J. Am. Chem. Soc.* **2015,** *137* (47), 14838-14841.

37. McMillan, J. R.; Brodin, J. D.; Millan, J. A.; Lee, B.; Olvera de la Cruz, M.; Mirkin, C. A., Modulating Nanoparticle Superlattice Structure Using Proteins with Tunable Bond Distributions. *Journal of the American Chemical Society* **2017,** *139* (5), 1754-1757.

38. Fu, A.; Tang, R.; Hardie, J.; Farkas, M. E.; Rotello, V. M., Promises and Pitfalls of Intracellular Delivery of Proteins. *Bioconjugate Chemistry* **2014,** *25* (9), 1602-1608.

39. Hurst, S. J.; Lytton-Jean, A. K. R.; Mirkin, C. A., Maximizing DNA Loading on a Range of Gold Nanoparticle Sizes. *Analytical Chemistry* **2006,** *78* (24), 8313-8318.

40. Mitchell, G. P.; Mirkin, C. A.; Letsinger, R. L., Programmed Assembly of DNA Functionalized Quantum Dots. *Journal of the American Chemical Society* **1999,** *121* (35), 8122-8123.

41. Watson, J. D.; Crick, F. H., Molecular structure of nucleic acids. *Nature* **1953,** *171* (4356), 737-738.

42. Als-Nielsen, J.; McMorrow, D., *Elements of modern X-ray physics*. John Wiley & Sons: 2011.

43. Ballauff, M.; Jusufi, A., Anomalous small-angle X-ray scattering: analyzing correlations and fluctuations in polyelectrolytes. *Colloid and Polymer Science* **2006,** *284* (11), 1303-1311.

44. Bowers, E. M.; Ragland, L. O.; Byers, L. D., Salt effects on β-glucosidase: pH-profile narrowing. *Biochimica et Biophysica Acta (BBA)-Proteins and Proteomics* **2007,** *1774* (12), 1500-1507.

45. Sharp, K.; Fine, R.; Schulten, K.; Honig, B., Brownian dynamics simulation of diffusion to irregular bodies. *Journal of Physical Chemistry* **1987,** *91* (13), 3624-3631.

46. Gelbart, W. M.; Bruinsma, R. F.; Pincus, P. A.; Parsegian, V. A., DNA-Inspired Electrostatics. *Phys. Today* **2000,** *53* (9), 38.

47. McFail-Isom, L.; Sines, C. C.; Williams, L. D., DNA structure: cations in charge? *Curr. Opin. Struct. Biol.* **1999,** *9* (3), 298-304.

48. Duong-Ly, K. C.; Gabelli, S. B., Chapter Seven - Salting out of Proteins Using Ammonium Sulfate Precipitation. In *Methods Enzymol.*, 2014; Vol. 541, pp 85-94.

49. Dill, K. A., Dominant forces in protein folding. *Biochemistry* **1990,** *29* (31), 7133-7155.

50. Lindman, S.; Xue, W.-F.; Szczepankiewicz, O.; Bauer, M. C.; Nilsson, H.; Linse, S., Salting the charged surface: pH and salt dependence of protein G B1 stability. *Biophys. J.* **2006,** *90* (8), 2911-21.

51. Brodin, J. D.; Auyeung, E.; Mirkin, C. A., DNA-mediated engineering of multicomponent enzyme crystals. *Proc. Natl. Acad. Sci. U.S.A.* **2015,** *112* (15), 4564-4569.

52. Li, Y.; Girard, M.; Shen, M.; Millan, J. A.; Olvera de la Cruz, M., Strong attractions and repulsions mediated by monovalent salts. *Proceedings of the National Academy of Sciences* **2017,** *114* (45), 11838-11843.

53. Wang, M. X.; Brodin, J. D.; Millan, J. A.; Seo, S. E.; Girard, M.; Olvera de la Cruz, M.; Lee, B.; Mirkin, C. A., Altering DNA-Programmable Colloidal Crystallization Paths by Modulating Particle Repulsion. *Nano Letters* **2017,** *17* (8), 5126-5132.

54. Storhoff, J. J.; Elghanian, R.; Mucic, R. C.; Mirkin, C. A.; Letsinger, R. L., One-Pot Colorimetric Differentiation of Polynucleotides with Single Base Imperfections Using Gold Nanoparticle Probes. *Journal of the American Chemical Society* **1998,** *120* (9), 1959-1964.

55. Taton, T. A.; Mirkin, C. A.; Letsinger, R. L., Scanometric DNA Array Detection with Nanoparticle Probes. *Science* **2000,** *289* (5485), 1757.

56. Jensen, S. A.; Day, E. S.; Ko, C. H.; Hurley, L. A.; Luciano, J. P.; Kouri, F. M.; Merkel, T. J.; Luthi, A. J.; Patel, P. C.; Cutler, J. I.; Daniel, W. L.; Scott, A. W.; Rotz, M. W.; Meade, T. J.; Giljohann, D. A.; Mirkin, C. A.; Stegh, A. H., Spherical Nucleic Acid Nanoparticle Conjugates as an RNAi-Based Therapy for Glioblastoma. *Science translational medicine* **2013,** *5* (209), 209ra152-209ra152.

57. Park, S. Y.; Lytton-Jean, A. K. R.; Lee, B.; Weigand, S.; Schatz, G. C.; Mirkin, C. A., DNA-programmable nanoparticle crystallization. *Nature* **2008,** *451* (7178), 553-556.

58. Patel, M.; Rosenfeldt, S.; Ballauff, M.; Dingenouts, N.; Pontoni, D.; Narayanan, T., Analysis of the correlation of counterions to rod-like macroions by anomalous small-angle X-ray scattering. *Phys. Chem. Chem. Phys.* **2004,** *6* (11), 2962.

59. Das, R.; Mills, T.; Kwok, L.; Maskel, G.; Millett, I.; Doniach, S.; Finkelstein, K.; Herschlag, D.; Pollack, L., Counterion Distribution around DNA Probed by Solution X-Ray Scattering. *Phys. Rev. Lett.* **2003,** *90* (18), 188103-188103.

60. Pabit, S. a.; Meisburger, S. P.; Li, L.; Blose, J. M.; Jones, C. D.; Pollack, L., Counting ions around DNA with anomalous small-angle X-ray scattering. *J. Am. Chem. Soc.* **2010,** *132* (46), 16334-6.

61. Andresen, K.; Das, R.; Park, H. Y.; Smith, H.; Kwok, L. W.; Lamb, J. S.; Kirkland, E. J.; Herschlag, D.; Finkelstein, K. D.; Pollack, L., Spatial distribution of competing ions around DNA in solution. *Phys Rev Lett* **2004,** *93* (24), 248103.

62. Evans, G.; Pettifer, R. F., CHOOCH: a program for deriving anomalous-scattering factors from X-ray fluorescence spectra. *J. Appl. Crystallogr.* **2001,** *34* (1), 82-86.

63. Samejima, T.; Yang, J. T., Reconstitution of acid-denatured catalase. *J. Biol. Chem.* **1963,** *238* (10), 3256-3261.

64. Kozlowski, L. P., IPC–Isoelectric Point Calculator. *Biology direct* **2016,** *11* (1), 55.

65. Fan, L.; Degen, M.; Bendle, S.; Grupido, N.; Ilavsky, J. In *The absolute calibration of a small-angle scattering instrument with a laboratory X-ray source*, J. Phys. Conf. Ser., IOP Publishing: 2010; p 012005.

66. Zwanikken, J. W.; Guo, P.; Mirkin, C. A.; Olvera de la Cruz, M., Local Ionic Environment around Polyvalent Nucleic Acid-Functionalized Nanoparticles. *The Journal of Physical Chemistry C* **2011,** *115* (33), 16368-16373.

67. Svergun, D.; Barberato, C.; Koch, M. H. J., CRYSOL – a Program to Evaluate X-ray Solution Scattering of Biological Macromolecules from Atomic Coordinates. *J. Appl. Cryst* **1995,** *28*, 768-773.

68. Candelaresi, M.; Gumiero, A.; Adamczyk, K.; Robb, K.; Bellota-Anton, C.; Sangal, V.; Munnoch, J.; Greetham, G. M.; Towrie, M.; Hoskisson, P. A.; Parker, A. W.; Tucker, N. P.; Walsh,

M. A.; Hunt, N. T., A Structural and Dynamic Investigation of the Inhibition of Catalase by Nitric Oxide. *Org.Biomol.Chem.* **2013,** *11*, 7778-7778.

69. Raspaud, E.; Chaperon, I.; Leforestier, A.; Livolant, F., Spermine-induced aggregation of DNA, nucleosome, and chromatin. *Biophysical journal* **1999,** *77* (3), 1547-1555.

70. Arber, W., DNA modification and restriction. *Progress in nucleic acid research and molecular biology* **1974,** *14* (0), 1-37.

71. Lacks, S. A., Deoxyribonuclease I in mammalian tissues. Specificity of inhibition by actin. *Journal of Biological Chemistry* **1981,** *256* (6), 2644-2648.

72. Samejima, K.; Earnshaw, W. C., Trashing the genome: the role of nucleases during apoptosis. *Nature reviews Molecular cell biology* **2005,** *6* (9), 677.

73. Shiokawa, D.; Tanuma, S.-i., Characterization of human DNase I family endonucleases and activation of DNase γ during apoptosis. *Biochemistry* **2001,** *40* (1), 143-152.

74. Zagorovsky, K.; Chou, L. Y.; Chan, W. C., Controlling DNA–nanoparticle serum interactions. *Proceedings of the National Academy of Sciences* **2016,** *113* (48), 13600-13605.

75. Cutler, J. I.; Zhang, K.; Zheng, D.; Auyeung, E.; Prigodich, A. E.; Mirkin, C. A., Polyvalent nucleic acid nanostructures. *Journal of the American Chemical Society* **2011,** *133* (24), 9254-9257.

76. Song, L.; Guo, Y.; Roebuck, D.; Chen, C.; Yang, M.; Yang, Z.; Sreedharan, S.; Glover, C.; Thomas, J. A.; Liu, D., Terminal pegylated DNA–Gold nanoparticle conjugates offering high resistance to nuclease degradation and efficient intracellular delivery of DNA binding agents. *ACS applied materials & interfaces* **2015,** *7* (33), 18707-18716.

77. Yuan, Y.; Tan, J.; Wang, Y.; Qian, C.; Zhang, M., Chitosan nanoparticles as non-viral gene delivery vehicles based on atomic force microscopy study. *Acta Biochim Biophys Sin* **2009,** *41* (6), 515-526.

78. Han, G.; Martin, C. T.; Rotello, V. M., Stability of gold nanoparticle-bound DNA toward biological, physical, and chemical agents. *Chemical biology & drug design* **2006,** *67* (1), 78-82.

79. Suck, D.; Oefner, C., Structure of DNase I at 2.0 Å resolution suggests a mechanism for binding to and cutting DNA. *Nature* **1986,** *321* (6070), 620.

80. MATSUDA, M.; OGOSHI, H., Specificity of DNase I. *The Journal of Biochemistry* **1966,** *59* (3), 230-235.

81. Guéroult, M.; Picot, D.; Abi-Ghanem, J.; Hartmann, B.; Baaden, M., How Cations Can Assist DNase I in DNA Binding and Hydrolysis. *PLoS Computational Biology* **2010,** *6* (11), e1001000.

82. Price, P. A., The essential role of Ca2+ in the activity of bovine pancreatic deoxyribonuclease. *Journal of Biological Chemistry* **1975,** *250* (6), 1981-1986.

83. Melgar, E.; Goldthwait, D. A., Deoxyribonucleic acid nucleases II. The effects of metals on the mechanism of action of deoxyribonuclease I. *Journal of Biological Chemistry* **1968,** *243* (17), 4409-4416.

84. Campbell, V. W.; Jackson, D., The effect of divalent cations on the mode of action of DNase I. The initial reaction products produced from covalently closed circular DNA. *Journal of Biological Chemistry* **1980,** *255* (8), 3726-3735.

85. Shack, J., The Influence of Sodium and Magnesium Ions on the Action of Deoxyribonuclease II. *Journal of Biological Chemistry* **1959,** *234* (11), 3.

86. Barnaby, S. N.; Lee, A.; Mirkin, C. A., Probing the inherent stability of siRNA immobilized on nanoparticle constructs. *Proceedings of the National Academy of Sciences* **2014,** *111* (27), 9739-9744.

87. Craievich, A. F., Synchrotron SAXS Studies of Nanostructured Materials and Colloidal Solutions: A Review. *Materials Research* **2002,** *5*, 1-11.

88. Skou, S.; Gillilan, R. E.; Ando, N., Synchrotron-based small-angle X-ray scattering (SAXS) of proteins in solution. *Nature protocols* **2014,** *9* (7), 1727-1739.

89. Graewert, M. A.; Svergun, D. I., Impact and progress in small and wide angle X-ray scattering (SAXS and WAXS). *Current Opinion in Structural Biology* **2013,** *23* (5), 748-754.

90. Kurinji Krishnamoorthy, K. H., Sumit Kewalramani, Jeffrey D. Brodin, Liane Moreau, Monica Olvera de la Cruz, Chad Mirkin, Michael Bedzyk, Defining the structure of a protein-spherical nucleic acid conjugate and its counterionic cloud. *ACS Central Science (Under revision)* **2018**.

91. Lang, J.; Maréchal, A.; Couture, M.; Santolini, J., Reaction intermediates and molecular mechanism of Peroxynitrite activation by NO synthases. *Biophysical journal* **2016,** *111* (10), 2099-2109.

92. Vinokurov, I. A.; Kankare, J., Beer's law and the isosbestic points in the absorption spectra of conductive polymers. *The Journal of Physical Chemistry B* **1998,** *102* (7), 1136-1140.

93. Dai, X.; Mashiguchi, K.; Chen, Q.; Kasahara, H.; Kamiya, Y.; Ojha, S.; DuBois, J.; Ballou, D.; Zhao, Y., The biochemical mechanism of auxin biosynthesis by an Arabidopsis YUCCA flavin-containing monooxygenase. *Journal of Biological Chemistry* **2013,** *288* (3), 1448-1457.

94. Matsudaira, P.; Bordas, J.; Koch, M., Synchrotron x-ray diffraction studies of actin structure during polymerization. *Proceedings of the National Academy of Sciences* **1987,** *84* (10), 3151-3155.

95. Perakis, F.; Amann-Winkel, K.; Lehmkühler, F.; Sprung, M.; Mariedahl, D.; Sellberg, J. A.; Pathak, H.; Späh, A.; Cavalca, F.; Schlesinger, D., Diffusive dynamics during the high-to-low density transition in amorphous ice. *Proceedings of the National Academy of Sciences* **2017,** *114* (31), 8193-8198.

96. Helm, C.; Tippmann-Krayer, P.; Möhwald, H.; Als-Nielsen, J.; Kjaer, K., Phases of phosphatidyl ethanolamine monolayers studied by synchrotron x-ray scattering. *Biophysical journal* **1991,** *60* (6), 1457-1476.

97. Rosi, N. L.; Giljohann, D. A.; Thaxton, C. S.; Lytton-Jean, A. K.; Han, M. S.; Mirkin, C. A., Oligonucleotide-modified gold nanoparticles for intracellular gene regulation. *Science* **2006,** *312* (5776), 1027-1030.

98. Zheng, D.; Seferos, D. S.; Giljohann, D. A.; Patel, P. C.; Mirkin, C. A., Aptamer nano-flares for molecular detection in living cells. *Nano letters* **2009,** *9* (9), 3258-3261.

99. Leskovac, V., *Comprehensive enzyme kinetics*. Springer Science & Business Media: 2003.

100. Terry, J., The major electrolytes: sodium, potassium, and chloride. *Journal of intravenous nursing: the official publication of the Intravenous Nurses Society* **1994,** *17* (5), 240-247.

101. Parsegian, V., Long-range physical forces in the biological milieu. *Annual review of biophysics and bioengineering* **1973,** *2* (1), 221-255.

102. Collins, K. D.; Neilson, G. W.; Enderby, J. E., Ions in water: characterizing the forces that control chemical processes and biological structure. *Biophysical chemistry* **2007,** *128* (2-3), 95-104.

103. Honig, B.; Nicholls, A., Classical electrostatics in biology and chemistry. *Science* **1995,** *268* (5214), 1144-1149.

104. Abdizadeh, H.; Atilgan, A. R.; Atilgan, C., Mechanisms by Which Salt Concentration Moderates the Dynamics of Human Serum Transferrin. *The Journal of Physical Chemistry B* **2017,** *121* (18), 4778-4789.

105. Hille, B., *Ion channels of excitable membranes*. Sinauer Sunderland, MA: 2001; Vol. 507.

106. DuPont, F., Salt-induced changes in ion transport: regulation of primary pumps and secondary transporters. In *Transport and receptor proteins of plant membranes*, Springer: 1992; pp 91-100.

107. Chonn, A.; Semple, S.; Cullis, P., Protein-membrane interactions in the complex biological milieu. In *Biological membranes: structure, biogenesis and dynamics*, Springer: 1994; pp 101-106.

108. Mirshafiee, V.; Kim, R.; Mahmoudi, M.; Kraft, M. L., The importance of selecting a proper biological milieu for protein corona analysis in vitro: Human plasma versus human serum. *The international journal of biochemistry & cell biology* **2016,** *75*, 188-195.

109. Price, P. A., Characterization of Ca++ and Mg++ binding to bovine pancreatic deoxyribonuclease A. *Journal of Biological Chemistry* **1972,** *247* (9), 2895-2899.

110. Lodish, H.; Berk, A.; Zipursky, S. L.; Matsudaira, P.; Baltimore, D.; Darnell, J., Intracellular ion environment and membrane electric potential. **2000**.

111. González-Mozuelos, P.; de la Cruz, M. O., Ion condensation in salt-free dilute polyelectrolyte solutions. *The Journal of Chemical Physics* **1995,** *103* (8), 3145-3157.

112. Bacquet, R. J.; Rossky, P. J., Ionic distributions and competitive association in DNA/mixed salt solutions. *The Journal of Physical Chemistry* **1988,** *92* (12), 3604-3612.

113. Andresen, K.; Qiu, X.; Pabit, S. A.; Lamb, J. S.; Park, H. Y.; Kwok, L. W.; Pollack, L., Mono- and Trivalent Ions around DNA: A Small-Angle Scattering Study of Competition and Interactions. *Biophysical Journal* **2008,** *95* (1), 287-295.

114. Kirmizialtin, S.; Pabit, S. A.; Meisburger, S. P.; Pollack, L.; Elber, R., RNA and its ionic cloud: solution scattering experiments and atomically detailed simulations. *Biophysical journal* **2012,** *102* (4), 819-828.

115. Andresen, K.; Das, R.; Park, H. Y.; Smith, H.; Kwok, L. W.; Lamb, J. S.; Kirkland, E.; Herschlag, D.; Finkelstein, K.; Pollack, L., Spatial distribution of competing ions around DNA in solution. *Physical review letters* **2004,** *93* (24), 248103.

116. Wu, C.; Chen, S.; Shih, L.; Lin, J., Direct measurement of counterion distribution around cylindrical micelles by small-angle X-ray scattering. *Physical review letters* **1988,** *61* (5), 645.

117. Rouzina, I.; Bloomfield, V. A., Competitive electrostatic binding of charged ligands to polyelectrolytes: practical approach using the non-linear Poisson-Boltzmann equation. *Biophysical chemistry* **1997,** *64* (1-3), 139-155.

118. Henke, B., *X-ray interactions : photoabsorption, scattering, transmission, and reflection at E = 50-30,000 eV, Z = 1-92*. Academic Press: San Diego, 1993.

119. Guiner, A.; Fournet, G.; Walker, C., Small angle scattering of X-rays. *J. Wiley & Sons, New York* **1955**.

120. Candelaresi, M.; Gumiero, A.; Adamczyk, K.; Robb, K.; Bellota-Anton, C.; Sangal, V.; Munnoch, J.; Greetham, G. M.; Towrie, M.; Hoskisson, P. A.; Parker, A. W.; Tucker, N. P.; Walsh, M. A.; Hunt, N. T., A Structural and Dynamic Investigation of the Inhibition of Catalase by Nitric Oxide. *Org. Biomol. Chem.* **2013,** *11*, 7778-7778.

121. James, R. W., *The Optical Principles Of The Diffraction Of X Rays Vol II*. G. Bell And Sons Limited, 1969.

122. Egli, M.; Saenger, W., *Principles of Nucleic Acid Structure*. Springer: New York, 1984.